Indium Phosphide Quantum Dots in GaP and in $In_{0.48}Ga_{0.52}P$

Growth and Properties

DISSERTATION

zur Erlangung des akademischen Grades
doctor rerum naturalium
(dr. rer. nat.)
im Fach Physik

eingereicht an der
Mathematisch-Naturwissenschaftlichen Fakultät I
Humboldt-Universität zu Berlin

von
Dipl.-Phys. Fariba Hatami
geboren am 03.06.1966 in Teheran

Präsident der Humboldt-Universität zu Berlin:
Prof. Dr. Jürgen Mlynek

Dekan der Mathematisch-Naturwissenschaftlichen Fakultät I:
Prof. Dr. Michael Linscheid

Gutachter:

1. Prof. Dr. W. Ted Masselink
2. Prof. Dr. Klaus Ploog
3. Prof. Dr. Anupam Madhukar

eingereicht am: 07. Mai 2002
Tag der mündlichen Prüfung: 23. Oktober 2002

Abstract

The growth and structural properties of self-assembled InP quantum dots are presented and discussed, together with their optical properties and associated carrier dynamics. The QDs are grown using gas-source molecular-beam epitaxy in and on the two materials $In_{0.48}Ga_{0.52}P$ (lattice matched to GaAs) and GaP.

Under the proper growth conditions, formation of InP dots via the Stranski-Krastanow mechanism is observed. The critical InP coverage for 2D-3D transition is found to be 3 ML for the InP/$In_{0.48}Ga_{0.52}P$ system and 1.8 ML for the InP/GaP system. The structural characterization indicates that the InP/GaP QDs are larger and, consequently, less dense compared to the InP/$In_{0.48}Ga_{0.52}P$ QDs; hence, InP dots on GaP tend to be strain-relaxed. The InP/$In_{0.48}Ga_{0.52}P$ QDs tend to form ordered arrays when InP coverage is increased.

Intense photoluminescence from InP quantum dots in both material systems is observed. The PL from InP/GaP QDs peaks between 1.9 and 2 eV and is by about 200 meV higher in energy than the PL line from InP/$In_{0.48}Ga_{0.52}P$ QDs. The optical emission from dots is attributed to direct transitions between the electrons and heavy-holes confined in the InP dots, whereas the photoluminescence from a two-dimensional InP layer embedded in GaP is explained as resulting from the spatially indirect recombination of electrons from the GaP X valleys with holes in InP and their phonon replicas. The type-II band alignment of InP/GaP two-dimensional structures is further confirmed by the carrier lifetime above 19 ns, which is much higher than in type-I systems. The observed carrier lifetimes of 100–500 ps for InP/$In_{0.48}Ga_{0.52}P$ QDs and 2 ns for InP/GaP QDs support our band alignment modeling. Pressure-dependent photoluminescence measurements provide further evidence for a type-I band alignment for InP/GaP QDs at normal pressure, but indicate that they become type II under hydrostatic pressures of about 1.2 GPa and are consistent with an energy difference between the lowest InP and GaP states of about 31 meV. Exploiting the visible direct-bandgap transition in the GaP system could lead to an increased efficiency of light emission in GaP-based light emitters.

Zusammenfassung

Im Rahmen dieser Arbeit wurden selbstorganisierte, verspannte InP-Quantenpunkte mittels Gasquellen-Molekularstrahlepitaxie hergestellt und deren strukturelle und optische Eigenschaften untersucht. Die Quantenpunkte wurden sowohl in $In_{0.48}Ga_{0.52}P$-Matrix gitterangepasst auf GaAs-Substrat als auch in GaP-Matrix auf GaP-Substrat realisiert.

Die starke Gitterfehlanpassung von 3,8% im InP/$In_{0.48}Ga_{0.52}P$- bzw. 7,7% im InP/GaP-Materialsystem ermöglicht Inselbildung mittels des Stranski-Krastanow-Wachstumsmodus: Ab einer kritischen InP-Schichtdicke findet kein zweidimensionales, sondern ein dreidimensionales Wachstum statt. Die kritische Schichtdicke wurde mit etwa 3 Monolagen für das InP/$In_{0.48}Ga_{0.52}P$- und mit etwa 1,8 Monolagen für das InP/GaP-System bestimmt. Die strukturellen Untersuchungen zeigen, dass InP Quantenpunkte in GaP im Vergleich zu solchen in $In_{0.48}Ga_{0.52}P$ größer sind und stärker zum Abbau von Verspannung tendieren. Die in $In_{0.48}Ga_{0.52}P$-Matrix eingebettete InP-Quantenpunkte zeigen sehr ausgeprägte optische Emissionen, die, in Abhängigkeit von den Wachstumsparametern, im Bereich von 1,6 bis 1,75 eV liegen. Die Emissionslinie wird der strahlenden Rekombination von in den Quantenpunkten lokalisierten Elektronen und Löchern zugeordnet. Dies wird auch durch das Bänderschema bestätigt, das mit Hilfe der *Model-Solid*-Theorie modelliert wurde. Darüber hinaus weist die Lebensdauer der Ladungsträger von einigen hundert Pikosekunden darauf hin, dass die InP/$In_{0.48}Ga_{0.52}P$ Quantenpunkte vom Typ I sind.

Zusätzlich zu den optischen Eigenschaften wurde die Anordnung von dicht gepackten InP-Quantenpunkten in und auf $In_{0.48}Ga_{0.52}P$ mittels zweidimensionaler Fourier-Transformation der Daten aus der Atomkraftmikroskopie, Transmissionelektronmikroskopie und diverser Röntgen-Streuexperimente untersucht sowie die planaren und vertikale Ordnungseffekte der Quantenpunkte studiert. Die Untersuchungen zeigen, dass die Ordnung der Quantenpunkte sowohl hinsichtlich ihrer Packungsdichte als auch ihrer Orientierung mit wachsender InP-Bedeckung zunimmt. Darüber hinaus wurde die Verspannungsverteilung in den InP/$In_{0.48}Ga_{0.52}P$-Quantenpunkten mit Hilfe von diffuser Röntgen-Streuung in Verbindung mit kinematischen Simulationen studiert und eine asymmetrische Form der Quantenpunkte festgestellt, die auch Ursache für die gemessene Polarisationsanisotropie der Photolumineszenz sein kann.

Die in GaP-Matrix eingebetteten InP-Quantenpunkte wurden im Rahmen

dieser Arbeit erstmals erfolgreich auf ihre aktiven optischen Eigenschaften hin untersucht. Sie zeigen eine optische Emission zwischen 1,9 und 2 eV im sichtbaren Bereich. Diese strahlende Rekombination wird ebenfalls dem direkten Übergang zwischen Elektronen- und Löcherzuständen zugeordnet, die in den InP Quantenpunkten lokalisiert sind. Auch Photolumineszenzmessungen unter mechanischem Druck weisen darauf hin, dass es sich in diesem System hauptsächlich um einen direkten räumlichen Übergang handelt. Dieses Ergebnis wird dadurch untermauert, dass die Lebensdauer der Ladungsträger im Bereich von etwa 2 ns liegt, was nicht untypisch für Typ-I-Systeme ist.

Die Ergebnisse für zweidimensionale, in GaP eingebettete InP-Schichten zeigen im Gegensatz zu den Quantenpunkten, dass die strahlende Rekombination in InP/GaP Quantentöpfen aufgrund eines indirekten Übergangs (sowohl in Orts- als auch in Impulsraum) zwischen Elektronen- und Löcherzuständen erfolgt. Die optischen Emissionslinien liegen für Quantentöpfe im Bereich von 2,15 bis 2,30 eV. Die nachgewiesene sehr lange Lebensdauer der Ladungsträger von etwa 20 ns weist weiter darauf hin, dass die Quantentöpfe ein Typ-II-System sind. Nach Modellierung des Bänderschemas für das verspannte InP/GaP-System und Berechnung der Energieniveaus von Löchern und Elektronen darin mit Hilfe der Effektive-Masse-Näherung in Abhängigkeit von der InP-Schichtdicke zeigt sich ferner, dass für InP-Quantentöpfe mit einer Breite kleiner als 3 nm die Quantisierungsenergie der Elektronen so groß ist, dass der X-Punkt in GaP energetisch tiefer liegt als der Γ-Punkt in InP. Dieser Potentialverlauf führt dazu, dass die Elektronen im X-Minimum des GaP lokalisieren, während die Löcher in der InP-Schicht bleiben. Optische Untersuchungen nach thermischer Behandlung der Quantenpunkte führen sowohl im InP/$In_{0.48}Ga_{0.52}P$- als auch im InP/GaP-System zur Verstärkung der Lumineszenz, die bis zu 15 mal internsiver als bei unbehandelten Proben sein kann.

Insgesamt zeigt diese Arbeit, dass InP-Quantenpunkte durch ihre optischen Eigenschaften sehr interessant für optoelektronische Anwendungen sind. Die Verwendung von durchsichtigem GaP (mit einer größeren Bandlücke und kleineren Gitterkonstante im Vergleich zu GaAs und $In_{0.48}Ga_{0.52}P$) als Matrix und Substrat hat nicht nur den Vorteil, dass die InP-Quantenpunkte hierbei im sichtbaren Bereich Licht emittieren, sondern man kann in der Praxis auch von einer hochentwickelten GaP-basierten LED-Technologie profitieren.

Hauptergebnis dieser Arbeit ist, dass die in indirektes GaP eingebetteten InP-Quantenpunkte aktive optische Eigenschaften zeigen. Sie können daher als

aktive Medien zur Realisierung neuartiger effizienter Laser und Leuchtdioden verwendet werden.

Parts of this work have been published in

- F. Hatami, U. Müller, H. Kissel, K. Braune, R.-P. Blum, S. Rogaschewski, H. Niehus, H. Kirmse, W. Neumann, M. Schmidbauer, R. Köhler, and W.T. Masselink,
  Planar ordering of InP quantum dots on (100) $In_{0.48}Ga_{0.52}P$,
  J. Cryst. Growth **216**, 26 (2000).

- F. Hatami, U. Müller, H. Kissel, K. Braune, R.-P. Blum, S. Rogaschewski, H. Niehus, H. Kirmse, W. Neumann, M. Schmidbauer, R. Köhler, and W.T. Masselink,
  Planar ordering of InP quantum dots on InGaP,
  Proc. 26th International Symposium on Compound Semiconductors, Berlin, Germany, 1999, edited by Institute of Physics Conference series No. 166, p. 235 (2000).

- F. Hatami, L. Schrottke, and W.T. Masselink,
  Optical spectroscopy of self-assembled InP quantum dots grown on GaP using gas-source molecular beam epitaxy,
  Proc. 12th International Conference of Microelectronics (ICM 2000), Teheran, Iran, IEEE, p. 129 (2000).

- M. Schmidbauer, F. Hatami, P. Schäfer, M. Hanke, Th. Wiebach, H. Niehus, W.T. Masselink, and R. Köhler,
  Shape, strain and spatial correlation of InP/InGaP QDs multilayers,
  Proc. Material Research Society Symposium **642**, J6.8 (2001).

- F. Hatami, L. Schrottke, and W.T. Masselink,
  Radiative recombination in InP quantum dots,
  Proc. Material Research Society Symposium **642**, J7.7 (2001).

- F. Hatami, L. Schrottke, and W.T. Masselink,
  Radiative recombination from InP quantum dots on (100) GaP,
  Appl. Phys. Lett. **78**, 2163 (2001).

- F. Hatami, G. Mussler, M. Schmidbauer, L. Schrottke, H.-Y. Hao, H.T. Grahn, and W.T. Masselink,
  Optical emission from ultrathin strained type-II InP/GaP quantum wells,
  Appl. Phys. Lett. **79**, 2886 (2001).

- W.T. Masselink, F. Hatami, G. Mussler, and L. Schrottke,
  InP quantum dots in (100) GaP: Growth and luminescence,
  Materials Science in Semiconductor Processing **4**, 497 (2002),
  Proc. International Conference on Materials for Advanced Technologies (ICMAT 2001), 1–6 July 2001, Singapore.

- M. Schmidbauer, M. Hanke, F. Hatami, P. Schäfer, H. Raidt, D. Grigoriev, T. Panzer, W.T. Masselink, and R. Köhler,
  Shape induced anisotropic elastic relaxation in InP/InGaP quantum dots,
  Physica E **13** (2-4), 1139 (2002),
  Proc. 10th International Conference on Modulated Semiconductor Structures (MSS10), 23–27 July 2001, Linz, Austria.

- M. Schmidbauer, F. Hatami, M. Hanke, P. Schäfer, K. Braune, W.T. Masselink, R. Köhler, and M. Ramsteiner,
  Shape mediated anisotropic strain in self-asselmbed InP/InGaP quantum dots,
  Phys. Rev. B **65**, 125320 (2002).

- A.R. Goñi, C. Kristukat, F. Hatami, S. Dressler, W.T. Masselink, and C. Thomsen,
  High-pressure photoluminescence study of the electronic structure of InP/GaP quantum dots,
  physica status solidi (b) **235**(2), 412 (2003), Proc. 10th International Conference on High Pressure Semiconductor Physics (HPSP-X, satelite conference of the ICPS-26), 5-8 August 2002, Guildford, UK.

- F. Hatami, W.T. Masselink, L. Schrottke, J. W. Tomm, V. Talalaev, C. Kristukat, A.R. Goñi,
  InP quantum dots embedded in GaP: optical properties and carrier dynamics,
  Phys. Rev. B **67**, 85306 (2003).

- A.R. Goñi, C. Kristukat, F. Hatami, S. Dressler, W.T. Masselink, and C. Thomsen,
  Electronic structure of self-assembled InP/GaP quantum dots from high-pressure photoluminescence,
  Phys. Rev. B **67**, 75306 (2003).

Contents

Chapter 1

Introduction

The impressive progress in epitaxial growth technology in recent years has allowed the reduction of spatial extent in one, two, and even all three dimensions to the nanometer scale directly through growth. The best-known and most widely applied example of epitaxially-controlled low-dimensional systems is the quasi-two-dimensional quantum well (QW) system, in which the spatial extent in one dimension is made so small that the physical properties of the material are significantly different from bulk. Quantum dots (QDs) are nanostructures whose spatial extent in all three dimensions are small enough that they exhibit in some respects quasi-zero-dimensional electronic properties. During the last decade, quantum dots have been a focus of interest for many research groups.

In the early 1980s, it became known that quantum dots are not only inherently important for the understanding of quasi-zero dimensional quantum systems, but also offer promising improvements in optical and electronic devices [1]. In the early 1990s, the self-organized growth mechanism driven by the lattice mismatch between strained epitaxial layers was used for the fabrication of quantum dots [2, 3]. Today, quantum dots are applied as an active material in optical and electronic devices. For example, using indium arsenide (InAs) quantum dots in a gallium arsenide (GaAs) matrix, 1.3 μm lasers on GaAs substrate could recently be fabricated [4, 5].

The most extensively investigated QD system is that of InAs quantum dots on and in GaAs. More exotic systems, such as indium phosphide (InP) quantum dots on and in the indirect gallium phosphide (GaP), are less known; the InP/GaP, however, is a very interesting system. First, analogous to the InAs/GaAs system, quantum dot formation in InP/GaP system due to the self-organized growth mechanism is expected under the proper growth conditions, driven by the lattice mismatch between strained InP and GaP. Second, due to the high indirect bandgap energy of GaP of 2.3 eV, an optical emission from InP quantum dots in the visible range is expected. Third, the use of GaP as substrate could take advantage of a well-developed light-emitting diode (LED) technology. Finally, using the transparent GaP rather than GaAs as substrate allows easier extraction of the emitted light for vertical structures such as vertical cavity lasers.

To study the structural, optical, and electronic properties of InP quantum dots, I have fabricated InP quantum dots in GaP as well as in $In_{0.48}Ga_{0.52}P$ matrix. A broad range of experimental techniques have been employed for the investigation and characterization of the resulting InP quantum dots to further understand the growth mechanisms and carrier dynamics in both systems.

This work is organized as follows: Chapter 2 serves to describe the fundamental properties of nanostructures. Chapter 3 gives an introduction in epitaxial growth. Chapter 4 surveys various techniques used in the course of this work to characterize structures. Chapter 5 discusses the growth of and results for the $InP/In_{0.48}Ga_{0.52}P$ system. In Chapter 6, likewise, the results on growth and on structural and optical characterization of the InP/GaP system are presented and discussed. An important aspect for QD-based optoelectronic application is the quantum dot ordering; therefore, Chapter 7 is devoted to the results from structural studies on planar and vertical ordering. This chapter also includes the theoretical modeling of quantum dot geometry. QD properties can also be modified and controlled using post-growth methods such as rapid thermal annealing; the results of this special treatment on InP QDs are discussed in Chapter 8.

Chapter 2

Physics of quantum heterostructures

2.1 Introduction

When the thickness of a solid is of the order of the de Broglie wavelength for the carrier of momentum p, the carrier is confined and its motion in the solid is limited. We will observe quantum effects and speak of quantum structures. The de Broglie wavelength λ is given by

$$\lambda = \frac{h}{p} = \frac{h}{\sqrt{3m_{eff}k_BT}} \tag{2.1}$$

where m_{eff} is the effective mass of carrier, and T denotes the temperature of carrier. Because m_{eff} of the carriers in a solid is normally much smaller than the free electron mass, size quantization effects can already be observed at a thickness in nanometer range.

Size quantization in quantum structures, also known as nanostructures, has pronounced effects on the physics of these structures. This chapter will focus on the fundamental physics of QWs and QDs, which is necessary for the understanding of electronic structures and optical properties later in this work. The chapter is organized as follows: Section 2.2 gives an introduction to heterostructure and its band alignment. Section 2.3 discusses band structure. Both band alignment and band structure deliver essential information on optical and electronic properties of heterostructures. Section 2.4 introduces the density of electronic states functions for low-dimensional systems. Section 2.5 serves to introduce strain as the most important cause for self-organized quantum dots to develop. Section 2.6 discusses the excitons that are decisive for optical properties.

2.2 Band alignment of heterostructures

When two different semiconductors are adjacent to each other, they form a heterojunction. Heterostructures comprise at least one heterojunction. Modern epitaxial growth methods allow the preparation of heterostructures with nearly abrupt interfaces in the range of Ångstroms. Although the heterostructures are made from common semiconductors, they allow to realize novel semiconductor devices [6].

One of the fundamental problems in modeling quantum heterostructures is the band alignment. The band alignment is given by the relative energy position of the band edges of heterostructures at the interface of heterojunctions (or at the surface). The existing charge carriers in a heterostructure will attempt to lower their energy. Thus, the band alignment determines the potential energy profile for the charge carriers, which is decisive for optical and electronic properties. Two basic systems of band alignment exist: type I and type II.

In type-I systems the bandgaps of the semiconductors A and B are aligned in

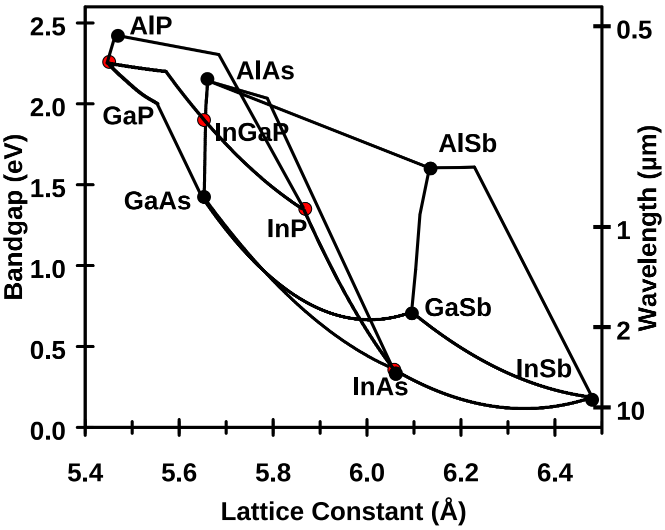

Figure 2.1: Energy gap and corresponding optical wavelength versus lattice constant at 300 K for most III-V semiconductors. The connection lines denote the behavior for corresponding alloys.

a way that the barriers for electrons (conduction band, CB) and holes (valence band, VB) are in the same semiconductor (see Fig. 2.2), leading to localization of electrons and holes in the same material.

In contrast to type-I systems, in type-II systems the band alignment of the semiconductors A and C gives rise to a barrier either for electrons or for holes in each of the aligned semiconductors, which leads to localization of electrons and holes in different materials, i.e., to a spatial separation of the carrier types. Consequently, the electron-hole overlap is smaller than in a type-I system, resulting in longer recombination times.

The theoretical work on band alignment of heterostructures may be divided into there groups: The first group consists of numerical calculations of the electronic structure of a certain interface for finding the Hamiltonian and thereafter solving the Schrödinger equation. In such a way the electronic structure of the interface, including the band alignment can be calculated. The second group comprises of analysis of electronic properties of the interface, which are experimentally obtained and provide information on the band alignment. The third group tries to analyze qualitatively the band alignment, which results in *model theories.* The model theories allow to simplify and to reduce the band alignment modeling to a few basic parameters and, hence, they involve a minimum of calculation. The accuracy of this method, however, is limited by the approximation being used to simplify the problem. (For an overview refer to [6].)

To solve the band alignment problem here, I have applied Van de Walle's

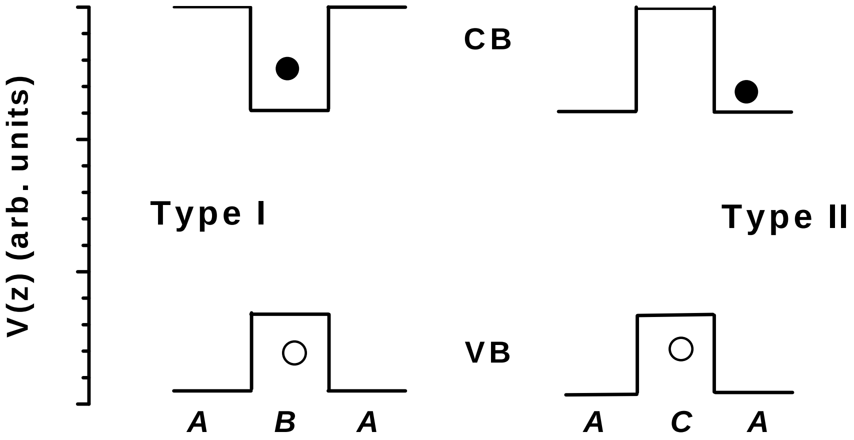

Figure 2.2: The one-dimensional potential energy profile V(z) for electrons and holes in a type-I and a type-II system. Open and solid circles indicate holes and electrons, respectively.

model-solid theory [7]. This approach fixes an *absolute* energy level for each semiconductor, and certain *deformation potentials* that describe the effects of strain on the electronic structures. Van de Walle's model will be discussed in more detail in Section 2.5.

2.3 Band structure of low-dimensional systems

Band structure delivers the most important information about the electronic states for a system. In free carrier approximation the band structure is described by the dispersion relation as function of the carrier momentum $\mathbf{k}$

$$E(\mathbf{k}) = \frac{\hbar^2}{2m_{eff}} \left(k_x^2 + k_y^2 + k_z^2\right), \tag{2.2}$$

which is clearly just the kinetic energy of a wave traveling in three-dimensional space. Furthermore, the effective mass m_{eff} for free carriers is given by

$$(m_{eff})_{ij} = \hbar^2 \left(\frac{\partial^2 E}{\partial \mathbf{k}_i \partial \mathbf{k}_j}\right)^{-1}. \tag{2.3}$$

In the case of a bulk crystal with ionic bonding between atoms, the upper valence bands arise from highest occupied atomic p-levels of the anions with a mixture of d-levels, or from the binding state of the sp^3 hybrid orbits for covalent bonding.

The lowest conduction band is formed by the lowest empty s-levels of the cations or by the antibonding sp^3 hybrid states. In zinc-blende structures, the valence band energy has its maximum at the Γ point ($\mathbf{k}$=0). It is six-fold degenerated and split, due to spin-orbit coupling, into a two-fold degenerated (Γ_7) and a four-fold degenerated band (Γ_8).

The Γ_8 valence band splits at $k \neq 0$ into two bands. They have different curvature and are known as heavy-hole and light-hole bands. All bands have cubic symmetry. Consequently, the dispersion and, thus, the hole masses depend on the direction of $\mathbf{k}$. The conduction band energy has a minimum at the Γ point, but also at points outside the center of the Brillouin zone (X and L points).

In the case of a *direct* semiconductor, Γ point is a global minimum of conduction band energy and transition between valence band and conduction band is possible via photons, having momentum about zero. Otherwise, the semiconductor is called *indirect* and a momentum-conserving phonon is involved in

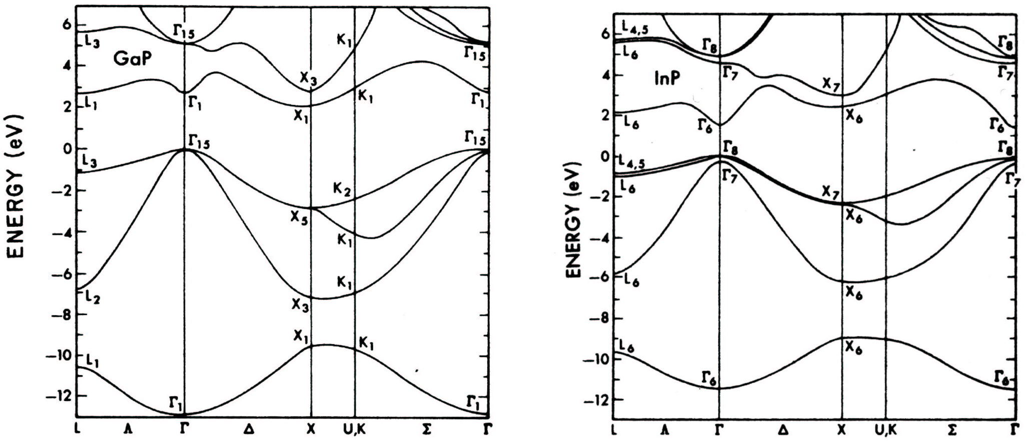

Figure 2.3: Band structures of bulk GaP and InP calculated using empirical nonlocal pseudopotential [8].

the transition between the valence band and conduction band (Γ point is not the global minimum of conduction band energy).

Figure 2.3 exhibits the band structures for bulk GaP (indirect semiconductor) and InP (direct semiconductor).

In lower-dimensional systems, spatial confinement reduces the number of degree of freedom for the carriers. In the case of quantum wells, the carrier momentum will be restricted from three to two dimensions. This results in an in-plane dispersion as for quasi-free carriers, which is given by

$$E_{plane}(\mathbf{k}_{2D}) = \frac{\hbar^2(k_x^2 + k_y^2)}{2m_{eff}} \tag{2.4}$$

and in a perpendicular quantization of the carrier energy, dependent on the confinement length L,

$$E_{n_z} = \frac{\hbar^2\pi^2}{2m_{eff}L^2} n_z^2. \tag{2.5}$$

In the case of quantum dots, three-dimensional confining restricts motion in all directions. From the substantially simplified viewpoint employing effective-mass theory with parabolic band, it becomes clear that the strong three-dimensional confinement lifts any $\mathbf{k}$ conservation in the bound states of charge carriers in an ideal quantum dot.

For a cubic quantum dot (L being dot length) with infinite barrier height the confinement energy $E_{x,y,z}$ within this quantum dot follows as:

$$E_{x,y,z} = \frac{\hbar^2\pi^2}{2m_{eff}L^2}\left(n_x^2 + n_y^2 + n_z^2\right). \tag{2.6}$$

n_x, n_y, and n_z are the quantum numbers and integer.

2.4 Density of electronic states

The density of states $\rho(E)$ is defined as the number of states per unit volume in real space, dN, per energy dE:

$$\rho(E) = \frac{dN}{dE} \tag{2.7}$$

$N(k)$, the total number of states in **k**-space per volume of real space L^3, is given by the volume of the sphere with radius **k**, divided by the volume occupied by one state in **k**-space $2\pi/L^3$:

$$N(k) = 2\frac{4\pi k^3}{3}\frac{1}{(2\pi/L)^3}\frac{1}{L^3}. \tag{2.8}$$

Thus, the density of states in the bulk solid, where the energy can be represented as a parabolic function of momentum, is given by

$$\rho_{bulk}(\mathrm{E}) = \frac{1}{2\pi^2}\left(\frac{2m_{eff}}{\hbar^2}\right)^{\frac{3}{2}} E^{\frac{1}{2}}. \tag{2.9}$$

Note that this approximation holds for quasi-free carriers and low kinetic energy around $k = 0$ of the band edges (see Sec. 2.3), but is sufficient for many effects

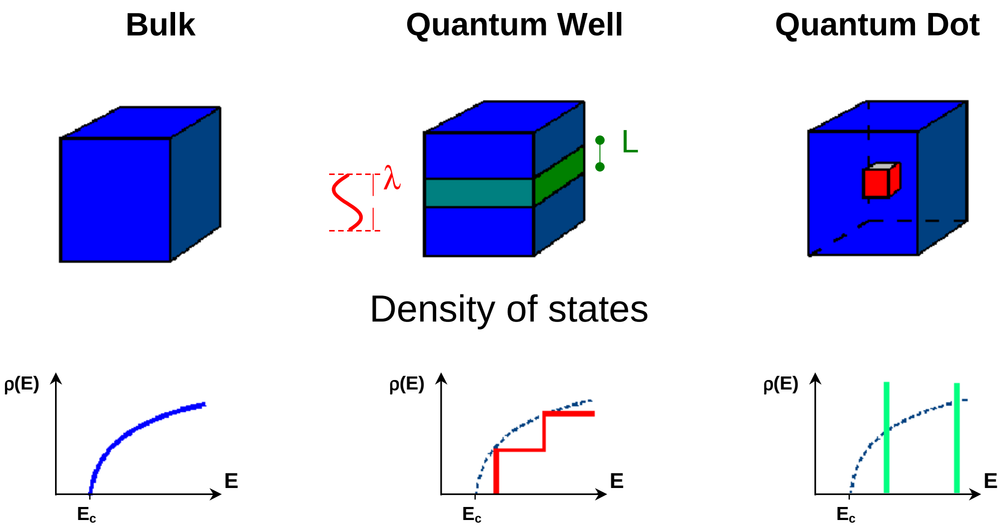

Figure 2.4: Density of electronic states in bulk material, quantum wells, and quantum dots. λ denotes the de Broglie wavelength.

to be treated with. The overall density of states function, however, is more complex for real studies.

In contrast to the bulk solid, for quantum wells only two degrees of freedom exist, therefore the electron momenta map out a circle area in **k**-space. Thus, the density of states for a single subband in a QW is given by

$$\rho_{QW}^{ssb}\left(\mathrm{E}\right) = \frac{m_{eff}}{\pi\hbar^2} \tag{2.10}$$

and, taking n subbands into account, by:

$$\rho_{QW}\left(\mathrm{E}\right) = \frac{m_{eff}}{\pi\hbar^2}\sum_{i=1}^{n}\Theta\left(E - E_i\right). \tag{2.11}$$

Θ denotes the unit step function.

In the special case of quantum dots the carriers are confined in all directions, leading to vanishing dispersion curves. Hence, the density of states is only dependent on the number of confined levels. A single isolated QD has just two states for each confined level (spin-down and spin-up), resulting in a density of states given by a series of δ-functions:

$$\rho_{QD}\left(\mathrm{E}\right) \propto \sum_{i=1}^{n}\delta\left(E - E_i\right). \tag{2.12}$$

2.5 Strain

If the semiconductors that form heterostructure have different lattice constants, strain governs in the system. Strain changes both the band structure and the band edge discontinuity at the heterointerfaces, resulting in modified optical and transport properties. The relative lattice mismatch is defined as

$$\varepsilon = \frac{a_A - a_B}{a_B} \tag{2.13}$$

where a_A and a_B are the lattice constants of materials A and B, respectively. If a_A is larger than a_B, the strain in the material A is compressive, whereas in the material B the strain is tensile. In the case of a pseudomorphic structure, material A and B are biaxially strained in the such way that in-plane lattice constant ($a_{||}$) of A is the same as that of B, while their perpendicular lattice constants ($a_{\perp}$) are different from a_A and from a_B. If the thickness of B is much greater than that of A, $a_{||}$ in both materials attains the value of a_B (see Fig. 2.5). This can be expressed by a strain tensor ϵ with parallel ($\epsilon_{||}$) and

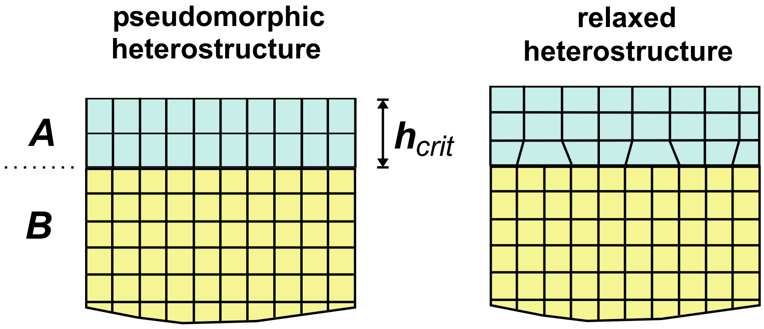

Figure 2.5: Schematic illustration of biaxially strained heterostructure: **(a)** pseudomorphic and **(b)** relaxed with interface dislocations.

perpendicular ($\epsilon_\perp$) components to the plane of the interface

$$\epsilon_\| = \frac{a_\| - a}{a} \tag{2.14}$$

and

$$\epsilon_\perp = \frac{-1}{\nu}\epsilon_\|. \tag{2.15}$$

ν denotes the Poisson ratio, a scaling factor dependent on material.

In highly lattice-mismatched systems it is not possible to realize thick pseudomorphic structures due to the large strain that will be reduced by emerging of dislocations at the interface. This occurs when the thickness of A exceeds a critical thickness h_{crit}. Hence, strain is partially relaxed (see Fig. 2.5). h_{crit} is mainly dependent on the lattice mismatch ε (for an overview see Reference [9]).

The strain in the InP QDs and surrounding $\mathrm{In}_x\mathrm{Ga}_{1-x}\mathrm{P}$ matrix has a dominant influence on the electronic structure. Strain is the main drive for the formation of self-organized quantum dots (see Sec 3.4.1). The total strain energy in the continuum mechanical model (CM) is given by [10]

$$U_{CM} = \frac{1}{2}\sum_{ijkl} C_{ijkl}\epsilon_{ij}\epsilon_{kl}. \tag{2.16}$$

The elastic moduli C_{ijkl} are represented by parameters C_{11}, C_{12}, and C_{44} for cubic crystals. The components of the strain tensor are represented by ϵ_{ij} and ϵ_{kl}. The difference in elastic constants for III-V semiconductors results in different strain energies (see Table 2.1).

Furthermore, to obtain a realistic approximation for the band alignment, we take strain effects into account by following the procedure given in Van de Walle's model-solid theory [7].

Material	C_{11}	C_{12}	C_{44}	B_s
InP	101.1	56.1	45.6	71.1
GaP	140.5	62.1	70.3	88.2
InAs	83.3	45.3	39.6	-
GaAs	119.0	53.8	59.5	-

Table 2.1: Values of elastic constants C and bulk modulus B_s in GPa unit [11].

Model-solid theory: Two main aspects of this model theory are the draft of an accurate band structure and its arrangement on an *absolute* energy scale. The band structure is calculated using density-functional calculations on bulk semiconductor. Since the calculated values are for infinite bulk semiconductor, the *vacuum level* cannot be set here as energy reference. To define the *absolute* energy scale, the solid is modeled as a superposition of neutral atoms, in each of which the electrostatic potential is defined with respect to the vacuum level. In such a way, the average electrostatic potential in this *model solid* is given with respect to the vacuum level and the absolute energy scale can be defined. Van de Walle introduced in his model E_{Vav}, the average over the three uppermost valence bands at Γ point, as the absolute energy reference.

The shift of band edge of the semiconductor under strain can also be described by the model-solid theory. Strain is given in terms of deformation potentials, whose values in semiconductors are obtained using self consistent interface calculations. The hydrostatic deformation potential a_V for the valence band expresses the change in E_{Vav} per unit fractional volume change:

$$a_V = \frac{dE_{Vav}}{d\ln\Omega}. \tag{2.17}$$

The values for the two band edges of the heterojunction are given by

$$\Delta E_{Vav} = a_V \frac{\Delta\Omega}{\Omega}, \quad \Delta E_C = a_C \frac{\Delta\Omega}{\Omega} \tag{2.18}$$

where a_V and a_C are the hydrostatic deformation potential for the valence and conduction band, respectively. $\Delta\Omega/\Omega$ denotes the fractional volume change and is given by

$$\frac{\Delta\Omega}{\Omega} = \mathrm{Tr}(\epsilon) = (\epsilon_{xx} + \epsilon_{yy} + \epsilon_{zz}). \tag{2.19}$$

According to Van de Walle's model, in the InP/GaP system with a relative lattice mismatch of about 7.7%, the strain may reduce the conduction band discontinuity by about 300 meV (see Fig. 2.6).

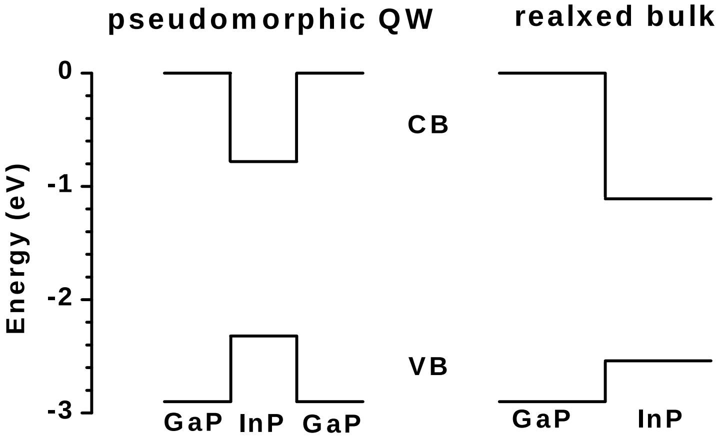

Figure 2.6: Band alignment scheme for a pseudomorphic InP/GaP QW and a relaxed InP bulk on GaP substrate calculated after Ref. [7].

2.6 Optical properties: excitons

Excitons are quasi-bound electron-hole pairs; the binding is due to the Coulomb interaction energy E_{col} between an excited electron at position $\mathbf{r}_e$ in conduction band and a hole at position $\mathbf{r}_h$ in valence band:

$$E_{col}(\mathbf{r}_e, \mathbf{r}_h) = \frac{e^2}{4\pi\varepsilon_r\varepsilon_0} \frac{1}{|\mathbf{r}_e - \mathbf{r}_h|} \tag{2.20}$$

where ε_0 and ε_r denote the dielectric constants in the vacuum and in the material, respectively.

Because the hole mass is generally much larger than the electron mass, this two-body system can be treated as a hydrogen atom. Excitons are quite stable and can have a relatively long lifetime in the order of hundreds of picoseconds up to nanoseconds. Exciton recombination is an important feature at low temperature. However, due to their low binding energy (a few meV up to a few tens of meV), they tend to dissociate at higher temperature.

The energy of excitons in semiconductors is given by

$$E_{exc} = E_{gap} + E_e + E_h + E_{col} \tag{2.21}$$

where E_e and E_h are electron and hole confinement energy.

Three regimes of confinement may be distinguished by comparing the effective radius R of quantum dot with the Bohr radii of electron a_B^e and hole a_B^h in the respective bulk material [12], given by $a_B^{e,h} = \hbar^2/(m_{eff}e^2)$, where m_{eff} is the effective mass of the CB electrons or VB holes, respectively (typically, a_B^e is larger than a_B^h):

- Weak confinement regime, $R > a_B^e$: This gives rise to a quantization of the center-of-mass motion of excitons, while the exciton binding energy E_{exc} still is mainly due to Coulomb interaction.
- Intermediate confinement regime, $a_B^e \geq R \geq a_B^h$: Mainly the electrons are quantized but not the holes. In this case, quantum confinement and Coulomb interaction have comparable influence on E_{exc}.
- Strong confinement regime, $a_B^h > R$: In this regime both electrons and holes are quantized, and E_{exc} can be strongly enlarged by the structural confinement.

Due to structural dependency of its components, the exciton energy is clearly a function of structure and material. For instance, the Coulomb interaction energy in type-II systems, where electrons and holes are localized in different layers, is much smaller than that in type-I systems. Furthermore, E_{col} depends strongly on the value of the dielectric constant, so quantum dots of same size in different material systems can belong to different confinement regimes.

In III-V compounds the bulk exciton radius is typically greater than 10 nm. Hence, only for those III-V quantum dots with a size smaller than 10 nm, or having about that size and sufficiently deep potential, the excitons belong to strong confinement regimes.

Chapter 3

Growth of quantum heterostructures

3.1 Introduction

The growth of properly designed semiconductor structures is the first technological step in the production process of optical and electronic devices. Due to the development of modern epitaxial growth methods such as molecular-beam epitaxy (MBE), liquid-phase epitaxy (LPE), and chemical vapor deposition (CVD) in recent years, the accurate preparation of low-dimensional semiconductor heterostructures has become feasible.

This chapter includes the most important aspects of growth of low-dimensional heterostructures using MBE. In Section 3.2 a general description of molecular-beam epitaxy is given and other growth methods in comparison to MBE are discussed. The section concludes with the description of our own growth facility, which is a gas-source molecular beam epitaxy (GSMBE) system. Section 3.3 focuses on kinetic and surface aspects of molecular-beam epitaxy. Because this work concerns lattice-mismatched systems, Section 3.4 serves to demonstrate heteroepitaxial growth in such systems. The growth of self-organized quantum dots will be discussed in particular.

3.2 Molecular beam epitaxy

Molecular beam epitaxy is a versatile method for growing thin monocrystalline films, called epitaxial films or epilayers. The epitaxial growth occurs due to physical and chemical interaction between thermal-energy molecular or atomic beams of the constituent elements and a substrate surface in ultrahigh vacuum.

Variations of MBE include solid-source MBE, hydride-source MBE, gas-source MBE, and metal-organic MBE. Other approaches to epitaxial growth are liquid-phase epitaxy (LPE) or chemical vapor deposition (CVD). The latter method includes hydride CVD, trichloride CVD, and metal-organic CVD (MOCVD).

When epilayer and substrate have the same chemical composition, the growth is called *homoepitaxy*; when the epilayer grows on a substrate with different chemical composition, the growth is called *heteroepitaxy*. MBE allows to change the chemical composition of heteroepitaxial films over several Ångstroms and to grow atomic layer by atomic layer. Furthermore, growth of films with sharp doping profiles is possible [13, 14].

The chemical composition and doping level of epilayers depend on the arrival rates of the constituent elements that are thermally vaporized from effusion cells. Consequently, the arrival rate itself is dependent on the temperature of sources that are stored in Knudsen-type crucibles. To start and stop the deposition of elements, simple mechanical shutters in front of the Knudsen-effusion cells are used (see Fig. 3.1). The ideal Knudsen cell should contain vapor and condensed phase in equilibrium.

In contrast to other epitaxial growth techniques, such as vapor phase epitaxy and liquid phase epitaxy, due to ultrahigh vacuum condition maintained in MBE, this epitaxy occurs far from thermodynamic equilibrium and is mainly

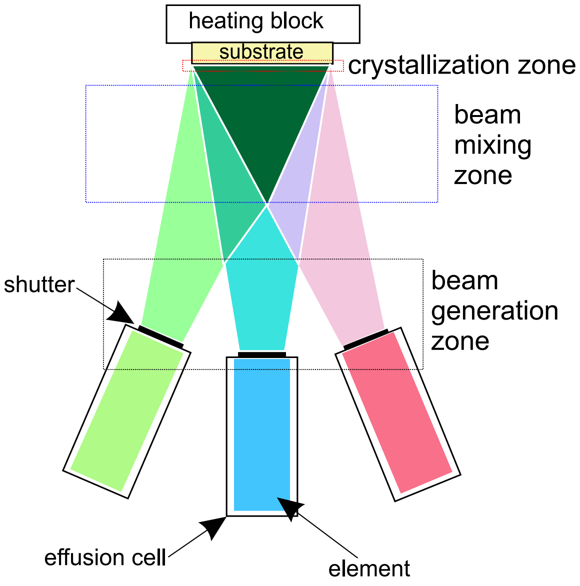

Figure 3.1: Schematic illustration of the essential parts of a MBE growth system.

governed by the kinetics of the surface process. Further advantage of MBE is that the ultrahigh vacuum environment allows to control the growth *in situ* via surface analysis techniques such as reflection high-energy electron diffraction (RHEED). In the next section the ultrahigh vacuum environment will be discussed in detail.

3.2.1 Ultrahigh vacuum environment

In ultrahigh vacuum (UHV) environment (background pressure lower than 10^{-9} Torr) the influence of the residual gas or of the adsorption of contaminants can be neglected. The reason is the very low impinging rate due to low ambient pressure p_a, leading to the possibility of growth of well-defined surfaces. p_a determines how many particles of the residual gas impinge on a surface area of 1 cm^2 per second and is proportional to the temperature T (in Kelvin), to the impinging rate r, and to the inverse average thermal velocity $\langle v \rangle$ of the gas atoms or molecules:

$$p_a \propto T \frac{r}{\langle v \rangle}. \tag{3.1}$$

Typical UHV equipment for MBE consists of stainless UHV chambers (for epitaxy, preparation, structural analysis, etc.), the pumping part including several different pumps, and pressure gauges.

For optimal epitaxy a background pressure in the order of 10^{-10} Torr is necessary. Due to limitation of the operation pressure range of each pump type, a combination of different pumps is required. Figure 3.2 shows the operation pressure ranges for different pump types.

3.2.2 Gas source molecular beam epitaxy

Conventional MBE of III-V compounds is usually done with solid sources (SSMBE) for all elements, but the use of solid sources for group-V materials has several disadvantages, for instance:

- rapid depletion of sources
- beam flux variation with time
- Solid phosphorus consists of mixed allotropic phases with different vapor pressures. This may cause difficulties in controlling beam intensity.

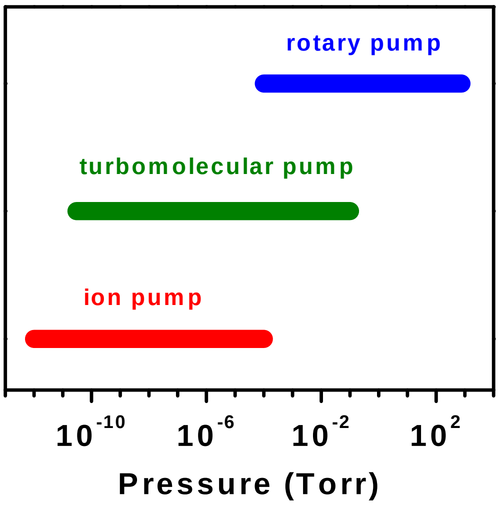

Figure 3.2: Operation pressure ranges for three different pumps.

In the early 1980s, it became known that the use of gas sources for the group-V elements rather than solid sources can eliminate these disadvantages and improve conventional solid source MBE [15,16,17]. The modified epitaxial growth technique developed thereafter is gas source MBE (GSMBE), employing solid sources for group-III elements and gaseous sources for group V (group-V hydrides). Arsine (AsH_3) and phosphine (PH_3) are thermally decomposed in a cracking cell at sufficiently high temperatures. The decomposition products are the possible stable gas species of arsenic and phosphorous: Monomer (M), dimer (M_2), and tetramer (M_4) molecules, together with MH_2, MH, atomic and molecular hydrogen (H and H_2), where M denotes the arsenic (As) or phosphorous (P) atom. The relative amounts of species depend on the temperature and pressure. The most important species are the dimers, whose concentration is nearly independent of cracking temperature between 600°C and 1200°C, as demonstrated by Jordan et al. for GSMBE [18]. On the other hand, as the temperature rises, the concentration of tetramers declines: At 600°C the ratio of M_2 to M_4 is about unity, whereas at 800°C it is more than two orders of magnitude higher [18]. Thus, a higher cracking temperature can produce a higher M_2/M_4 ratio in the gas flux. It is well known that dimers are chemically more reactive than tetramers [19,20] and dimers have an accommodation coefficient near unity [16]. Hence, any alteration of M_2/M_4 may modify the chemical composition of a growing crystal structure, resulting in a change in optoelectronic properties [20].

At 800°C the concentration of species containing hydrogen is five to eight orders of magnitude lower than that of dimers [18].

All structures for this study were grown using GSMBE in a modified RIBER-32-P MBE system. Our MBE system consists of two UHV chambers: the intro chamber (IC), being used for loading and required surface preparation of the substrate and the growth chamber (GC). In the growth chamber the most important parts for epitaxy are embodied: beam sources (Knudsen cells and cracking cell) with their individual shutters, the substrate holder (manipulator) with heater, the electron gun and fluorescent screen of the RHEED system, the ion gauge, the pyrometer, and the quadrupole mass spectrometer. To hold the impurity at the lowest level, the growth chamber and the sources are surrounded by a liquid-nitrogen cooled cryopanel (see Fig. 3.3).

Six Knudsen cells contain solid sources:

- three group-III elements: gallium (Ga), indium (In), and aluminum (Al)
- one group-V element: arsenic (As)
- one group-II element, used as p-dopant: beryllium (Be)
- one group-IV element, used as n-dopant: silicon (Si)

A low-pressure high-temperature cell is used for cracking of both gases AsH_3 and PH_3. The cracking temperatures for AsH_3 and PH_3 are usually 830°C and 850°C, respectively, resulting in cracking efficiency higher than 90% [19]. The fact of both gases sharing the same port leads to some difficulties in controlling the interface during heteroepitaxy of structures with alternating group-V elements (see Sec. 5.2.1).

All cells contain thermocouples, which are controlled by temperature EuroTherm regulators, based on proportional-integral-derivative (PID) controllers with self-calibration function [22].

The temperature of the substrates is controlled with the same type of thermocouple mounted on the substrate holder. Additionally, a pyrometer, which is calibrated for GaAs, allows to control the radiation temperature of substrates.

In order to obtain an homogeneous surface, a motor rotates the substrate holder during growth.

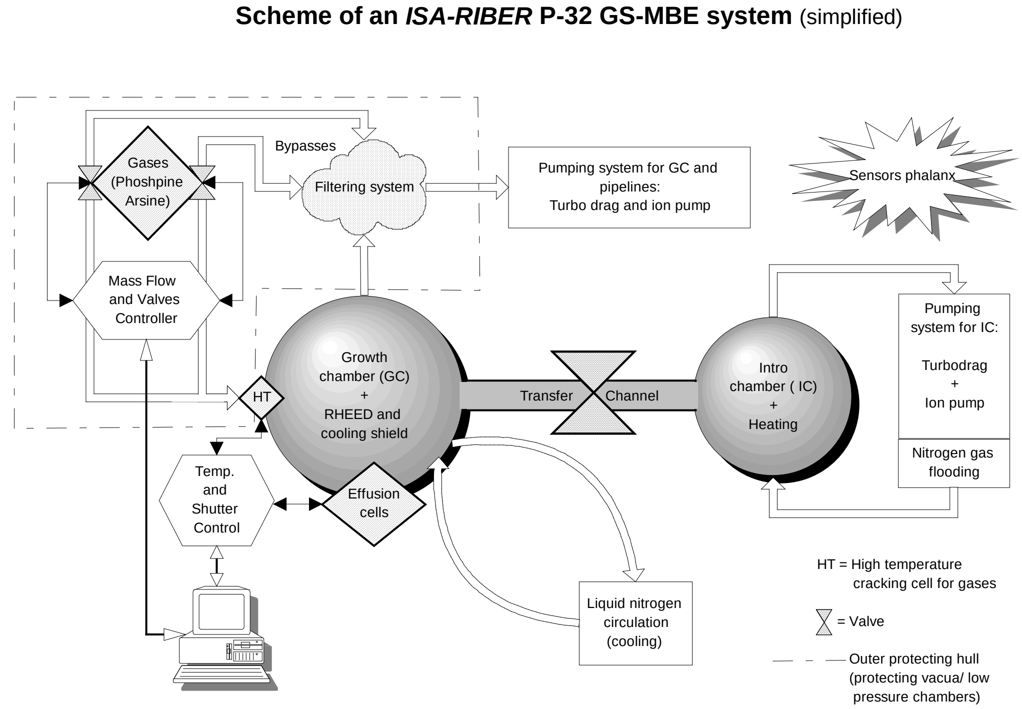

Figure 3.3: RIBER32 [21]

Pre-Growth

Only if the substrate surface is free of contamination, epitaxial growth is possible. Therefore, prior to loading the substrate into the MBE machine, the surface is usually cleaned using organic solutions (thrichlorethylen, acetone, and methanol), followed by etching in proper solutions, dependent on the kind of substrate (see Chapters 5 and 6). After this preparation, the substrate is ready for loading into the IC, where, for further cleaning, it is heated for at least one hour at about 200°C. The last step of cleaning is removal of oxide layer from the surface and done in the growth chamber by heating under continuous V-elements beam at a temperature between 550 and 630°C.

Growth rate

The growth rate of each solid element (group III and dopants) is a function of its effusion-cell temperature, and is given by

$$R(T) = \exp \frac{T - T_0}{S}. \tag{3.2}$$

T_0 depends on the element and its physical state (for instance, its amount in the effusion cell), whereas S is nearly constant and depends on the geometry of the growth chamber and the cell. To obtain Ga and Al growth rates,

$Al_xGa_{1-x}As/GaAs$ superlattices at various Al and Ga cell temperatures are grown and analyzed by X-ray measurements, yielding the period and thickness of the layers (analogous to this we can use $Al_xGa_{1-x}P/GaP$ superlattices); indium growth rate can be determined by epitaxy of bulk $In_xGa_{1-x}P$ on GaAs, followed again by X-ray analysis of structures, after optimization of Ga growth rate (see Sec. 5.2.2). To appoint the growth rate of both dopants Be and Si, doped bulk GaAs is grown, and the carrier concentration in the structures is measured (see Sec. 4.4).

3.3 Kinetic and surface aspects of MBE growth

The MBE arrangement can be divided into three zones: The first zone is the generation zone of the atomic and molecular beams (in front of the cells). The second zone is where the different beams intersect each other and the vaporized elements mix (on the way from the cells to substrate surface). The third zone is on the substrate surface, where the crystallization process takes place (see Fig. 3.1).

The important stage for epitaxial growth occurs in the third zone on the substrate surface. The most influential surface processes are:

- adsorption of the impinging atoms or molecules
- surface diffusion
- nucleation
- diffusion into the crystal
- desorption of the atoms that do not incorporate into the crystal.

All these processes are critically dependent on the physical and chemical state of the growth surface.

The molecular or atomic beam arrives at the surface with an impinging rate r, which describes the number of particles impinging on the unit area of the surface per second:

$$r = \frac{p}{\sqrt{2\pi M k_B T_e}} \tag{3.3}$$

where p is the vapor pressure, M the particle mass, and T_e the source temperature.

There are two types of adsorption: physical adsorption and chemical adsorption. Physical adsorption, called physisorption, is a process in which no electron

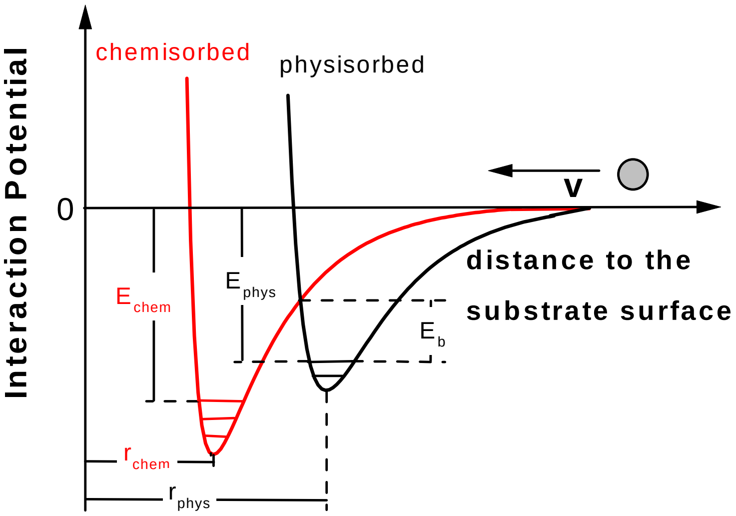

Figure 3.4: The interaction potential between the substrate surface and one free atom impinging perpendicularly to the surface for chemisorbed and physisorbed states [14]

transfer between the adsorbate and the adsorbent occurs. The corresponding mechanism is van der Waals bonding. In contrast, chemical adsorption, called chemisorption, is an adsorption process that resembles the formation of covalent or ionic bonds. In this case, electron transfer between the adsorbate and the adsorbent takes place.

Generally, physisorption potentials are characterized by a lower binding energy compared to chemisorption potentials (see the depth of the potential wells in Fig. 3.4). Atoms arriving at the surface first undergo physisorption; in a second step, chemisorption incorporates the atoms into the crystal surface.

To obtain smooth surface, the thermodynamic conditions must lead to a sufficiently high surface mobility of the diffusing particles, which is achieved by setting growth rate slow and the surface temperature sufficiently high so that kinetic processes are rapid [14, 23, 24].

In thermodynamic equilibrium all kinetics would proceed in two opposite directions at equal rates, resulting in zero net growth. Thus, crystal growth is a nonequilibrium kinetic process, and a global theory of film growth is more difficult, as it must include the rate equation for each possible effect. The next section will focus on the phenomenology of film growth.

Surface reconstruction: One speaks of surface reconstruction, if the periodicity of epilayer parallel to the surface differs from that of bulk. Otherwise, the surface is called relaxed (see Sec. 2.5). The reason for surface reconstruction are *dangling bonds* of surface atoms, which enlarge the in-plane real-space lattice in order to stabilize the surface. The new periodicity results in additional reflections (fractional-order reflection) between main reflections (integral-order reflections) that appear due to the periodicity of underlying bulk atoms. Hence, the surface reconstruction (size and symmetry of the surface lattice) can be determined directly by reflection high-energy electron diffraction pattern (see Sec. 4.2.1). As defined, for a (m×n) reconstructed surface the two perpendicular in-plane real-space lattice distances are m and n times larger, respectively, than the bulk lattice constants.

3.4 Growth in lattice-mismatched systems

Heteroepitaxial growth can be classified in three different modes: Frank-van der Merwe (FM) [25], Volmer-Weber (VW) [26], and Stranski-Krastanow (SK) [27]; they represent two-dimensional planar growth, three-dimensional island growth, and planar-plus-island growth, respectively. In lattice-mismatched systems the surface and interface energies as well as the lattice-mismatch determine the particular growth mode, whereas in lattice-matched systems the energies alone regulate the growth behavior.

All of these various growth modes can be modeled by the characteristic free energy G in substrate–epilayer system, given by the sum of epilayer surface energy E_e and of the substrate–epilayer interface energy E_{se}:

$$G = E_e + E_{se}. \tag{3.4}$$

These energies are related to surface tensions γ. Due to the definition of tension as force per unit length of boundary, force equilibrium at a point where the substrate contacts the epilayer can be depicted as follows (see Fig. 3.6):

$$\gamma_s = \gamma_{se} + \gamma_e cos\theta. \tag{3.5}$$

θ denotes the contact angle. γ_s, γ_{se}, and γ_e are substrate-surface tension, substrate–epilayer interface tension, and epilayer-surface tension, respectively. If $\gamma_e + \gamma_{se}$ is less than the tension of the substrate surface γ_s, the interaction between substrate and epilayer atoms is weaker than that between substrate

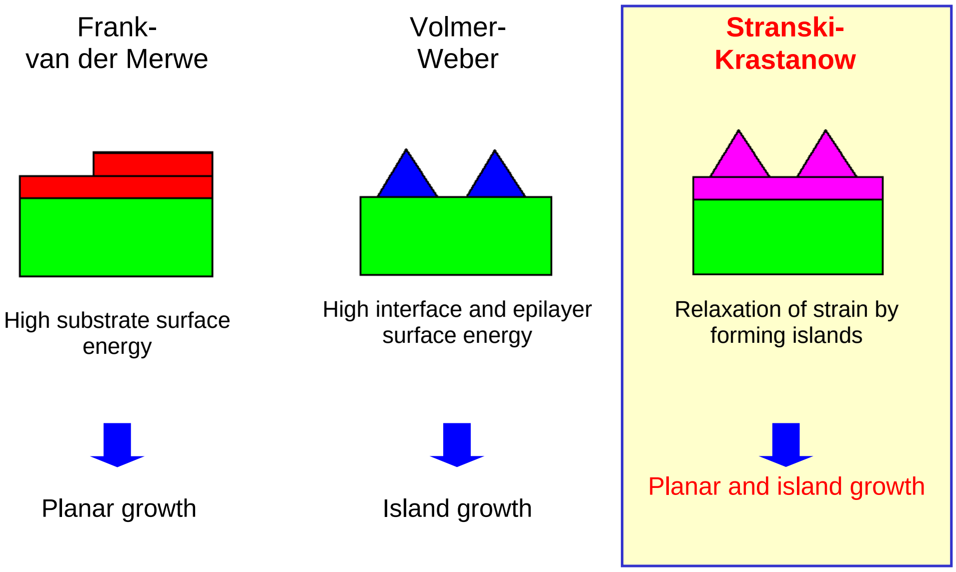

Figure 3.5: Schematic illustration of three possible growth modes: planar growth (Frank-van der Merwe), island growth (Volmer-Weber), and planar plus island growth (Stranski-Krastanow).

atoms; thus, the two-dimensional FM mode appears. A rise in $\gamma_e + \gamma_{se}$ leads to the opposite case, resulting in the three-dimensional VW growth mode [28, 29]:

$$\text{layer growth (FM)} : \gamma_e + \gamma_{se} \leq \gamma_s \tag{3.6}$$

$$\text{island growth (VM)} \ : \gamma_e + \gamma_{se} > \gamma_s \tag{3.7}$$

For a highly strained epilayer with a small interface energy only initial growing may appear planar (wetting layer); growth of thicker strained two-dimensional layers leads to a large strain energy in the system that discharges by formation of islands. This mode of self-organized island growth is Stranski-Krastanow, and in such way the growth of *coherently* (dislocation free) strained islands is possible.

Today, Stranski-Krastanow growth is the commonly used method for the formation of quantum dots. The InP QDs investigated in this work were fabricated accordingly. In the next section this growth mode will be discussed in detail.

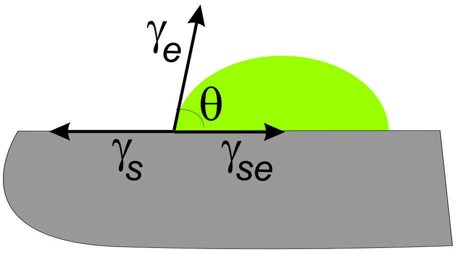

Figure 3.6: Schematic illustration of surface and interface tension terms for an island in its equilibrium shape. For layer growth: $\theta = 0$.

3.4.1 Growth of quantum dots

SK growth mode in the equilibrium model

Although for a precise theory of quantum-dot growth both equilibrium and nonequilibrium effects must be taken into consideration, most of the existing theories are based on the equilibrium condition [30, 31, 32, 33], in which the material exchange between the islands is negligible against the diffusion of atoms into a single island. In the equilibrium theory of the Stranski-Krastanow growth mode [30] the total energy of an island with size L can be described via the short-range energy of the island facets (E_{facets}), the change in the surface energy of the island ($\Delta E_{surface}$), and the elastic relaxation energy, which is proportional to the volume of island ($-E_{relax}$):

$$E_{island} = E_{facets} + \Delta E_{surface} - E_{relax}. \tag{3.8}$$

All of these energies are function of island size, and their size dependence are given as follows:

$$E_{facets} \propto L, \qquad \Delta E_{surface} \propto L^2, \qquad -E_{relax} \propto L^3. \tag{3.9}$$

When $\Delta E_{surface}$ is positive, a coherent island can be formed and the critical island size $\mathrm{L_{crit}}$, for which the increasing surface energy and the decreasing volume strain energy are balanced, can be derived from the condition $dE(L)_{island}/dL = 0$. If the size of the island exceeds this critical size, further growth of this island is energetically convenient. Thus, *Ostwald ripening* [34] occurs. This behavior can be explained as follows: To reduce the overall surface of the large islands and, hence, to lower the total surface energy of the system, the coherent small islands of a size greater than the critical size of $\mathrm{L_{crit}}$ conglomerate (Ostwald ripening) forming larger islands [35]. Additionally,

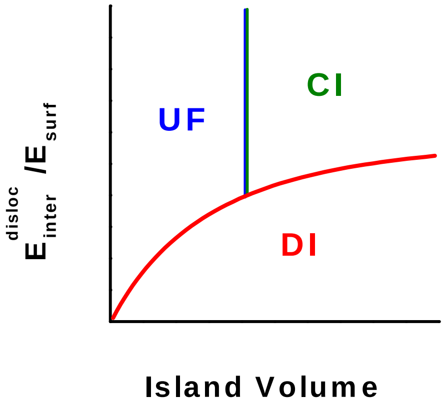

Figure 3.7: Schematic phase diagram as a function of the island volume and the ratio of dislocated interface energy to excess surface energy $E_{inter}^{disloc}/E_{surf}$ with the favorite morphology regimes: uniform film (UF), coherent island (CI), and dislocated island (DI) [36].

the relaxation energy is strongly dependent on the island shape, including its facets and its dimension; if the island becomes larger than $\mathrm{L_{crit}}$, its volume enlargement results in a very high E_{relax} that may diminish by introduction of dislocations [36, 37], or shape transition [38, 39].

Although the equilibrium model is able partly to delineate the nature of island growth, experimental studies of Stranski-Krastanow islands in several material systems have shown that control of island properties is more difficult. This will be discussed now.

Growth of self-organized quantum dots

Fabrication of self-organized quantum dots via the coherent island Stranski-Krastanow growth has been realized in numerous material systems and using different epitaxy methods (for an overview see Reference [40]). Advantageous for QD-based optoelectronic devices is the formation of coherent quantum dots. Thus, the island volume must be small enough so that the strain energy does not generate dislocations. Furthermore, dense ordered arrays of uniform quantum dots are required. The size, shape, density, and orientation of self-organized SK QDs can be affected by a variety of growth conditions. To determine in which way the growth conditions impact the formation of quantum dots, many studies have been done:

Effect of deposition thickness: The SK QD formation appears after the highly strained, two-dimensional wetting layer exceeds a critical thickness d_{crit} (2D–3D transition); this is strongly dependent on the misfit of the material system, but it can also be affected by other growth conditions such as growth temperature. If the thickness of a strained layer is smaller than d_{crit}, formation of elongated, wire-like islands may occur [41]. After dot formation, further material deposition usually leads to higher dot density and larger islands [42,43].

Effect of deposition rate: Johansson et al. [44] have investigated the growth of InP-MOVPE quantum dots on $In_{0.48}Ga_{0.52}P$ for different InP deposition rates. According to their observation, the dot density becomes higher with increasing deposition rate. Actually, for low deposition rates the density is linearly proportional to the deposition rate, whereas for high deposition rates a saturation effect of density is observed [44].

Effect of growth temperature: For numerous material systems the effect of growth temperature on the dot size and density has been studied. Common observation is that with lower growth temperature the dot density increases [45, 44, 43] and smaller dots can be grown [45, 46, 47, 43]. Consequently, at even more reduced growth temperature the dot formation may be suppressed. Furthermore, shape transition of QDs in the InAs/GaAs system at higher growth temperature has been reported [48].

Effect of III/V ratio: Investigation of $InP/In_{0.48}Ga_{0.52}P$ quantum dots grown by MBE with different III/V ratios exhibits that higher phosphorus pressure (lower III/V ratio) results in more homogeneous dot arrays with lower density. This decrease in the dot density is accompanied by an increase of the dot size, involving a shape transition of dots [49]. Apparently, lower III/V ratio enhances the ripening rate, which has also been observed for InP/GaP MOVPE QDs [47]. The same behavior has been reported for MOCVD $In_xGa_{1-x}As/GaAs$ and $Al_xIn_{1-x}As/AlAs$ [43, 50], and for MBE-$In_xGa_{1-x}As/GaAs$ QDs [51]. Besides, larger critical thickness for 2D–3D transition at lower III/V ratios is observed [50].

Effect of growth interruption: In order to achieve uniform dot arrays it is necessary to introduce a growth interruption after deposition of enough dot material. This interruption is the dot formation time. Ideally, in this time the dots reach their equilibrium shape and size and the growth of large clusters will be impeded. Enhancement of dot formation due to growth interruption is reported in several works [51, 52].

Effect of substrate off-angle orientation: The dot density, shape, and size are critically dependent on substrate off-angle orientation. Dot formation can be expedited by choice of substrates with higher off-angle orientation, causing an increase of dot density and a reduction of dot size [45, 43].

Effect of cap-layer growth temperature: A dependence on growth temperature during epitaxy of cap-layer has been observed for MOVPE-InAs/GaP QDs [53]; higher growth temperature results in larger QDs due to the coalescence of small InAs QDs. In this case, the best structural quality (small dots and a flat GaP surface) could be realized via a two-stage cap-layer growth. Starting with a lower temperature (same value as for the InP dots), the temperature was then increased for a good quality of the GaP cap layer [53].

Chapter 4

Characterization methods

4.1 Introduction

Today, we are able on a high measure to understand and explain the behavior of quantum structures using modern analysis and characterization methods. This chapter focuses on structural, optical, and electrical techniques that have been used to analyze the samples for this work.

In the next section the structural characterization methods will be discussed. Section 4.3 provides information about the basics and setups of optical measurements. Finally, the electrical characterization methods will be introduced in Section 4.4.

4.2 Direct and indirect structural characterization

Structural properties of quantum structures can be studied using two groups of imaging methods: *indirect* and *direct* imaging. Indirect imaging methods provide information on reciprocal space, whereas the direct methods image the structure in real space. Section 4.2 surveys indirect and direct techniques that are used to analyze the structural properties of the samples.

4.2.1 Reflection high-energy electron diffraction

Reflection high-energy electron diffraction (RHEED) is one important *in situ* surface characterization method. High-energy electrons (10 keV in our RHEED setup) are incident under a small angle (1°–3°) onto the sample surface and the uppermost atomic layers; the diffracted beams are observed on a fluorescent screen forming a characteristic diffraction pattern, which can be explained as follows:

The de Broglie wavelength λ_e of electrons with 10 keV kinetic energy E_{kin} is about 0.12 Å (λ_e= 12.2Å $/\sqrt{E_{kin}(eV)}$), resulting in a Ewald sphere with radius about 50 Å^{-1} ($k = 2\pi/\lambda_e$). This radius is 50 times larger than the typical reciprocal constant of III-V semiconductors. Considering the surface of a crystal, the corresponding image in **k**-space is a bunch of parallel lattice rods having infinite extension perpendicular to the surface (see Fig. 4.1). At points, where these rods intersect the Ewald sphere, the maximum of interference condition as well as energy conservation is fulfilled. Thus, ideally, the diffraction pattern of a flat surface must consist of sharp spots aligned in a semi-circle, to be seen on the fluorescent screen. However, the energy spread of the incidence beam and the deviation of real crystal from the translation symmetry in the surface cause a finite "thickness" of both the Ewald sphere and the reciprocal lattice rods. Therefore, the diffraction pattern of flat surface usually consists of streaks, the maximum of intensity for each of which marks the intersection with the Ewald sphere [14].

Because the number of scattering centers (surface atoms) in the case of *surface scattering* is small, the loss of energy of the incident beam can be neglected, and formation of RHEED pattern may be described in the first approximation by the kinematic theory of diffraction. Although, if the surface is not flat and there is some three-dimensional morphology, the incident beam loses part of its energy due to electron transmission diffraction — and *bulk scattering* occurs [24]. As a result, the streaky reflection pattern from flat surface will be dominated by spots (see Fig. 4.2). Hence, growth of quantum dots can be identified through the according change in RHEED pattern. Additionally, the RHEED pattern

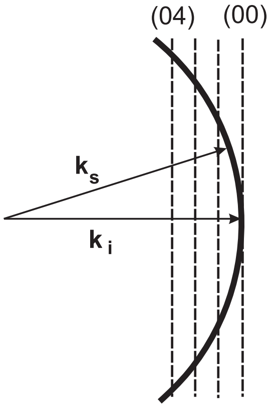

Figure 4.1: Schematic Ewald sphere for RHEED. $\mathbf{k_i}$ and $\mathbf{k_s}$ are primary and scattered wavevectors, respectively.

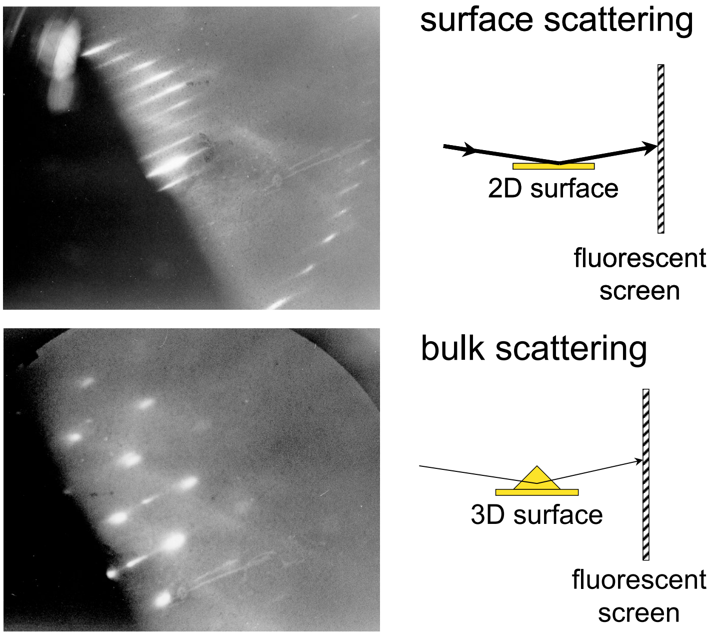

Figure 4.2: RHEED pattern [54] from: Two-dimensional growth (surface scattering) and three-dimensional growth (bulk scattering).

can supply information about the shape and faceting of quantum dots [55, 48].

4.2.2 Double-crystal X-ray diffraction

Double-crystal X-ray diffraction (DCXD) is a powerful post growth method for structural characterization of heterostructures and can provide information on quality, thickness, chemical composition, strain, orientation, and relaxation of epilayers.

The basic principle of DCXD is scattering of incident monochromatic (char-

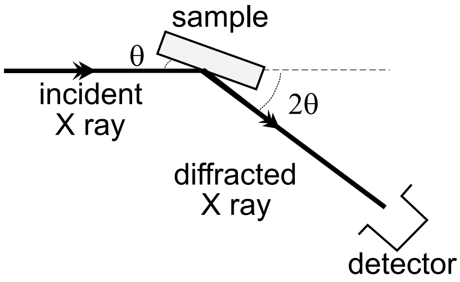

Figure 4.3: Basic setup of X-ray diffractometer. 2θ is the angle between the incident and diffracted X-ray beam.

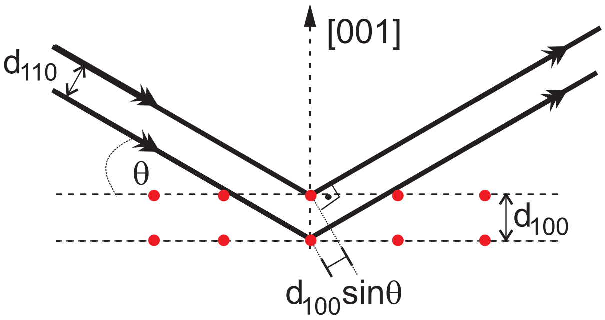

Figure 4.4: Schematic illustration of X-ray diffraction by atomic planes in a cubic crystal.

acteristic) X rays by the atomic planes of the bulk crystal. This may lead to a complex diffraction pattern. At points of constructive interference, a diffraction peak appears in a scanning detector (Fig. 4.3). In kinematic theory, the Bragg law gives the condition for maxima of diffracted intensity to occur:

$$n\lambda = 2d_{hkl}\sin\theta \tag{4.1}$$

where n is the integer diffraction order, λ and d_{hkl} denote the wavelength of X ray, and the spacing between hkl lattice planes, respectively. θ is the angle of incidence of the beam on the diffracting planes (see Fig. 4.4). For cubic crystals, d_{hkl} is given by

$$d_{hkl} = \frac{a_0}{\sqrt{h^2+k^2+l^2}}, \tag{4.2}$$

a_0 being the lattice constant. Elastic strain changes d_{hkl} and shifts the diffraction peak position; from this shift the lattice mismatch between the epilayer and substrate in a pseudomorphical structure can be calculated by

$$\frac{\Delta a}{a_\perp} = -\Delta\Lambda\cot\theta_B. \tag{4.3}$$

$\Delta\Lambda$ is the angular distance between the substrate peak and the epilayer peak; θ_B is the Bragg angle from Equation 4.1.

The non-uniform strain in, and the finite size of layers cause a broadening of the diffraction peak growing with sinθ. Hence, layer size can be determined by analyzing peak shape and peak width $W_{2\theta}$. Using DCXD measurements for several diffraction orders, it is possible to determine the strain and the size effect separately. If there is non-uniform strain in the layer, the layer thickness can be estimated by

$$L \approx \frac{\lambda}{W_{2\theta}\cos\theta}. \tag{4.4}$$

For calibration of Ga and Al growth rates we normally use $Al_xGa_{1-x}As$/GaAs superlattices (see Chapter 3.2.2). According to the Bragg law, considering the $(n+1)$-order satellite peak θ_{SL}, the thickness of the superlattice period T is given by

$$T = n\frac{\lambda}{2\sin\theta_{SL} - 2\sin\theta_n}. \tag{4.5}$$

For zero-order peak, $\theta_{SL} = \theta_B + \Delta\theta$ and $\theta_n = \theta_B$. $\Delta\theta$ denotes the average distance between satellite peaks. Using Taylor series expansion, Equation 4.5 can be given approximately by

$$T \approx \frac{\lambda}{2\Delta\theta\cos\theta_B}, \tag{4.6}$$

which we used for estimation of superlattice periodicity.

Of course, the approach of kinematic theory for X-ray diffraction in a real crystal is not sufficient and for an exact analysis of X-ray measurements a more comprehensive theory is required. The RADS (rocking curve analysis by dynamical simulation) software [56] used for examination of rocking curves in this work is based on the generation diffraction theory from Takagi [57,58] and Taupin [59]. This dynamic theory applies the two-beam approximation and describes the field within the crystal as differential form of total amplitude of incident and diffracted X-ray waves. Thereby it allows to depict the passage of X rays through a crystal with any kind of distortion.

All DCXD spectra are examined using a Bede QC1a diffractometer [60]. X rays are generated by focusing an electron beam (I_{max}=1 mA, V_{max}=50 kV) onto a copper block, producing Cu Kα_1 and Kα_2 radiation with a wavelength of λ=1.54 Å. A (001)-GaAs *reference crystal* is used as beam conditioner for supply of monochromatic beams ((004) reflections) with an approximate cross-section of 0.5×3.0 mm^2.

It should be noted that for rocking curve analysis of the samples containing quantum dots, the QDs "layer" is treated as two-dimensional layer, in such a way that its average thickness results from the height of the dots and the wetting layer; its material composition is estimated by both the material of dots and of their spacing layer (matrix).

4.2.3 Grazing incidence small-angle X-ray scattering

The grazing incidence small-angle X-ray scattering (GISAXS) technique is based on small-angle X-ray scattering [61] and total external reflection [62]

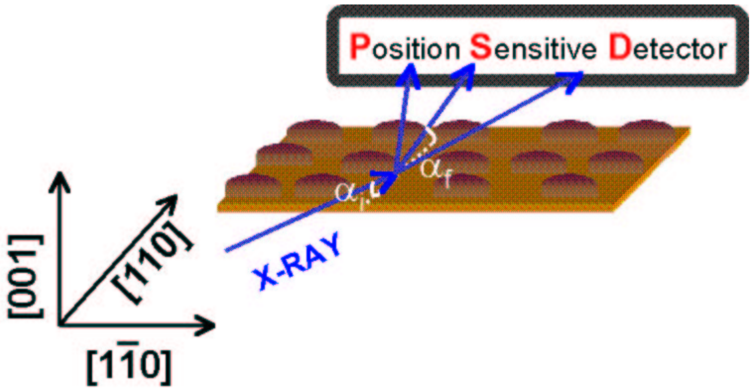

Figure 4.5: Basic setup of GISAXS experiment.

methods, and allows to determine in-plane electron density fluctuations in the nanometer up to the micrometer range, providing information on surface morphology in reciprocal lattice space [63].

To study lateral ordering effects of quantum dots, we have performed GISAXS experiments at the W1 and BW2 wiggler beamlines at HASYLAB/DESY using a photon energy of 8 keV at X-ray wavelengths of $\lambda = 1.550$ Å and 1.378 Å, respectively, with a typical bandwidth of typically $\Delta\lambda/\lambda = 10^{-4}$; a lateral resolution of about $\Delta q = 6.0 \times 10^{-4}$ Å^{-1} was achieved. GISAXS signal stems mainly from spatial correlation effects and island shape. In order to be able to characterize the surface, the X-ray angle of incidence was chosen close to the critical angle for total external reflection, $\alpha_i = 0.25°$ (grazing incidence). The specularly reflected beam as well as the scattered intensity distribution in the lateral direction was recorded by a linear position-sensitive detector (PSD). To align the scattering vector along different crystallographic directions, the sample was rotated azimuthally [64].

4.2.4 Grazing incidence X-ray diffraction

In contrast to GISAXS geometry, in which the detected signal exclusively stems from spatial correlation effects and island shape, the grazing incidence X-ray diffraction (GID) is mainly sensitive to strain inside the surrounding matrix lattice and inside the QDs themselves. Similarly to the GISAXS measurements, the angles of incidence and exit are here in the range of the critical angle of total external reflection. Hence, the sensitivity to the thin InP/$In_xGa_{1-x}P$ layers is largely enhanced as compared to conventional X-ray diffraction.

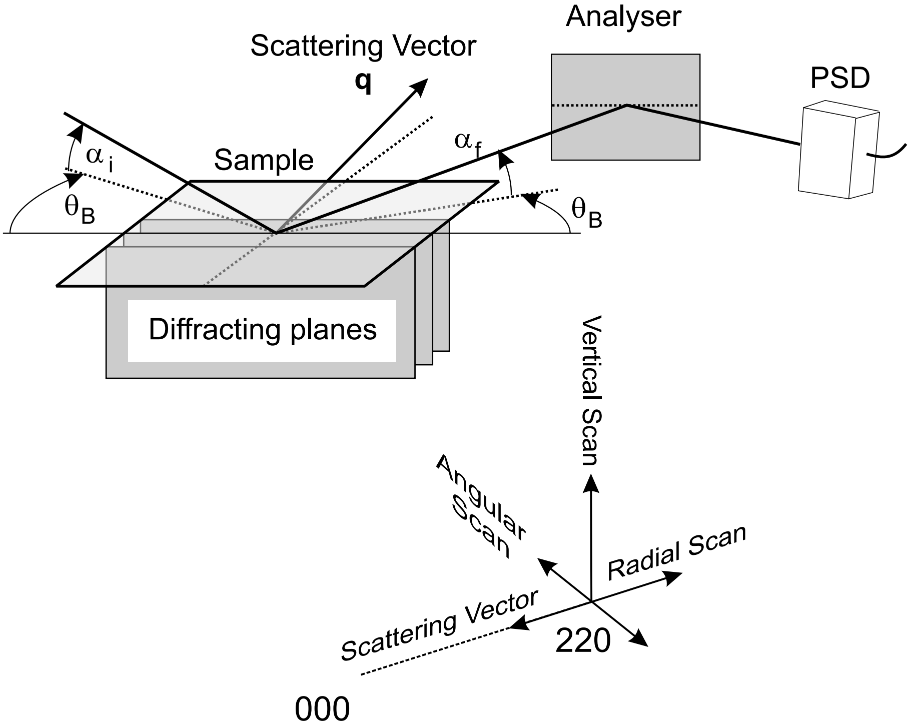

Figure 4.6: Illustration of scattering geometry of GID together with three scanning directions with respect to the scattering vector **q**: angular, radial, and vertical.

Samples have been measured using GID experiments again at the W1 and BW2 wiggler beamlines at HASYLAB/DESY. A linear position-sensitive detector (PSD) was placed about 800 nm behind the sample. At the front and the back of the evacuated detector flight tube the scattered wave is collimated by narrow slits. This setup ensures three-dimensional mapping of the diffuse intensity distribution in the vicinity of an in-plane reciprocal lattice point. Figure 4.6 schematically shows the scattering geometry and possible scan directions [64].

4.2.5 Diffuse X-ray scattering

Likewise, diffuse X-ray scattering experiments have been done at the BW2 wiggler beamline at HASYLAB/DESY under the same radiation condition as explained above. A PSD with a spatial resolution of about 80 μm was placed 800 nm behind the sample in such a way that different scattering angles 2Θ with respect to the incidence beam correspond to different channels of the PSD. Hence, the PSD works as analyzer of the scattered beam direction with a typical resolution of $\Delta q/q = 5 \times 10^{-4}$. This value is sufficiently small to ensure that all relevant diffraction features originating from the strained layer can be resolved. By tilting either the sample (ω scan) or, alternatively, both sample and PSD in 1:2 coupling ($\omega - 2\Theta$), a complete two-dimensional map of reciprocal space can be measured in single scan [64].

4.2.6 Scanning electron microscopy

Scanning electron microscopy (SEM) operates using secondary electrons for imaging of the surface structure in real space. The surface is scanned by a primary electron beam with typical energy of about 2–50 keV; the variation in the intensity of emitted electrons from the surface delivers an image of surface with a lateral resolution limited by the diameter of the electron beam of about 20 Å. Because the emission intensity of secondary electrons is affected by both surface topography and electronic properties of the surface material, some of the intensity contrast in a SEM image is due to the latter effect. Although, for study of island formation the small electronic dissimilarity on the surface cannot disturb the topographical image.

The SEM studies in this work have been done *ex situ* in a S360 Leica Cambridge microscope [65].

4.2.7 Atomic force microscopy

Atomic force microscopy (AFM) is also a direct method for surface imaging [66]. It allows the force between a sample surface and a very sharp probe tip to be measured and, thus, literally, to ”feel” the surface. The tip is mounted on the end of a cantilever having a very low force constant of about 0.001–0.1 N/m, which is more than two orders of magnitude smaller than the typical force constant between two atoms. This low force constant results in a highly precise imaging method with a resolution limited by the dimension of its tip, which is in nanometers range. A sample is fixed on a piezoelectric transducer that controls scanning motion. During scanning the tip is held in contact with the sample surface. A laser beam is focused onto the end of the cantilever, and the reflection beam is detected by a photodiode (see Fig. 4.7).

High spatial resolution and the possibility of surface imaging without any preparation yield an advantageous method for structural characterization of quantum dots. Furthermore, both conducting and insulating materials can be studied with AFM. A disadvantage of AFM is the impact of tip shape on the measurements. Figure 4.8 shows two AFM images from same sample scanned

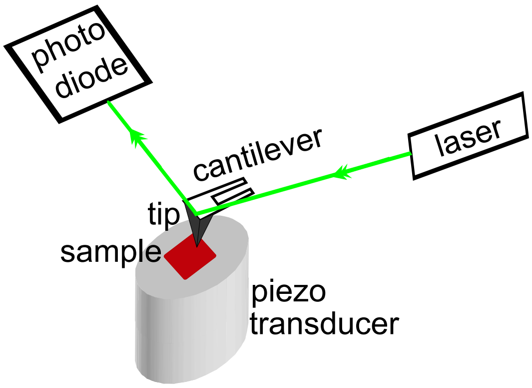

Figure 4.7: Schematic setup of AFM.

using two different tips. AFM investigations in this work have been carried out in a TopoMetrix Discover microscope under ambient conditions. The tips were made of silicon nitride and the length of cantilever was about 200 μm [67].

4.2.8 Transmission electron microscopy

The principle of transmission electron microscopy (TEM) is incidence of a focused electron beam on a sample with thickness less than 200 μm and detection of both deflected and undeflected electrons that penetrate the sample. Several magnetic lenses are used to guide the signal to a film plate and to provide

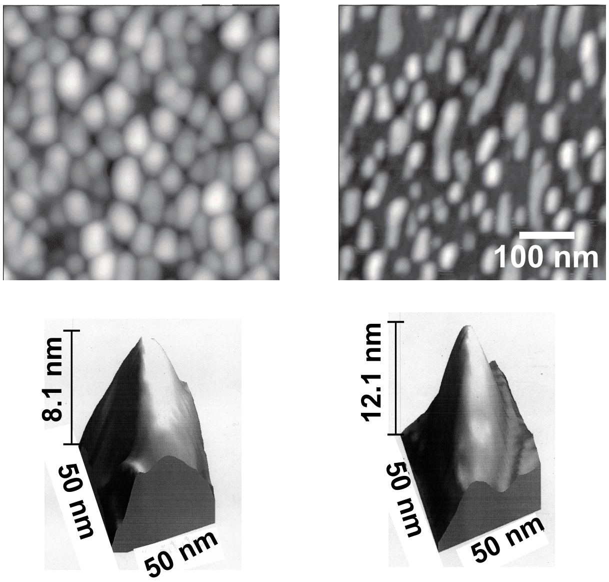

Figure 4.8: AFM images from same sample using two different tips. The corresponding tips are also shown.

the intended image. The greatest advantages of TEM are its high resolution, which is better than 2 Å, and its capacity to provide both image and diffraction information from samples.

Analogous to RHEED and X-ray pattern, the diffraction mode provides information from reciprocal space, whereas the image mode produces a real-space image of the illuminated sample area. The image contrast can be due to mass contrast (different atoms), thickness contrast (variation of thickness), diffraction contrast (beam scattering by defects), and phase contrast. There are three image modes in TEM: bright field, dark field, and high-resolution.

In practice, the particular image mode is dependent on the kind of objective diaphragm being used as a filter in the back focal plane. Bright-field image develops as transmitted electrons and all diffracted beams are filtered. Image contrast arises, when electrons in some segment of the illuminated sample area are scattered. This scattering can occur when some variation of chemical composition, or of thickness, or strain are present within sample. The degree of darkness scales with the scattering intensity; as an example, the atoms with higher atomic number appear darker. If the central beam ((000) reflection) is not included, only the diffracted beam is able to pass, and the dark-field image appears. Weak-beam dark field imaging is a powerful method for the study of dislocations that are the main origin of scattering in a crystal and produce a bright peak on a darker background [68].

High-resolution transmission electron imaging operates using a large-diameter objective that allows not only the transmitted beam, but also at least one diffracted beam to pass. This imaging method has atomic-scale resolution and is often used to determine the shape of quantum dots [69,70,71]. However, it should be noted that the interpretation of images is possible only using a multiple-beam dynamic image simulation [70].

Conventional TEM equipment and also which is used here operates with acceleration voltage about 200 keV and allows to analyze structures having a maximum thickness of about 200 nm [72]. Therefore, a highly important aspect of the TEM technique is the preparation of high-quality thin films. For plan view imaging of samples thin slices with thickness of 10–100 nm were prepared by chemical etching or ion milling. The technique for producing high-quality samples for cross-section TEM is more difficult. The microscope used is a Hitachi H-8110 [73]. For more information on TEM equipment and sample preparation refer to [74].

4.3 Optical characterization methods

Optical experiments can provide a variety of information on heterostructures. Not only the quality and level of impurity in samples are examined, but also electronic properties, quantum size effects, and recombination and relaxation dynamics of carriers quantum structures are studied using optical characterization methods. All of these techniques are based on interaction between semiconductors and electromagnetic radiation (for more information refer to [75, 76]).

For most of the optical experiments contributing to this work I have been able to benefit from equipment at Paul-Drude-Institute in Berlin [77]. The frequently applied characterization method is photoluminescence that will be discussed in the next section.

4.3.1 Continuous wave photoluminescence

Photoluminescence (PL) is radiative recombination emission that may occur when photons whose energies correspond to or exceed the gap energy (or that of intermediate states) excite valence electrons across the gap. Besides free carriers that result in a band-band luminescence peak, bound exciton recombination may produce a characteristic photoluminescence peak indicating the quality of semiconductor (high level of impurity disturbs the Coulomb interaction and, hence, the probability of exciton formation decreases). Radiative recombination may also occur between impurity states and the valence and conduction bands. Phonons can produce characteristic photoluminescence peaks. That is, photoluminescence spectra may involve a combination of band-band, excitonic, impurity, and phonon features. Therefore, detailed line-shape analysis of PL spectra is required.

Measurements for this work were carried out in our own continuous-wave photoluminescence (cw-PL) laboratory as well as in an external one located at Paul-Drude-Institute [77].

Due to the nonequilibrium nature in PL-emission process, a laser is needed as energy source for pumping electrons into the higher levels. In our own PL laboratory, photoluminescence is excited using the 514.5 nm line of a cw Ar^+ laser and the signal is detected by a photomultiplier. Samples studied at Paul-Drude-Institute are excited using the 325 nm line of a He-Cd laser (beam size is about 100×100 μm^2) and the emission is dispersed by a 1 m monochromator and detected by a charge-coupled device (CCD) camera. In both setups the measurements can be performed in the temperature range of 5–300 K, which is controlled by a continuous-flow cryostat.

Photoluminescence in magnetic field

In our own laboratory samples were excited in magnetic fields up to 7 T with a spectral resolution better than 0.1 meV (see also the description of the cw-PL laboratory at the beginning of this section). The magneto-PL at Paul-Drude-Institute is measured using the superconducting magnet system OXFORD Spectromag 1000. The temperature of samples is controlled in a continuous-flow cryostat and the excitation is provided by the 413.1 nm line of a Kr^+ laser, the magnetic-field direction being parallel to the light propagation (Faraday geometry). The magneto-PL signal is dispersed in a DILOR spectrograph XY800 and detected by a CCD camera.

4.3.2 Time-resolved photoluminescence

The first step for measuring time-resolved photoluminescence (TR-PL) is the generation of modulated optical pulses with a time constant τ_m shorter than the decay time τ that is to be measured:

$$\tau_m \leq \tau. \tag{4.7}$$

Decay times in nanosecond or picosecond range for $InP/In_xGa_{1-x}P$ quantum structures are expected. The TR-PL measurements for this time range are realized using laser pulses from a mode-locked Ti:sapphire ($\lambda = 772$ nm) pumped with a cw-Ar^+ laser. InP/GaP samples are excited, actually, using a second harmonic generator that provides a laser beam with half the wavelength (386 nm). Decay times in ns range are measured using a pulse picker, which reduces the repetition rate from the original 76 MHz to 950 kHz. Signal was detected by a Hamamatsu C5680 streak camera, which works generally in a way that photons are incident on a photocathode, and thus produce electrons that are accelerated in an electric field. A linear time-dependent voltage transforms the time delay of electrons into a spatial separation, which can be monitored on a fluorescent screen. The resulting luminescence pattern on the screen is detected by a CCD camera. Figure 4.9 shows the basic setup of TR-PL equipment [78].

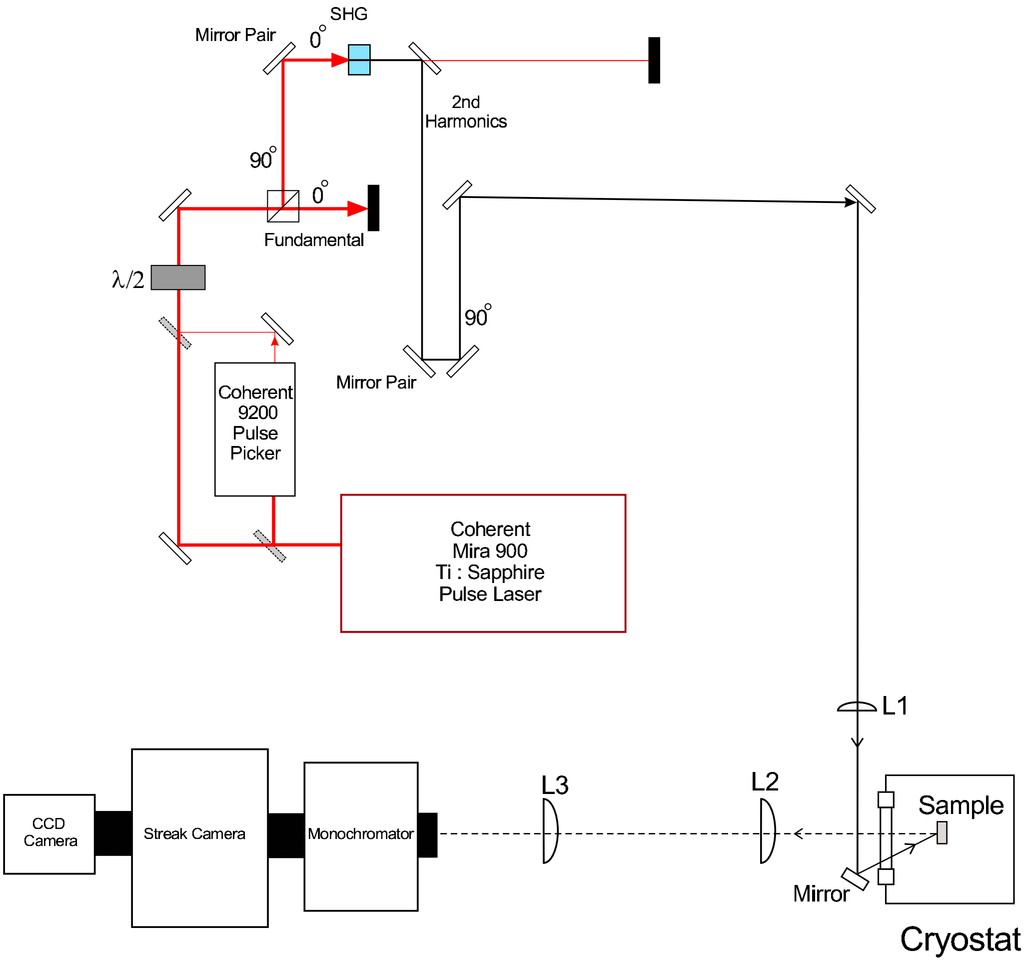

Figure 4.9: Scheme of time-resolved photoluminescence setup [78].

4.3.3 Raman scattering

Disparate absorption spectroscopy, Raman scattering, is based on inelastic interaction between light and phonon modes, resulting in a frequency shift between incident (ω_i) and scattered (ω_s) photons, which can be written according to the energy and momentum conservation rules as follows:

$$\omega_s = \omega_i \pm \Omega \tag{4.8}$$

$$\mathbf{k}_s = \mathbf{k}_i \pm \mathbf{K}. \tag{4.9}$$

Ω and $\mathbf{K}$ denote the phonon frequency and of wavevektor, respectively ($\pm\Omega$ represents the case of Stokes and anti-Stokes shift). Although Raman scattering is a weak process, lasers supply enough power for a measurable signal. The

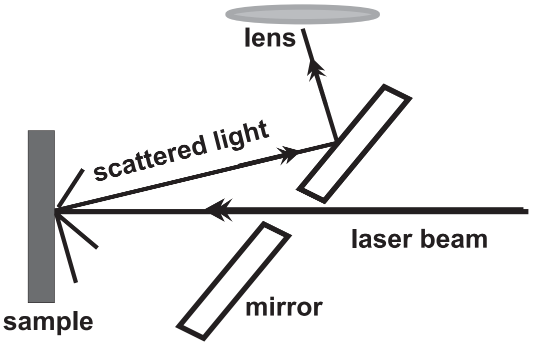

Figure 4.10: Backscattering geometry. Laser beam passes first through a hole in a mirror and then hits the sample. Scattered light from the sample is reflected by the mirror and collected and transmitted by a series of lenses to a spectrograph.

excitation source for Raman-scattering measurements for this work was a Kr^+ laser. Samples were excited with energies of 3.00 and 3.05 eV. The measurements were carried out in backscattering geometry (Fig. 4.10) with the sample temperature controlled by a continuous-flow cryostat. The scattered light is analyzed by a DILOR triple spectrograph equipped with a cooled CCD array. The polarized Raman spectra were recorded in the $z(y,y)\bar{z}$ scattering configuration, where y, z and $\bar{z}$ denote the [110], [001] and $[00\bar{1}]$ crystallographic directions of the substrate [79].

4.4 Electrical characterization methods

Besides optical experiments, electrical experiments can provide information on both bulk semiconductors and quantum heterostructures. Not only the crystallographical quality and the doping level of samples can be examined, but it is also possible to study the electronic properties of quantum structures. The applied electrical characterization method in this work is mainly Hall measurements, which will be discussed briefly in this section. For more information on electrical characterization methods refer to [80].

Hall measurement

Hall measurements allow to obtain profiles of both carrier density and mobility. The Hall effect is illustrated in Figure 4.11. A sample with lateral size d and thickness w is brought into a homogeneous magnetic field $\mathbf{B}=(B_x,0,0)$ normal

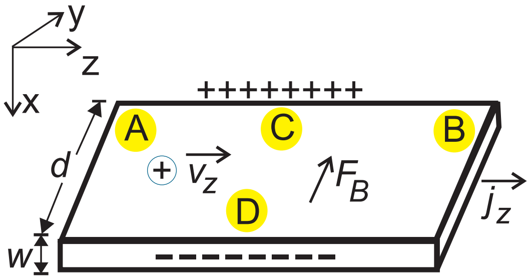

Figure 4.11: Illustration of Hall effect. + and − stand for electrons and holes, respectively. A, B, C, and D show the contacts on the sample.

to the sample surface. An applied lateral electric field E_z causes carrier (for example, holes) current with a current density j_z. Under this condition, the holes with a drift velocity v_z are pushed by a Lorentz force F_B=eB$_x v_z$ in the positive y direction. This deflection results in a electric field E_H, known as Hall field, which opposes the Lorentz force and is given by $E_H = V_H/d$ in steady state ($j_y = 0$):

$$eB_x v_z = -eE_H. \tag{4.10}$$

V_H denotes the Hall voltage and can be measured between two lateral contacts on the opposite sides, C and D in Figure 4.11. Furthermore, from the steady state condition it is clear that $E_H \propto B_x\, j_z$. Hence, the proportionality constant R_H (Hall coefficient) is defined as:

$$R_H = \frac{-E_H}{B_x j_z} = \frac{r}{ep} \tag{4.11}$$

where r is the Hall scattering factor and lies between 1 and 2. p denotes the hole density. Using all measurable parameters: Hall voltage, current, magnetic induction, and the sample thickness, the Hall coefficient can be estimated

$$R_H = \frac{-E_H}{B_x j_z} = \frac{V_H/d}{B_x I_z/wd} = \frac{V_H w}{B_x I_z} = \frac{(V_C - V_D)\,w}{B_x I_z} \tag{4.12}$$

The Hall mobility is given by

$$\mu_H = |R_H \sigma| = r\mu \tag{4.13}$$

where μ is the drift mobility, obtained as

$$\mu = \frac{\sigma}{ep} = \frac{R_H \sigma}{r} = \frac{|V_C - V_D|}{|V_A - V_B|} \cdot \frac{1}{B_x} \cdot \frac{1}{d} \cdot \frac{1}{r}. \tag{4.14}$$

Hall measurements are done in a magnetic field of 0.7 T. The temperature of samples is controlled in a continuous-flow cryostat. A KEITHLEY 220 current source provides current and the voltage is measured using the KEITHLEY 195A digital voltmeter. To switch between the contacts, the KEITHLEY 705 scanner is used.

Chapter 5

InP/(In,Ga)P system

5.1 Introduction

As we discussed in Section 3.4.1, self-organization during growth is the prevalent method applied for the formation of quantum dots. The high lattice mismatch between InP and $In_{0.48}Ga_{0.52}P$ (lattice matched to GaAs) of about 3.8% provides sufficient strain to allow the formation of QDs via the Stranski-Krastanow mechanism [81, 82, 83, 84, 85] with optical emission spanning the energy range between the InP and $In_{0.48}Ga_{0.52}P$ bandgaps.

In this chapter the growth, structural, and optical properties of InP QDs in and on $In_{0.48}Ga_{0.52}P$ will be described and discussed.

The formation of InP quantum dots on (In,Ga)P may be affected by inherent phenomena at the (In,Ga)P alloy surface such as strain inhomogeneity, alloy ordering, and indium segregation. To control the growth of QDs and to compare the dot formation process with other material systems, it is necessary to avoid such undesirable phenomena. The next section, therefore, surveys the growth and properties of bulk $In_{0.48}Ga_{0.52}P$, which is lattice matched to GaAs. Section 5.3 presents and discusses the growth and structural properties of $InP/In_{0.48}Ga_{0.52}P$ quantum dots. Optical properties of and carrier dynamics in InP QDs are discussed in Section 5.4.

5.2 Lattice-matched (In,Ga)P on GaAs

During the last two decades, the growth and application of $In_{0.48}Ga_{0.52}P$ lattice matched to GaAs have been enhanced. $In_{0.48}Ga_{0.52}P$ is an important semiconductor for optical application such as light emitting diodes operating in the visible range, as cladding material for 0.98 μm laser diodes [87, 88], as well

Material	**InP**	**GaP**	**$In_{0.48}Ga_{0.52}P$**
E_g (eV)	1.42	$2.38_{(ind)}$	1.92
a_0 (nm)	0.587	0.543	0.564
a_v	1.27	–	–
$E_{v,av}$	−7.04	−7.40	−7.23
E_c	−5.58	−5.02	−5.29
b	−2	−1.65	−1.82
D^{001}	1.127	0.906	1.012
a_c	−5.04	–	–
Δ_0	0.11	0.08	0.09
m_e	0.079	0.22	–
m_{hh}	0.65	0.79	–
m_{lh}	0.12	0.14	–

Table 5.1: Material parameters used in this work. $In_{0.48}Ga_{0.52}P$ parameters are linearly interpolated between InP and GaP values from [7, 86].

as for electronic devices such as modulation-doped field effect transistors [89]. Today, the growth of lattice-matched (In,Ga)P on GaAs is a standard procedure [90, 91, 92, 93, 94, 95].

5.2.1 Growth conditions

Samples were grown on (001)-GaAs substrates, which were etched in a solution of $10H_2SO_4 : 1H_2O_2 : 2H_2O$. After oxide desorption at a temperature of about 630°C, a 100 nm GaAs buffer was grown at 500°C at a rate between 0.9 and 1.8 μm/h, followed by $In_{0.48}Ga_{0.52}P$ grown at temperatures between 400 and 520°C.

During the growth process the RHEED patterns were monitored. The surface of $In_{0.48}Ga_{0.52}P$ shows a (2×1)-reconstruction.

Exchange and intermixing between As and P: Exchange reactions between the group-V elements during epitaxy are well known; furthermore, because AsH_3 and PH_3 are sharing the same port in our own MBE setup (see Sec. 3.2.2), an intermixing between both gases is possible. To study these effects in the (In,Ga)P/GaAs system, a series of epitaxial bulk GaAs samples was prepared in such a way that during epitaxy the growth was interrupted for 10–30 s under PH_3 flux. Figure 5.1 shows an X-ray spectrum from a 1000 nm epitaxial GaAs sample; the growth interruption was introduced after epitaxy of 100 nm GaAs and then 900 nm GaAs was grown. The pendellösung in this

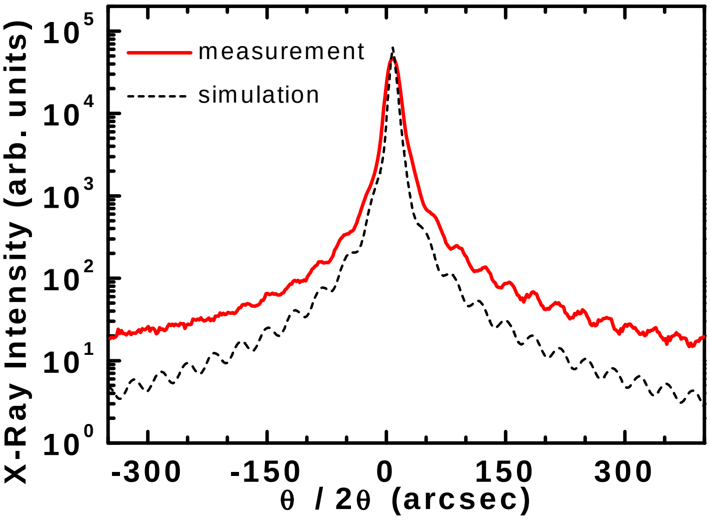

Figure 5.1: X-ray spectrum from 1 μm GaAs with 10 s growth interruption under PH_3 flux. The pendellösung is due to a very thin layer with different lattice constant from GaAs, which is explained with exchange reactions between P and As atoms in GaAs. The best fit is achieved by addition of a 3 Å $GaAs_{0.62}P_{38}$ layer.

spectrum indicates that this sample contains a very thin layer having different lattice constant from GaAs substrate. According to the simulation, the thickness of this thin layer is about 3 Å and is induced via substitution of As atoms by P atoms. The best fit is achieved for $GaAs_{0.62}P_{0.38}$. All samples grown in such way contain a very thin $GaAs_xP_{1-x}$ layer; for longer growth interruption the P composition increases, however, we did not observe any saturation of P composition in the range of 10–30 s. Our results exhibit that an intermixing between both gases and the exchange between As and P can take place during growth of (In,Ga)P/GaAs structures.

To reduce the intermixing and exchange reactions at the (In,Ga)P/GaAs heterointerface, we have introduced a growth interruption with gas change between epitaxy of GaAs and (In,Ga)P layer; here, the gas-switching plays a crucial role for growth of abrupt interfaces [96]. The applied gas-switching sequence is depicted in Figure 5.2.

5.2.2 Structural properties

The compositions and the quality of the (In,Ga)P layers were controlled by DCXD measurements. Figure 5.2.2 shows an X-ray spectrum from a sample containing a 700 nm thick (In,Ga)P layer on (001)-GaAs substrate. The es-

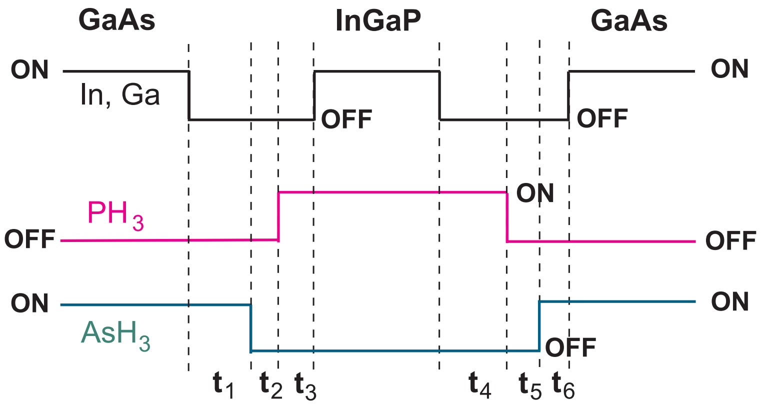

Figure 5.2: Schematic illustration of gas-switching sequence: t_1=30–120 s, t_2=8 s, t_3=3 s, t_4=15 s, t_5=5 s, t_6=3 s.

timated lattice mismatch between (In,Ga)P and GaAs is only about 100 ppm (parts per million), which is remarkably low, compared to lattice-matched systems like (Al,Ga)As/GaAs; furthermore, the sharp lines indicate the good quality of the epilayer.

5.2.3 Optical and electronic properties

Figure 5.4 shows the low-temperature PL spectra (10 K) of 1 μm, silicon doped (n=5×10^{16}) $In_{0.48}Ga_{0.52}P$ epitaxial layers. All samples were grown under same conditions; the only difference was the growth temperature, which changed from

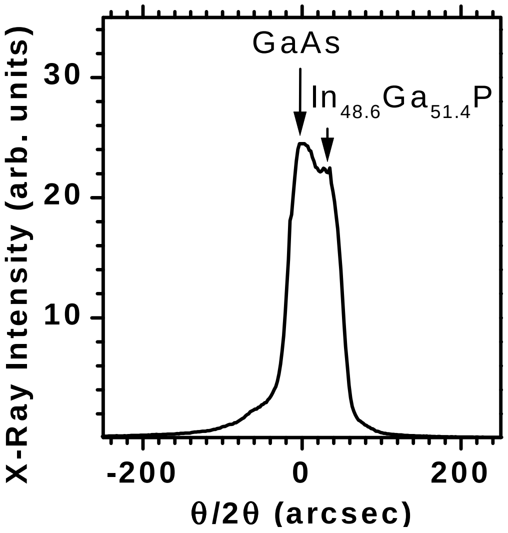

Figure 5.3: X-ray spectrum of (In,Ga)P bulk grown on (100)-GaAs. The lattice mismatch between the (In,Ga)P layer and GaAs substrate is about 100 ppm.

400°C to 495°C. Apparently, the growth temperature affects the shape and position of PL lines. The PL spectra from all samples contain two lines: one sharp exciton-like peak (full width at half maximum (FWHM) about 10–15 meV) and one broad peak (FWHM≈35 meV). The positions of PL peaks change with growth temperature: The exciton-like peak is redshifted by about 17 meV when the growth temperature goes up from 400°C to 495°C, whereas the broad PL peak at lower energy is first shifted toward higher energy (blueshift) by about 4 mV for sample B and after that this peak is redshifted about 13 meV (the error is in the range of 1 meV). Because the DCXD analysis indicates that the average composition of indium and gallium is nearly constant in all four samples (the In content is about 0.471 ± 0.002), the difference between the PL spectra cannot be due to the varying alloy composition alone; however, this can be the reason for the small blueshift of the broad PL peak.

On the other hand, the influence of growth temperature on alloy ordering and consequently on the bandgap in (In,Ga)P is well known. This will be discussed now.

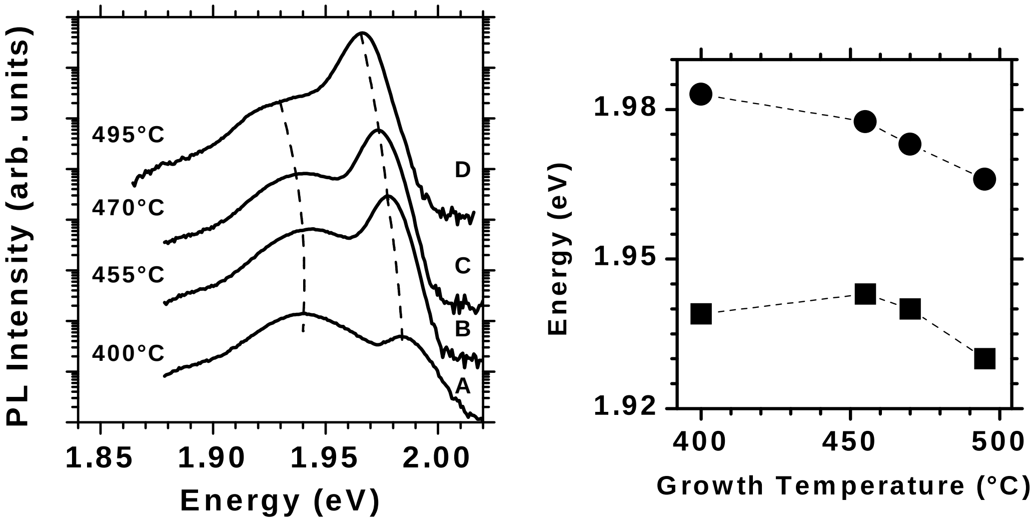

Figure 5.4: Photoluminescence spectra (10 K, 60 W/cm^2) of In$_{0.48}$Ga$_{0.52}$P bulk samples grown under same conditions with different growth temperature: (A) 400°C, (B) 455°C, (C) 470°C, and (D) 495°C; the growth temperature of indium and Ga was 778.5 and 905.8°C, respectively. The dashed lines are a guide to the eye and indicate the shift of PL maxima. PL intensity is on a logarithmic scale. Photoluminescence peak maxima as function of growth temperature obtained from the PL spectra are shown in the right graph.

Alloy ordering

The common belief is that the change in ordering, which depends on growth conditions, leads to bandgap variation and change in PL spectrum. The degree of ordering η is defined by the composition of the alternating Ga- and In-rich monolayers: Ordered (In,Ga)P consists of a sequence of layers ($Ga_{1+\eta}In_{1-\eta}P_2$) and ($Ga_{1-\eta}In_{1+\eta}P_2$). In the case of fully ordered material (CuPt ordering), η is equal unity and the elements Ga and In occupy the alternate (111) planes of group-III *sublattice*, forming a ...Ga-P-In-P-Ga-P-In-P... natural *superlattice* in the $\langle 111 \rangle$ directions [97, 98, 99].

The ordering modifies the optical, electronic, and structural properties of alloys and reduces the crystal symmetry. The influence of growth temperature on the PL spectrum was observed for the first time in $In_{0.48}Ga_{0.52}P$ samples grown using MOCVD [90, 100, 101]. According to the TEM studies by Nozaki et al., three growth temperature regimes can be recognized: In the first regime (570°C–620°C), designated "Type I", the alloy is ordered in the (100) plane (short-range ordering). The second regime ,"Type II", is at higher temperature (620°C–760°C); because of higher mobility of atoms in this regime, they can form the ordered structures both in plane and in the growth direction (long-range ordering), corresponding to the CuPt ordering. Apparently, in the third regime (higher than 770°C), designated "Type III", the high thermal energy, which results in easier migration of atoms, fully destroys the ordering and, hence, the alloy is disordered. This observation is supported by PL studies on MOCVD grown samples (see Fig. 5.5): The low-temperature PL peak shifts to lower energy when the growth temperature increases, indicating stronger ordering; the lowest energy is at about 1.85 eV and obtained for samples grown at 670°C. For higher growth temperature the PL peak blueshifts, which is attributed to the weaker ordering. The maximum value of about 1.975 eV is obtained for samples grown at 770°C, fully disordered structures (see also the discussion of influence of alloy ordering on bandgap in Sec. 4.2.1). The PL peak maximum of our samples, however, is between 1.966 and 1.983 eV, corresponding to the disordered or the short-range ordered MOCVD samples. Our results agree well with those reported by Masselink et al. [95] for $In_{0.48}Ga_{0.52}P$ samples grown via GSMBE. Apparently, at low growth temperature (lower than 470°C) the mobility of atoms is not sufficient for forming any ordered structure and we are dealing with fully disordered alloy. For higher growth temperature (470°C–500°C) the PL peak is slightly redshifted, which may attributed to partially

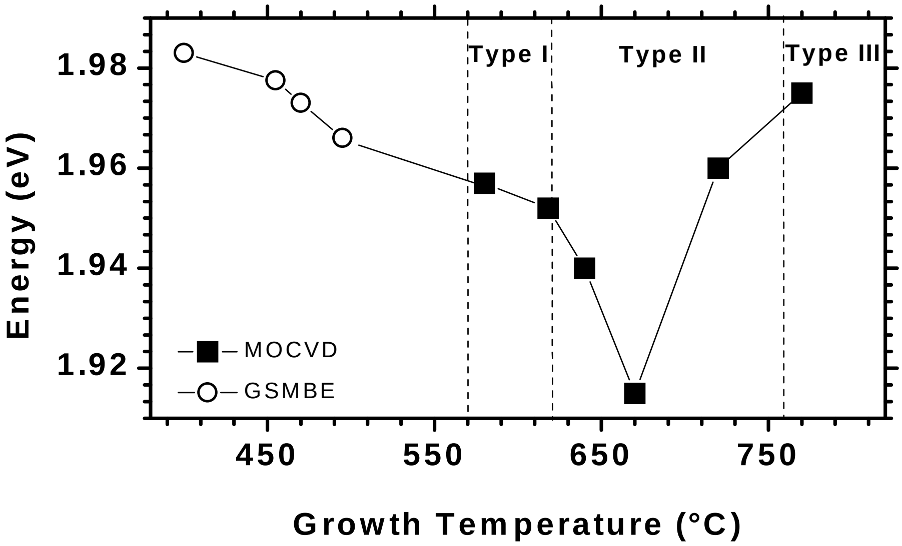

Figure 5.5: Low-temperature PL peak energy as function of growth temperature for MOCVD samples (Nozaki et al. [101]) and GSMBE samples from Fig. 5.4 (this work). The designated "Types" denote regimes of different degree of ordering [101] and are not to be confused with the band alignment type.

planar ordering. It should be noted that due to different epitaxial conditions in GSMBE and MOCVD, a comparison between growth temperatures is not straightforward.

Altogether, a change in growth temperature of $In_{0.48}Ga_{0.52}P$ could change the bandgap. Consequently, when $In_{0.48}Ga_{0.52}P$ is adjacent to another semiconductor, the band alignment on the heterointerface will be dependent on the degree of the alloy ordering. For instance, whereas the band alignment at the heterointerface of disordered $In_{0.48}Ga_{0.52}P$ to GaAs is type I [102,103], the band alignment at the heterointerface of fully ordered $In_{0.48}Ga_{0.52}P$ to GaAs, according to the experimental [104] and theoretical [105] works, is type II. It is interesting to note that even optical emission from quantum wells forming via MOCVD growth of disordered/ordered/disordered $In_{0.48}Ga_{0.52}P$ layers has been reported [106,107].

Study of optical properties is a very helpful method to determine the alloy ordering effects. It is known that the low-temperature PL spectrum of ordered (In,Ga)P is strongly excitation density dependent and shifts toward higher energy when the excitation density goes up [108,109,110]. The unusual behavior of temperature dependence PL is also known: With increasing temperature the peak maximum moves first to higher energy; afterwards, the peak maximum shifts toward lower energy (inverted S shape) [110,111,112,113].

Excitation density dependent photoluminescence

The low-temperature PL spectra (10 K) of a typical $In_{0.48}Ga_{0.52}P$ sample taken at different excitation density is shown in Figure 5.6. The high energy peak grows faster than the low energy peak when the excitation density rises from 0.06 to 60 W/cm^2; the integral intensities of both peaks depend superlinearly on excitation density with an exponent between one and two. This behavior is typical for photoluminescence processes, in which both electrons and holes are photogenerated (for example, bound and free excitons and band-to-band recombination), and in which simultaneously nonradiative processes can participate. In contrast, the integral PL line intensity depends linearly on excitation density when only holes (or electrons) are generated, for example (D^0,h) (or (A^0,e)).

As expected for band-to-band transition, for all samples (PL spectra shown in Figure 5.4) the energy position of the high energy peak is nearly constant and does not change with excitation density; we believe, therefore, that the high energy peak is due to the band-to-band transition.

On the other hand, the low energy peak (broad PL peak) is shifted by 4–7 meV toward higher energy; this blueshift is for the sample grown at 455°C

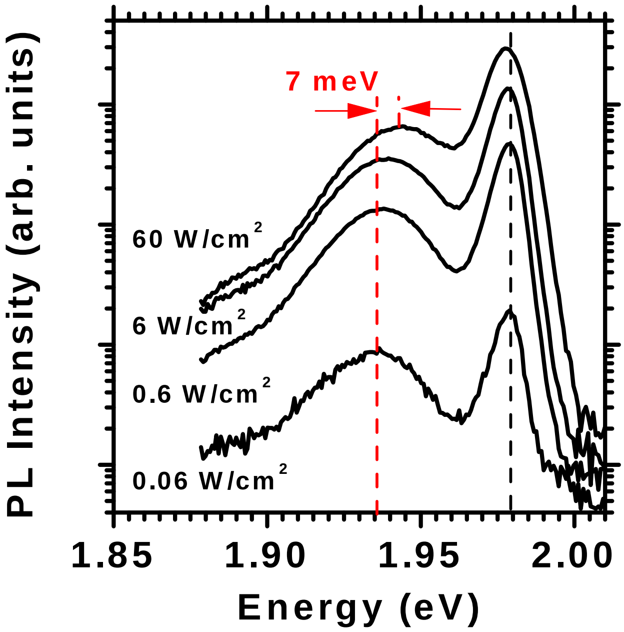

Figure 5.6: Excitation density dependence PL spectra (10 K) of $In_{0.48}Ga_{0.52}P$ bulk. The growth temperature was 455°C (sample B in Fig. 5.4). The dashed lines are a guide to the eye and indicate the shift of PL maxima.

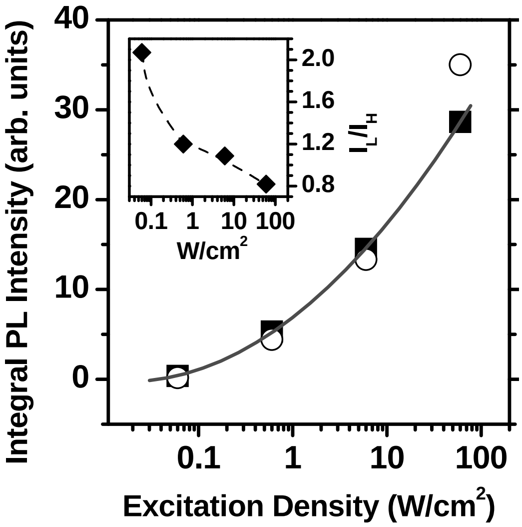

Figure 5.7: Excitation density dependence of integral intensity of high energy PL peak (I_H, open circles) and low energy PL peak (I_L, solid squares) from spectra shown in Fig. 5.6. Inset shows the ratio between the integral intensity of low energy peak and high energy peak (I_L/I_H).

(sample B in Fig. 5.4) about 7 mV and this indicates that this low energy PL peak has not an excitonic nature. But what is the origin of the low energy PL peaks? One possibility is the existence of a partially ordered $In_{0.48}Ga_{0.52}P$ alloy having a bandgap lower than disordered $In_{0.48}Ga_{0.52}P$. The PL energy position of this ordered part depends on excitation density, as reported in several works [108, 109, 110]; the blueshift is explained by assumption of an electronic density of states in ordered material, in which tails of states for electrons and holes exist below the conduction and valence band edges. In such a case, the saturation of optical transitions via band tails can causes the shift of PL peak to higher emission energy when excitation density goes up [108, 110]. However, this blueshift is nearly constant for all samples and does not exhibit growth temperature dependence. The second possibility for the origin of the low energy PL peak can be the degree of homogeneity in alloy composition. An (In,Ga)P layer with In concentration higher than 0.48% can cause a low energy PL peak. An increase in excitation density results in higher temperature of sample, which may change alloy composition and cause a blueshift; the X-ray measurements, however, do not give any evidence for such alloy inhomogeneity.

Temperature dependent photoluminescence

In contrast, the study of PL spectra at different temperatures does not indicate any alloy ordering effect (inverted S shape). The PL spectra taken at different temperatures and excited by the 686 nm line of an Ar^+ laser with a density of 60 W/cm^2 are shown in Figure 5.8. The high energy PL peak stays at approximately the same energy (1.980±0.001 eV) up to about 140 K, which is a further evidence that the origin of this peak is a band-to-band recombination.

Only a closer look at the peak maxima reveals a very small increase of the peak energy by 2 meV when the temperature is risen from 10 to about 30 K; this is generally observed in ternary alloy semiconductors; the reason here may be the small change in alloy composition due to In and Ga interdiffusion. For temperatures higher than 140 K the peak maximum shifts toward lower energy and at 300 K it is at 1.913±0.001 eV. On the other hand, the low energy peak stays in the energy position of 1.947±0.001 eV up to about 70 K, and after that

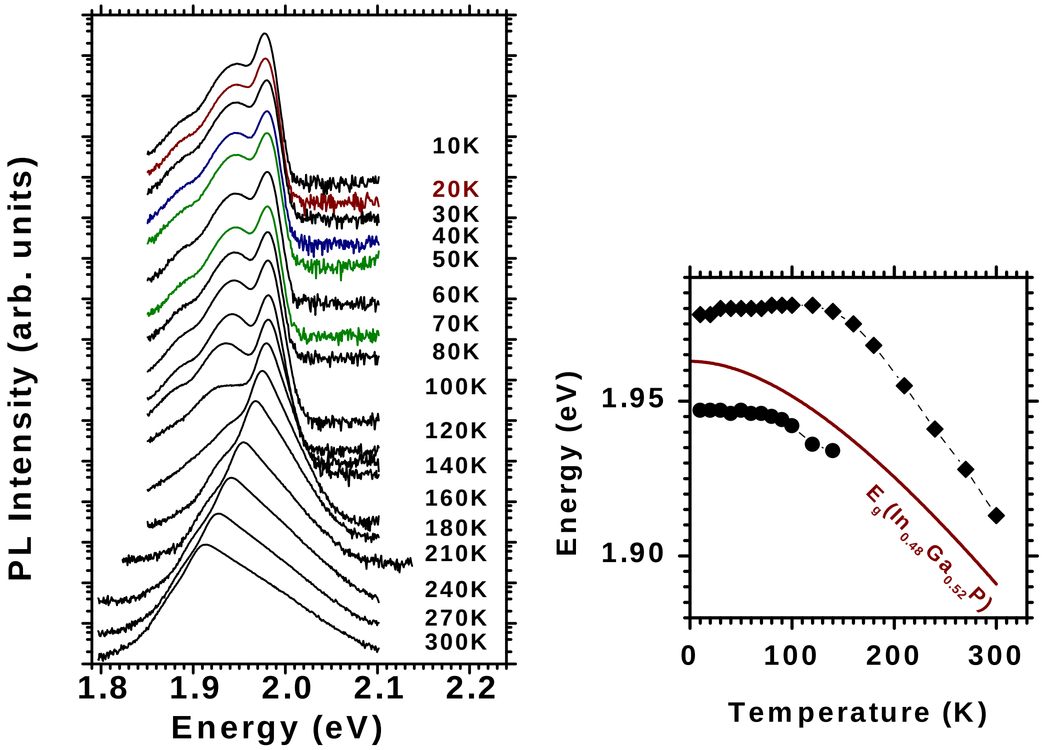

Figure 5.8: Temperature dependence PL spectra of $In_{0.48}Ga_{0.52}P$ bulk excited using Ar^+ laser (60 W/cm^2). The growth temperature was 455°C (sample B in Fig. 5.4), together with dependence of peak positions. The solid line indicates $In_{0.48}Ga_{0.52}P$ bandgap, linearly interpolated between InP and GaP (values from [86]).

shifts to lower energy by about 13 meV with increasing temperature before it becomes so small in intensity (160 K) that we are not able to determine the peak position and only a slight shoulder remains in the spectrum. Hence, we do not observe any abnormality in temperature-dependent PL spectra.

Absorption measurements

For a better study of ordering degree in our samples it is very important to have exact information on the bandgap of $In_{0.48}Ga_{0.52}P$. We have carried out, therefore, absorption measurements on the $In_{0.48}Ga_{0.52}P$ epilayers grown at different temperatures. For the measurements the substrate has been thinned to 100 μm by lapping. Then the GaAs was etched in a solution of $3H_3PO_4 : 1H_2O_2 : 15H_2O$, which is selective on GaAs with an etching rate of about 0.3 mm/h.

The absorption spectrum and the corresponding PL spectrum of a $In_{0.48}Ga_{0.52}P$ sample grown at 431°C are shown in Figure 5.9. According to this measurement, the bandgap is about 1.957 eV, which is lower than that in fully disordered $In_{0.48}Ga_{0.52}P$ alloy (1.963 eV). The shift of about 6 meV indicates ordering effects.

The degree of ordering can be estimated by [114, 115]

$$E_g(\eta) = E_g^{(\eta=0)} - \Delta E_g^{(\eta=1)} \cdot \eta^2 \tag{5.1}$$

where $\Delta E_g^{(\eta=1)}$ is bandgap reduction due to ordering and $E_g^{(\eta=0)}$ is the bandgap of a fully disordered $In_{0.48}Ga_{0.52}P$ and is 1.963 eV at 10 K. $\eta = 0$ and $\eta = 1$

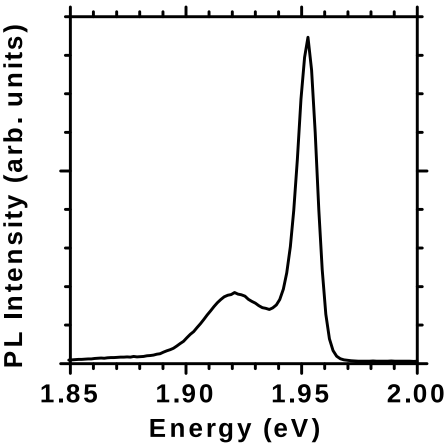

Figure 5.9: Absorption spectrum of $In_{0.48}Ga_{0.52}P$ bulk at 6 K. The growth temperature was 431°C.

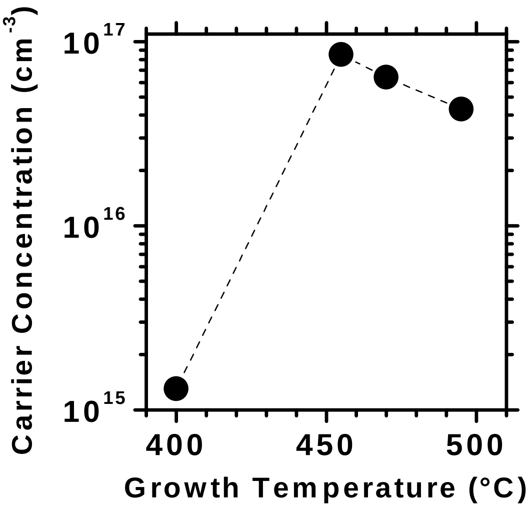

Figure 5.10: 200 K Hall concentration for $In_{0.48}Ga_{0.52}P$:Si samples as a function of growth temperature (other growth parameters were equal).

stand for a fully disordered and ordered alloy, respectively. The calculated and experimentally estimated $\Delta E_g^{(\eta=1)}$ is between 320 and 490 meV [114,115,109]. Using these values, the degree of ordering in this sample is only about 10%. The degree of ordering in the other samples grown at temperatures between 400 and 500°C was about 10%±4% and not significantly larger. Whether such low degree of ordering can affect the PL spectra will be discussed later in this section.

Hall measurements

Although intentional doping level (5×10^{16}) was the same for all samples in Figure 5.4, the growth temperature may have influenced the doping level [116], which can also affect the photoluminescence spectra.

Figure 5.10 shows the measured electron concentration as function of growth temperature. The doping level for the samples grown between 455 and 495°C increases with decreasing growth temperature from 3 up to 5×10^{16} cm^{-3}, but for the sample grown at 400°C it is significantly lower and about 2×10^{15} cm^{-3}. For samples with higher electron concentration we expect a luminescence at higher energy, therefore the difference in PL peak position of samples B, C, and D might be explained by the difference in electron concentration. But this cannot be the reason for the shift in PL spectrum of sample A toward higher energy compared to other samples.

Why do the PL spectra of bulk $In_{0.48}Ga_{0.52}P$ differ? There are several parameters that can affect the PL spectra: The homogeneity in alloy composition, the ordering, and the carrier concentration play the most important role, however, none of these parameters alone can be responsible for the differences in the PL spectra in Figure 5.4. Apparently, a random combination of these parameters is the origin and it is very difficult to isolate the contribution of each parameter.

$In_{0.48}Ga_{0.52}P$/GaAs QWs

To obtain more information on ordering effects in the samples, we have grown $In_{0.48}Ga_{0.52}P$/GaAs multi quantum wells (MQW). The conditions for growth of $In_{0.48}Ga_{0.52}P$ layers were the same as for bulk $In_{0.48}Ga_{0.52}P$ in Figure 5.4, with a growth temperature of 460°C. Figure 5.11 shows temperature and excitation-density dependent photoluminescence spectra of a sample containing 18 periods of $In_{0.48}Ga_{0.52}P$/GaAs with $In_{0.48}Ga_{0.52}P$ thickness of 10 nm and GaAs thickness of 15 nm.

In the case of disordered $In_{0.48}Ga_{0.52}P$ layers, both electrons and holes are located in GaAs and we expect for electron-hole transition an energy between the bandgap of GaAs (1.52 eV) and $In_{0.48}Ga_{0.52}P$ (1.92 eV). Surprisingly, there is no PL peak between those values and the detected PL peaks are between 1.4 and 1.5 eV. There are two possibilities to explain this: **(1)** The $In_{0.48}Ga_{0.52}P$ layers are at least partly ordered and we have a type-II system, in which the electrons are located in $In_{0.48}Ga_{0.52}P$ and the holes are located in GaAs. In such a case the energy of electron-hole transition may be lower than the energy of GaAs bandgap [104,105]. **(2)** The formation of unintentional $In_xGa_{1-x}As_yP_{1-y}$ intermediate layers at the $In_{0.48}Ga_{0.52}P$/GaAs heterointerface (see Sec. 5.2.1) may cause the PL peaks below the GaAs bandgap [117, 118, 119, 120].

In the case of a type-II system we expect a blueshift of PL peak with rising excitation density due to the effect of band-bending on the subband levels, which is observed for the ordered (In,Ga)P/GaAs system [104] and also other type-II systems such as GaSb/GaAs heterostructures [121]. In contrast to that, the PL peaks in our case are not blueshifted (see Figure 5.11); the position of the higher energy PL peak at 1.46 eV is apparently stable and independent of the excitation density. However, the lower PL peak at 1.445 eV is redshifted by about 7 meV when the excitation density becomes 580 times stronger; the reason for this redshift may be the temperature increase of sample when the excitation density becomes stronger. The fact that the PL peaks are not blueshifted indicates that the system is type I and the $In_{0.48}Ga_{0.52}P$ grown at these growth conditions is disordered, which coincides with our results from bulk material. Our assumption is that the luminescence anomaly is related to the formation of $In_xGa_{1-x}As_yP_{1-y}$ intermediate layers at the heterointerface.

To conclude, the optical studies of bulk $In_{0.48}Ga_{0.52}P$ and $In_{0.48}Ga_{0.52}P$/GaAs QWs reveal a low degree of ordering in our samples. Furthermore, the TEM and AFM studies also do not exhibit any evidence of ordered domains. Therefore, we conclude that, under the applied growth conditions, we are dealing with disordered $In_{0.48}Ga_{0.52}P$ alloy and ordering effects cannot change significantly the properties of the samples containing quantum dots, which have $In_{0.48}Ga_{0.52}P$ as matrix.

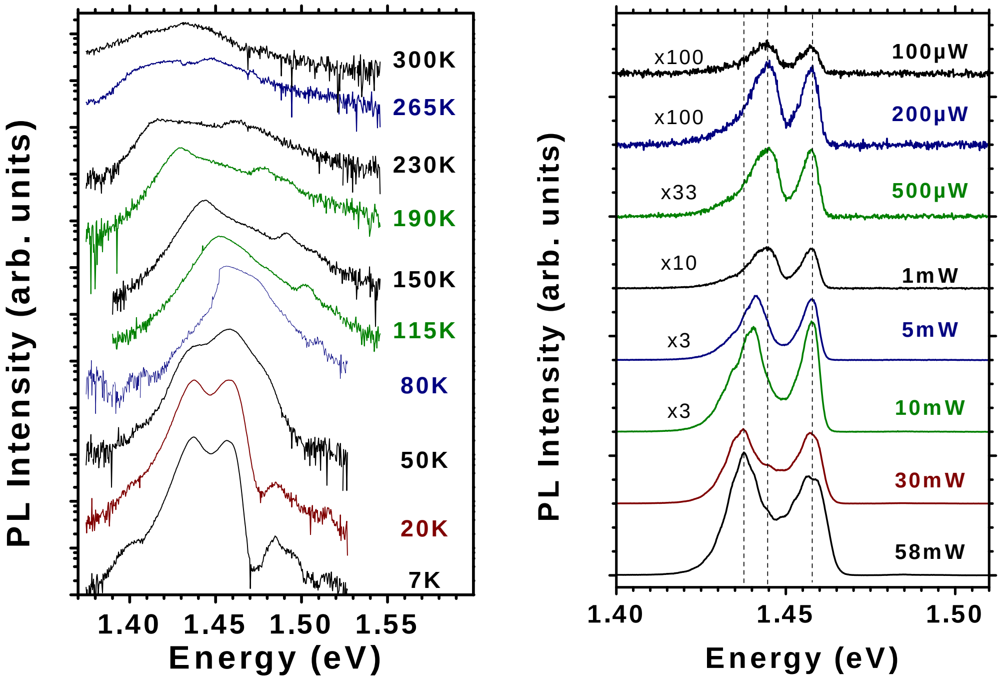

Figure 5.11: Temperature and excitation-density dependent PL spectra of a MQW $In_{0.48}Ga_{0.52}P$/GaAs sample containing 18 periods with $In_{0.48}Ga_{0.52}P$ thickness of 10 nm and GaAs thickness of 15 nm. The growth temperature during $In_{0.48}Ga_{0.52}P$ growth was 460°C. Temperature and excitation dependent PL intensities are on a logarithmic and linear scale, respectively. Dashed lines are a guide to the eye.

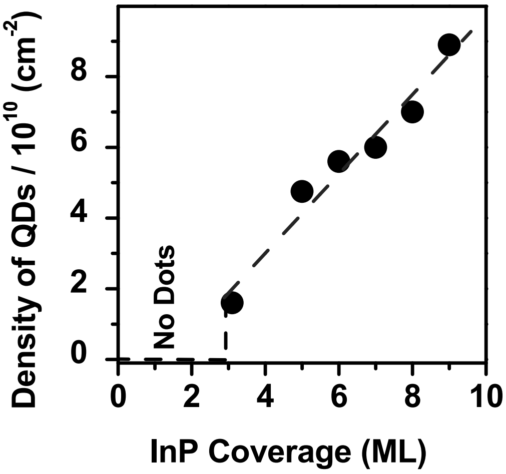

Figure 5.12: Area density of the dots per cm^2 as function of InP coverage (divided by 10^{10}). Data have been obtained from AFM and TEM studies. The dashed line is a guide to the eye and indicates the evaluation of dot formation.

5.3 InP/In$_{0.48}$Ga$_{0.52}$P quantum dots

5.3.1 Growth of InP quantum dots

The initial growth steps for samples containing quantum dots have been described in Sec. 5.2.1. After growth of 100–500 nm In$_{0.48}$Ga$_{0.52}$P buffer, the desired amount of InP was deposited; for different samples the growth temperature of In$_{0.48}$Ga$_{0.52}$P and InP was varied in the range of 415–520°C and 400–500°C, respectively. The growth of InP was followed by a growth interruption of 5–60 s. The resulting structures were capped with an In$_{0.48}$Ga$_{0.52}$P layer. Deposition rates were 0.1 μm/h for InP and 0.18 μm/h for In$_{0.48}$Ga$_{0.52}$P. The samples used for AFM and GISAXS studies were grown without cap layer. Some structures were prepared in vertically correlated multilayers. The InP thickness was varied between 1 and 9 monolayers.

At the beginning of InP growth, the RHEED pattern appears streaky and becomes gradually spotty after deposition of about 3 ML InP, indicating three-dimensional growth. This result agrees with AFM as well as SEM and TEM studies, which exhibit that QDs formation begins after the deposition of about 3 ML of InP. The area density of dots scales almost linearly with InP coverage in the range of 2–9 $\times 10^{10}$ cm^{-2} for samples with InP coverage between 3 and 9 ML (Fig. 5.12).

5.3.2 Structural properties of InP quantum dots

The quality and compositions of InP and (In,Ga)P were examined by X-ray measurements. DCXD studies reveal a good structural quality of the InP/$In_{0.48}Ga_{0.52}P$ samples.

According to the AFM studies on the uncapped QDs, the average height of the InP dots becomes about two times larger (3–5 nm) when the InP coverage goes up from 3 to 9 ML. The average base length, however, is nearly independent of the InP coverage and is about 30 ± 10 nm; here the reason may be the effect of the AFM tip, which limits the measurement resolution. On the other hand, when InP coverage increases, in addition to the small dots, a new group of dots being laterally larger than 40 nm and higher than 5 nm appears (see Fig. 5.3.2). Apparently, the growth of these large dots occurs at the expense of smaller dots. It seems that when the InP coverage increases, some of the dots grow together. This observation can be explained by Ostwald ripening: The growth of large dots reduces the overall surface of the dots, thus reducing the total surface energy (see Sec. 3.4.1). Figure 5.3.2 shows an AFM in-plane projection of a sample containing 9 ML InP. A statistical analysis of the size of about 230 dots in this sample indicates an average base length $\bar{L} = \sqrt{ab}$ of about 31 nm with a standard deviation of $\sigma_L = 4.4$ nm, a and b being the axes of the dots in [010] and [100] direction, respectively (Fig. 5.14); the relative standard deviation $\sigma_L/\bar{L}$ is about 14%. The average value of asymmetry $\alpha = (a - b) / (a + b)$ is about 0.01 (Fig. 5.14). These values indicate a narrow size distribution of the dots and a high degree of symmetry in [010] and [100] directions.

On the other hand, according to the GISAXS and X-ray diffuse scattering measurements, the strain field of the dots exhibits an anisotropy in $[1\bar{1}0]$ and [110] directions. This will be discussed in more detail in Section 7.2.3. Because of the high density of the InP/$In_{0.48}Ga_{0.52}P$ QDs, the dots are close together and the AFM tip may not be able to make perfect connection with structures

InP coverage	**base length**	**height**
5 ML	30	4
6 ML	40	4.5
7.5 ML	40	5
9 ML	35	5

Table 5.2: Average base length and height in nm of QDs as function of deposited InP coverage according to AFM studies. Samples are grown at 408° under same conditions.

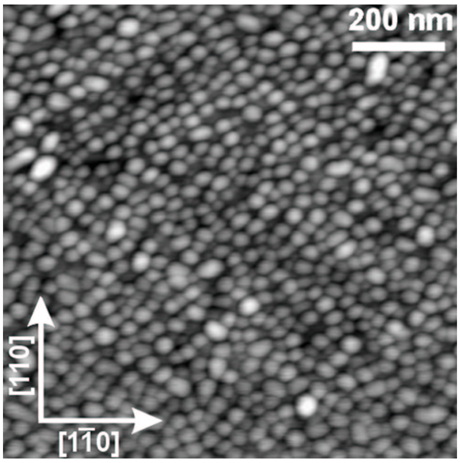

Figure 5.13: Atomic force micrograph of InP/In$_{0.48}$Ga$_{0.52}$P quantum dots with 9 ML InP coverage.

smaller than 30 nm. Hence, it is very difficult to evaluate the exact diameter and height of the dots by AFM studies. To get further information, some samples were investigated by TEM. Figure 5.15a shows a TEM bright-field cross-section micrograph of a sample with three stacked dot layers (9 ML) separated by 15 nm In$_{0.48}$Ga$_{0.52}$P. The last 9 ML of InP were grown uncapped.

As determined from the AFM data, the uncapped dots have an average height of 5 nm, an average lateral size of 30 nm, and an average center-center separation of 40 nm. The information obtained from AFM coincides very well

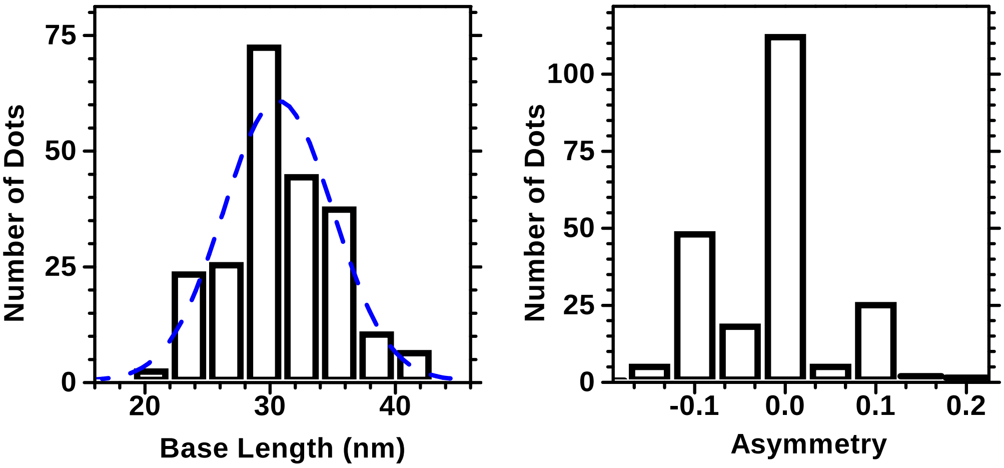

Figure 5.14: Histogram of the lateral size and the shape asymmetry of quantum dots in [010] and [100] directions from the sample containing 9 ML InP. The dashed curve is the corresponding Gaussian fit.

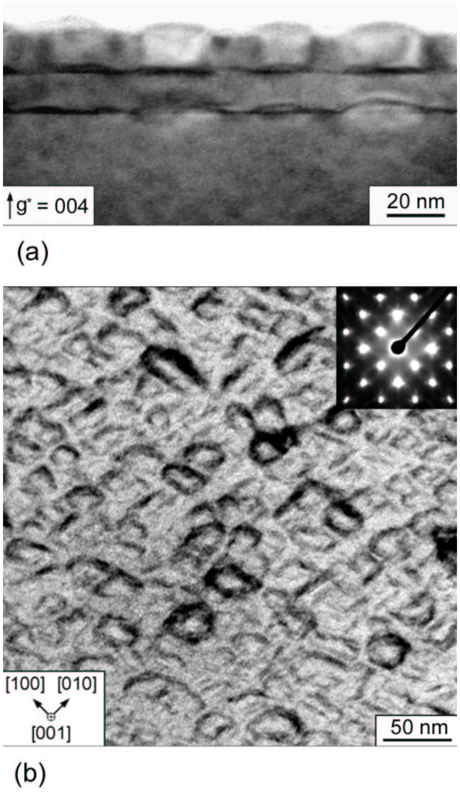

Figure 5.15: TEM bright-field images; **(a)** cross section micrograph of a sample with three stacked dot layers (9 ML) separated by 15 nm $In_{0.48}Ga_{0.52}P$; **(b)** plan-view image of a single InP QD layer (8 ML). Inset shows the diffraction pattern.

with the TEM studies of this sample (Note that this sample has the maximum InP coverage with 9 ML). Capped dots tend to become flattened, having an average height of about 4 nm. The wetting layer is somewhat inhomogeneous and between 2 and 3 ML thick. The average thickness of the wetting layer for uncapped InP is about 1 ML thinner than for the capped InP layer. The dot shape appears to be hemispherical. The stacked dots are correlated to each other vertically. TEM observations indicate that defect-free InP QDs can be grown at least up to 9 ML.

Effect of InP coverage on size of InP quantum dots

Only a close look at InP QDs using TEM studies reveals the significant effect of InP coverage on dot size. Figure 5.3.2 shows the TEM image of a sample containing 4.5 ML InP grown at 410°C. The average base length of QDs for this sample is about 14.6±0.6 nm; cross sectional TEM indicates an average height of about 2.5 nm. As expected, the size of dots increases with the InP coverage. Table 5.3 concludes these results, which is in contrast to AFM studies at different samples; AFM studies exhibit a nearly constant size of dots (30 ± 10 nm) being independent of the InP coverage (see Table 5.2). This systematic effect arises from the usage of a finite-size AFM tip and has already been discussed (see Sec. 4.2.7). Hence, we believe that the results from our AFM measurements are only reliable for dots having lateral size larger than 30 nm.

High-resolution TEM measurements (HRTEM) in the three-beam case allow to study a single quantum dot and to obtain more exact information on the dot size. However, because only a limited number of dots can be imaged in such a way, the statistics here are very poor. Furthermore, due to the difficult technique only two samples have been imaged using HRTEM. Figure 5.3.2 depicts a high-resolution TEM image of the sample containing 4 ML InP shown in Figure 5.3.2 and Figure 5.17. According to the high-resolution TEM image, the dots have an average height of about 2.5 nm and an average base length of about 12 nm, which is smaller than what we get from statistical analysis

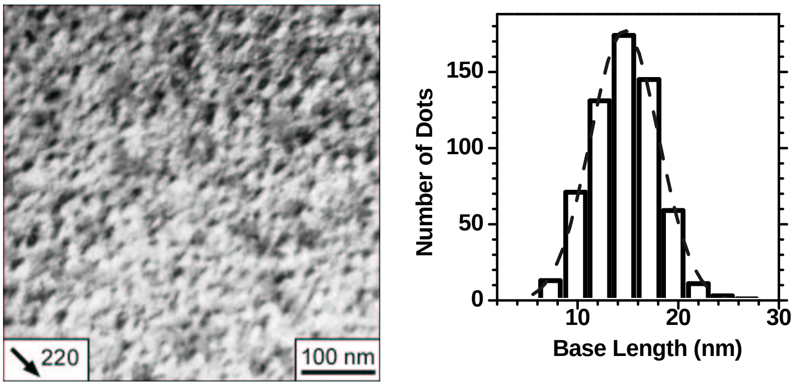

Figure 5.16: Dark-field plan-view TEM image of a QD sample containing 4.5 ML InP coverage. The histogram indicates the distribution of the lateral size of QDs.

InP coverage	**base length**	**height**
4.5 ML	15	2.5
8 ML	26	–
9 ML	30	4

Table 5.3: Average base length and height in nm of QDs as function of deposited InP coverage according to TEM studies. Samples are grown at 410° under same conditions.

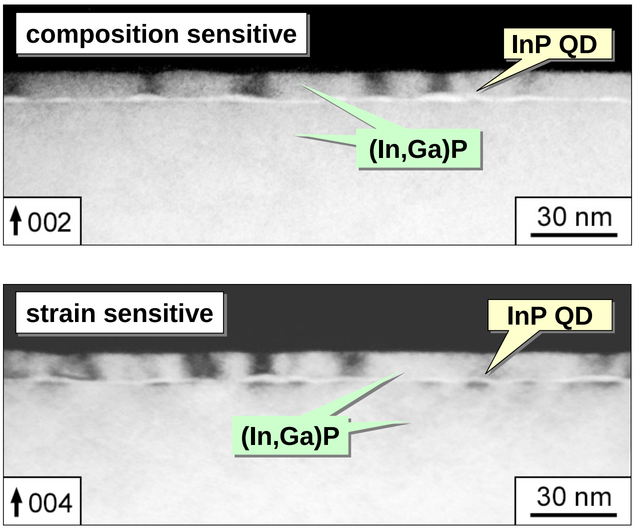

Figure 5.17: Dark-field cross-section TEM images of single-layer InP QDs measured under two different beam conditions: Composition sensitive and strain sensitive. The dark contrast above the InP dots in both images may be due to the variation of cap layer thickness resulting from sample preparation. In composition sensitive image [122] the InP layer with higher atomic number (z=64) compared to the $In_{0.48}Ga_{0.52}P$ ($z \approx 55$) appears with the lowest contrast. Thus, information on the size of dots can be obtained. The strain sensitive image provides information about the strain distribution in the sample, which can be seen also by the dark contrast in $In_{0.48}Ga_{0.52}P$ layer under the InP QDs, which is also strained and because the strain field of the QDs may extend several tens of Ångstrom, the size of the dots may be overestimated in this image.

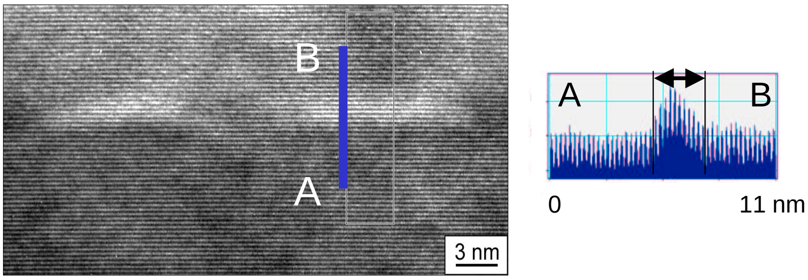

Figure 5.18: High-resolution TEM image of two InP QDs (bright) embedded in (In,Ga)P matrix (dark). The small plot on the right side indicates the line scan of brightness value from A to B in TEM image; the width of signal gives the height of dot (arrow).

of 580 dots in this sample (see Fig. 5.3.2). This may be due to the higher resolution or the poor statistics.

Effect of growth temperature on InP quantum dots

According to AFM studies on the samples grown at different temperatures, the dot density increases for samples with lower growth temperature; at the same time, the base length of dots becomes smaller. Figure 5.3.2 shows AFM micrographs of two samples (500×500 nm^2) having the same InP coverage of about 5 ML but grown at 410°C and 500°C, respectively. Keeping growth temperature low enough, we are able to suppress the dot formation; for a sample grown at 380°C the AFM image indicates only a surface roughness in of about several nanometers, indicating start of dot formation, but it is difficult to make statements about density and dot size. These results are concluded in Table 5.4 and are in agreement to general observation [45, 46, 47, 44, 43] that is already discussed in Section 3.4.1.

growth temperature	**area density**	**base length**
380°C	see text	see text
410°C	4.8×10^{10}	30
500°C	3.7×10^{10}	50

Table 5.4: Area density in cm^{-2} and average base length in nm of InP QDs grown at different temperatures as obtained from AFM studies. InP coverage is about 5 ML for all samples. The base length for the sample grown at 410°C may be smaller, but this cannot be resolved due to the limitation of AFM.

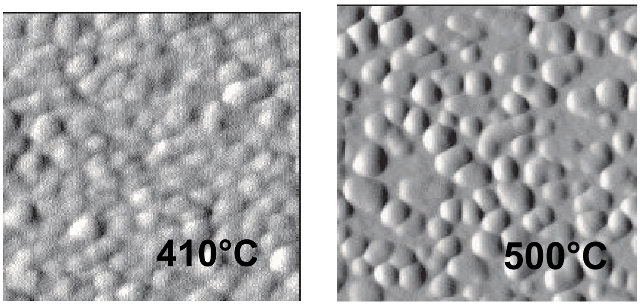

Figure 5.19: AFM micrographs of two samples having the same InP coverage of about 5 ML but grown at 410°C and 500°C. Size of images are 500×500 nm^2.

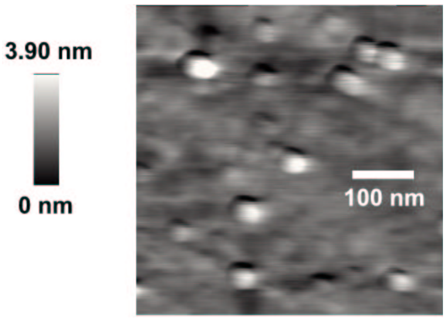

Figure 5.20: AFM micrograph of a sample containing 2 ML InP and 1 ML inserted GaP interface layer between $In_{0.48}Ga_{0.52}P$ and InP. Growth temperature for InP was 470°C.

Effect of a thin GaP interface layer on InP quantum dots

GaP has a smaller lattice constant than $In_{0.48}Ga_{0.52}P$ and, hence, compared to an InP/ $In_{0.48}Ga_{0.52}P$ interface, the InP/GaP interface is higher strained (lattice mismatch of about 7.7%). Consequently, the growth of a thin layer of GaP between $In_{0.48}Ga_{0.52}P$ and InP layers affects the formation of InP QDs. Our observations coincide with the common belief that a higher lattice mismatch favors the Stranski-Krastanow QD formation (see Sec. 3.4.1). Figure 5.3.2 shows an AFM image of a sample containing 2 ML InP grown on a GaP interface monolayer; here the area density of QDs is about 10^6 per cm^2 and the dots have a maximum base length of 35 nm. (Note that AFM images cannot give exact information on the dots smaller than 30 nm.) On the other hand, for samples grown in the same way but without GaP interface layer we do not observe any dot formation (see the beginning of this section).

Furthermore, some groups have reported an improvement of size homogeneity of MOCVD InP QDs on and in $In_{0.48}Ga_{0.52}P$ via growth of an inserted GaP layer [123, 124, 125].

Geometry of InP quantum dots

AFM in-plane projection of the QDs reveals a hemispherical shape (Fig. 5.3.2). On the other hand, on-zone bright field images in plan-view TEM show for most of the dots a rectangular base, but with rounded corners, and the elongated axis along $\langle 100 \rangle$ directions (Fig. 5.15b). However, both methods cannot provide exact information on shape of dots: AFM is not able to resolve the detailed shape of QDs and TEM performed under the dynamical two-beam condition images both the strain field within the structure and in the surrounding matrix. It is interesting to note that Liao et al. have demonstrated by multiple-beam dynamical image simulation that even a spherical QD can produce square-shape image in plan-view TEM [70]; the reason is here that the symmetry of such image is determined primarily by the underlying lattice rather than by the overall shape of the QDs [70]. Hence, the interpretation of plan view TEM images is not straightforward and needs multiple-beam dynamical image simulations.

The high-resolution TEM image indicates a lens-like (or truncated pyramidal with shallow faces) cross-sectional geometry for dots, which have an average base length of about 12 nm and average height of about 2.5 nm (see Fig. 5.3.2). In contrast, Georgsson et al. have reported pyramidal geometry for MOCVD QDs for InP coverage upon 4 ML; the base length is found to be about 60 nm [126,123]. On the other hand, for SSMBE InP QDs also a lens-like cross sectional geometry has been reported; however, the base length of those dots is about 30 nm and larger than the base length of our dots [127,128].

Because the geometry of dots influences the optical properties and, together with orientation and size distribution of QDs, determines the ordering of dots, which is very important for application devices based on QDs, this ordering will be discussed in more detail in a separate chapter (see Chapter 7).

5.4 Optical properties of InP quantum dots

5.4.1 Photoluminescence from InP quantum dots

Figure 5.21 shows PL spectra of InP/$In_{0.48}Ga_{0.52}P$ structures on GaAs containing InP coverage of 2.5, 4, 6, and 8.5 ML plus 10 nm $In_{0.48}Ga_{0.52}P$ cap layer. All samples were grown under same conditions with an InP growth temperature of 410°C. Apparently, with increasing InP coverage the PL peak maximum shifts towards lower energy and the formation of the InP dots results in a modification of the PL spectra: The PL spectra of QW samples (containing InP coverage of less than 3 ML) exhibit a broadening at lower energy side (see PL of 2.5 ML sample in Fig. 5.21) and to fit these spectra, we must take the thermic population of subbands into consideration. The InP layers in the QW samples are two-dimensional because the InP coverage is considerably lower than the critical thickness for island formation (see Sec. 5.3.1). On the other hand, the

PL spectra of QD samples indicate a simple Gaussian shape as predicted by Wu et al. [129] having a PL linewidth determined by the size distribution in a QD ensemble. Figure 5.22 depicts the low-temperature PL spectrum of a QD sample (InP coverage is 5 ML) together with corresponding Gaussian fit.

FWHM of PL lines of the QD samples is 70 ± 10 meV and independent of the InP coverage. This result is consistent with the relative standard deviation for dot size distribution of about $\sigma_L/\bar{L}$=14% from structural analysis depicted in Figure 5.14, which predicts a large linewidth for PL of QDs. Although the emission line for an individual dot is ultranarrow with a width due to the limitation of resolution of experimental setup [130], the emission line of a QD ensemble has a Gaussian form resulting mainly from the distribution of dot volumes that leads to a variation in the energy levels of the single dots. We attribute the PL line in QDs samples to radiative recombination of ground state heavy-holes and electrons in the dots. Further evidence that the PL line originates from the QDs is the lack of magnetic-field dependent splitting up to 14 T (see Sec. 5.4.2).

One interesting result from PL measurements on the InP/$In_{0.48}Ga_{0.52}P$ QD samples is that we do not detect any PL from the two-dimensional wetting layer. Here, the reason may be the high coverage density of QDs between 30% and 90% in our samples; apparently the dots capture most of the excited electrons and

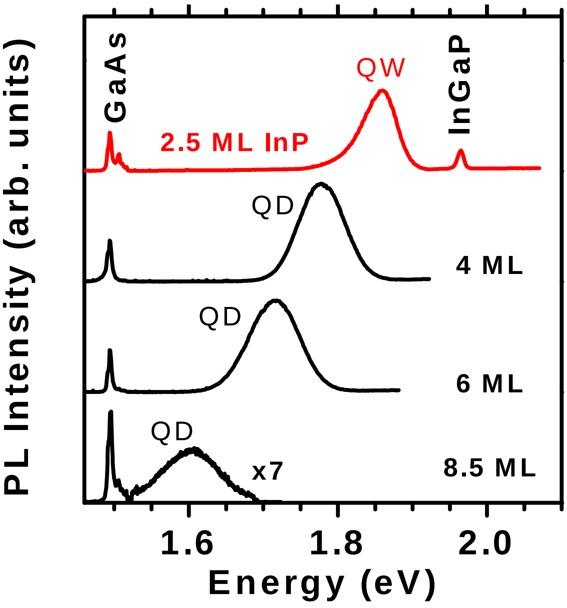

Figure 5.21: PL spectra of samples with different InP coverage measured at 6 K, excited by the 514.5 nm line of an Ar^+ laser with an excitation density of 5 W/cm^2.

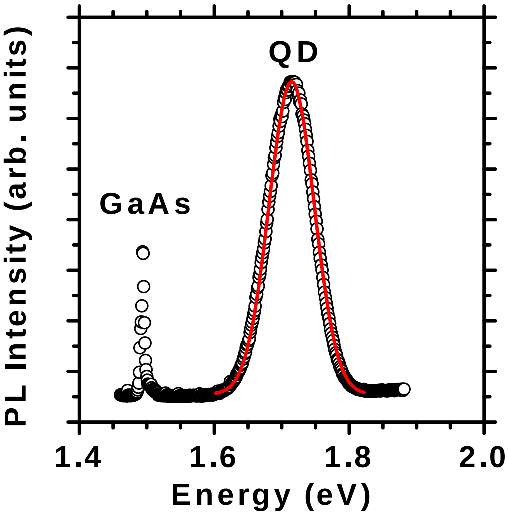

Figure 5.22: Low-temperature PL spectrum of sample containing 5 ML InP coverage (open circles) and the corresponding Gaussian fit (solid line). Fit parameters: E_{max}=1.7147 eV and FWHM=0.0670 eV. The χ^2-error is only 10^{-5}.

are the attractive channel for electron and hole recombination. It is interesting to note that only InP/$In_{0.48}Ga_{0.52}P$ QD samples grown by MOCVD have so far shown very weak luminescence from wetting layer [82, 131].

Band alignment of InP quantum dots

For the understanding of electronic and optical properties of InP QDs a band alignment modeling is required. To obtain a realistic approximation for the

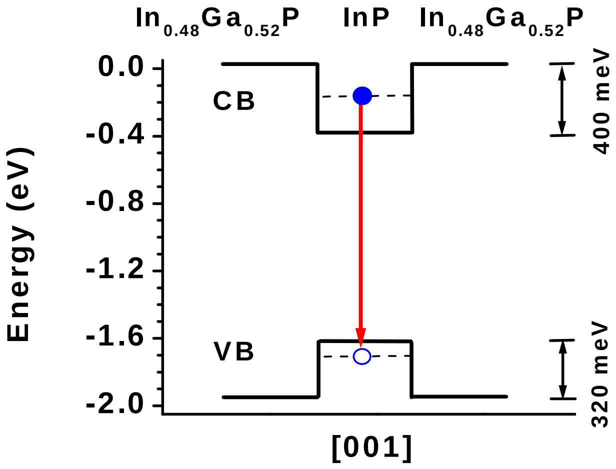

Figure 5.23: Band alignment scheme for a pseudomorphic InP/$In_{0.48}Ga_{0.52}P$ quantum slice according to Ref. [7].

band alignment, we take strain effects into account by following the procedure given in the model-solid theory by Van de Walle [7] (see Sec. 2.5). Because the lateral dimensions for the QDs are much larger than their vertical dimensions, we neglect the lateral confinement effects and model the QD as quantum slice (finite in-plane size quantum well) embedded in $In_{0.48}Ga_{0.52}P$ matrix with infinite thickness. The modeled quantum slice and average QD have same volume and base size but do not need to have same shape; the most important influence on electronic properties has the volume [40,132]. The strain distribution inside the QDs and surrounding matrix has a dominant influence on the electronic structure (and actually, depends mainly on the dot shape). To simplify, however, we will neglect the inhomogeneity of the strain distribution in the QDs and apply a homogeneous strain distribution instead. Figure 5.23 shows the calculated band alignment.

Effect of InP coverage on photoluminescence

The dependence of PL peak energy on InP coverage is depicted in Figure 5.4.1 (solid circles). Using multivalley effective-mass approximation, the localization energies for both electrons and heavy holes are calculated for the band alignment shown in Figure 5.23 as functions of InP quantum slice thickness; the solid line

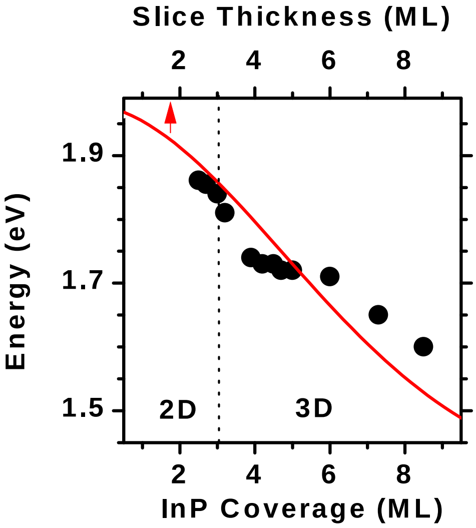

Figure 5.24: Dependence of PL peak energy on InP coverage (solid circles). The solid line indicates the calculated electron heavy-hole transition energy for $InP/In_{0.48}Ga_{0.52}P$ quantum slice as function of its thickness. Note that only for QW samples the thickness of slice is the same as InP coverage. For QD samples it is equal to the effective height of dots.

in Figure 5.4.1 indicates the calculated electron heavy-hole transition energy.

The PL peak energy dependence may be divided into three zones representing certain ranges of InP coverage:

First zone is up to about 3 ML InP coverage: It seems that when InP coverage increases, the PL maxima decrease in energy in accordance with calculations performed for the quantum slice (see Fig. 5.4.1) and the deposited InP is a two-dimensional layer; this agrees very well with our results from structural analysis indicating two-dimensional morphology for this InP coverage range where the thickness of slice is the same as InP coverage.

Second zone is between 3 and 6 ML InP coverage: The PL maxima here do not follow our calculation and are nearly independent of InP coverage (1.72±0.02 eV). This observation supports again our results from structural analysis, that we are not dealing with two-dimensional InP any more and the samples contain QDs, which we treat as quantum slice having an effective thickness given by $\vartheta = \bar{V}_{QD}/\bar{L}^2$, where $\bar{V}_{QD}$ and $\bar{L}$ are the average volume and base length of the QDs. Note that the effective thickness differs from InP coverage. According to the high-resolution TEM results for a sample containing 4.2 ML InP coverage, for instance, the average height, base and top length of dots are about 2, 12, and 8 nm, respectively (see Fig. 5.3.2); assuming a truncated pyramidal shape for dots, we get a thickness of about 1.75 nm (≈6 ML) for the equivalent quantum slice. For this quantum slice the calculated electron heavy-hole transition is about 1.67 eV. However, the detected PL energy is about 50 meV higher, but this result is in good agreement with our simple model considering that we applied a homogeneous strain distribution in the dots. Furthermore, we modeled the dots as very simple slices, thereby neglecting the known impact of dot geometry on electronic structure and consequently on the optical transitions. (There are several works about the influence of dot geometry on optical and electronic properties; for example see References [133, 134].)

Third zone is above 6 ML InP coverage: The PL maximum decreases as in the first zone when the InP coverage becomes larger. It is a matter of fact that the samples here contain quantum dots and the thickness of slice is not the same as InP coverage. However, it seems that the PL peak energy again follows in trend the calculation. But that is no indication that the InP in these samples have a two-dimensional morphology. The reason for the redshift of the PL peak may be the rapid rise of the volume of dots (see Table 5.2). The PL energies for samples containing InP coverage between 7 and 9 ML coincide with electron-hole transition energies of quantum slices having a thickness between 5 and 7 ML. Using the known size for dots in the 9 ML sample (base and top length about 30 and 15 nm and height about 4 nm) we obtain a slice thickness of about 7 ML. The transition energy for that slice (calculated curve in Fig. 5.4.1) is about 1.6 eV, which agrees well with the detected PL energy for 9 ML sample.

The fact that PL maxima in the second zone are nearly independent of the InP coverage may be explained as follows: PL energy of QD samples is mainly determined by two conflicting effects. One is the transition to 3D growth connected with QD formation, which results in higher confinement and, consequently, in higher PL energies. Second, due to strain and increasing thickness (volume), the confinement decreases. Once the system has settled down, i.e., for InP coverage above 6 ML (third zone), only the second effect contributes and the PL maxima again show a decreasing behavior with rising coverage.

A closer look in the second zone reveals a slight decrease of PL peak energy of about 20 meV, which might be due to increase of dot volume.

It should be emphasized that this very simple model cannot provide a quantitative picture of the energy levels and optical transition in quantum dots and it is just an approximation to get quickly and without complicated calculation (a pen and a piece of paper are enough) some value for the PL energy.

Note that for the calculation of electron-hole transition we do not take into account the lateral coupling between quantum dots, which affects of course the PL peak energy, especially in our samples where the distance between dots is not larger than their average base length. The lateral coupling results like vertical coupling in a PL peak shift towards lower energy. Generally, the lateral coupling amplitude between QDs may be estimated from the wave function decay in a finite barrier, which is given by the expression

$$\exp(-d\sqrt{2m_{eff}\Delta E}\Big/\hbar) \tag{5.2}$$

where d denotes the barrier thickness and is the border-to-border distance between two coupled dots, m_{eff} is the effective mass, and ΔE is the energy difference between the ground states in the dots and the wetting layer [135]. Since we observed no luminescence from wetting layer, we will use the PL energy of 2.5 ML thick QW (1.86 eV) to estimate the energy difference; the thickness of 2.5 ML for the wetting layer is known from cross-sectional TEM studies in Section 5.3. For samples containing 4.5 ML InP coverage with an approximated border-border distance of 12 nm and ground state energy of about 1.72 eV

(ΔE=140 meV), using the effective mass of InP ($0.08m_e$), we obtain a lateral conduction band coupling amplitude of about 0.15%, which is not large but is enough to redshift the calculated PL peak.

Excitation density dependent photoluminescence

Low-temperature PL spectra of a QD sample containing 4 ML InP coverage at different excitation densities are shown in Figure 5.25; the excitation source was the 514.5 nm line of an Ar^+ laser and the measurements were carried out at 10 K. As expected, the PL peak position does not change significantly for excitation power increase by factor ten and is blueshifted only about 5 meV (from 1.745 eV to 1.750 eV); the width of PL line is about 72±1 meV and almost constant. Furthermore, we do not observe any saturation of QD PL intensity within the measured range (see Fig. 5.25); such saturation is often associated with defects or impurities.

Temperature dependent photoluminescence

Figure 5.26 shows the temperature evolution of the PL from a QD sample containing 6 ML InP coverage. The excitation density was 65 W/cm^2. The results from these measurements may be classified into two temperature regimes: In the first regime between 5–100 K the maximum of PL peak is at about 1.71 eV and nearly constant, whereas in the second regime between 100–200 K the PL maximum shifts towards lower energy by 40 meV (see Fig. 5.27). This behavior is due to the temperature dependence of the bandgap and typical for III-V

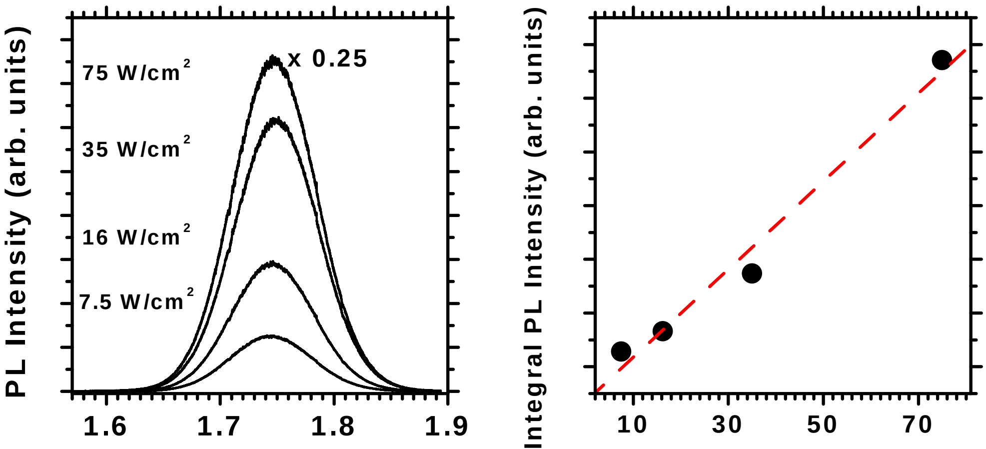

Figure 5.25: Low-temperature PL spectra (10 K) and dependence of integral PL intensity on excitation density. The dashed line indicates the linear fit.

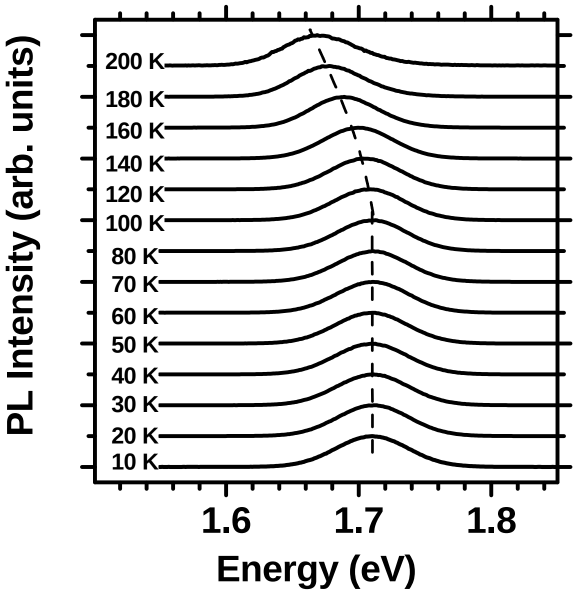

Figure 5.26: Temperature-dependent PL spectra of a sample containing InP/$In_{0.48}Ga_{0.52}P$ QDs resulting from 6 ML InP coverage (65 W/cm^2). The dashed line shows the peak maximum shift.

semiconductors and is given by Varshni equation [136]

$$E_g(T) = E_g(0) - \frac{\alpha T^2}{T + \beta} \tag{5.3}$$

where $E_g(0)$ is the bandgap at 0 K, and α and β (Debye temperature) are two material-dependent parameters. For InP bulk $\alpha = 4.9 \times 10^{-4}$ eV/K and β=327 K [137].

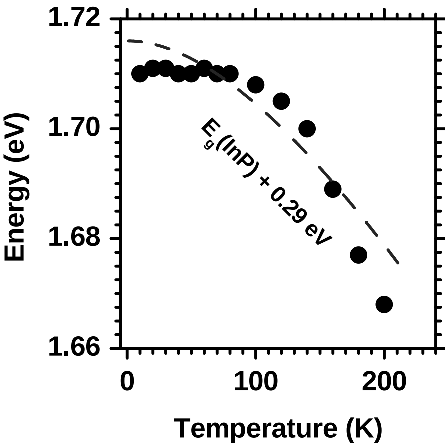

Figure 5.27: Temperature-dependent peak maximum obtained from spectra shown in Fig. 5.26. The dashed line indicates the temperature-dependent InP bandgap, shifted in energy scale.

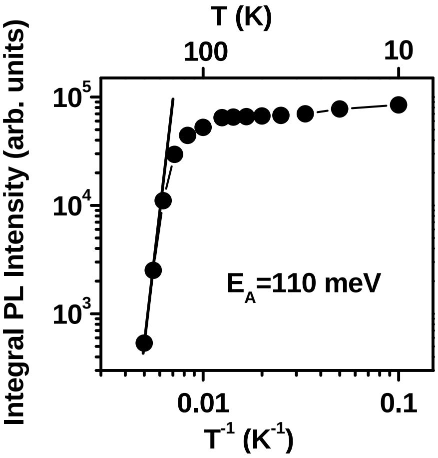

Figure 5.28: The integrated PL intensity as function of temperature (Arrhenius plot). The activation energy is derived from the slope of the solid line.

The behavior of integrated PL intensity as a function of inverse temperature may provide information about the carrier activation energy, which can be estimated by the following equation [138,139,140], derived from the Boltzmann distribution:

$$I(T) = \frac{I_0}{1 + \sum_{i=1}^{n} c_i \exp(-E_A^i/k_B T)} \tag{5.4}$$

$I(T)$ is the integrated PL intensity at temperature T, c_i is a temperature-independent constant, E_A^i the activation energy for carriers and n is the number of energy level. According to this simple model, the slope of the Arrhenius plot depicted in Figure 5.28 gives the activation energy of localized heavy holes in dot of about 110 meV, which is very helpful for understanding of dynamics of carrier recombination in InP QDs and this will be discussed in Section 5.4.3.

5.4.2 Optical polarization anisotropy

The photoluminescence of several QD heterostructures often shows polarization anisotropy due to the asymmetric shape of dots [55,141,142,143]. In order to study the effect of QD geometry on the optical matrix element and, thus, on the PL spectrum on InP/$In_{0.48}Ga_{0.52}P$ QDs, we investigated the linear polarization of the emitted PL light, which polarized along [110] and [$1\bar{1}0$] directions. The results will be demonstrated and discussed in this section.

Zero magnetic field

Figure 5.29 shows the low-temperature photoluminescence spectra of a sample containing 5 ML InP polarized along $[1\bar{1}0]$ and [110] directions. The spectra reveal a remarkable polarization anisotropy ρ of about 26%. The polarization anisotropy is defined as

$$\rho = \frac{I_{[1\bar{1}0]} - I_{[110]}}{I_{[1\bar{1}0]} + I_{[110]}} \tag{5.5}$$

where $I_{[1\bar{1}0]}$ and $I_{[110]}$ denote the integral PL intensity along the $[1\bar{1}0]$ and [110] directions. The integral PL intensity is proportional to the optical transition matrix element between valence band and conduction band

$$I_{[110]} \propto \left| < \psi_v | \mathbf{P}_{[110]} | \psi_c > \right|^2 \tag{5.6}$$

where ψ_v and ψ_c denote the valence band and conduction band state, respectively and $\mathbf{P}$ is the polarization vector.

No PL polarization anisotropy was observed between [100] and [010] directions and also the PL polarization anisotropy of the $In_{0.48}Ga_{0.52}P$ buffer and GaAs substrate vanished.

Interpretation of polarization anisotropy requires detailed theoretical investigation (see also the discussion of optical anisotropy in Sec. 6.3.3). Yang et al. calculated the electronic structures of [136]-faceted QDs using the atomistic valence force-field (VFF) model (for calculation of strain distribution) and eight-band $\mathbf{k}\cdot\mathbf{p}$ theory. They showed that the optical anisotropy is strongly dependent on the shape of the dots and that the PL spectra from QDs must be polarized along the longest axis of the QDs [144]. However, Wang et al. calculated the electronic structures of [110]-faceted, square-based pyramidal QDs, using a pseudopotential approach including spin-orbit-coupling [145]. They found that due to the strong coupling between hole states, the lowest interband transition has very different intensities along the two in-plane substrate directions $[1\bar{1}0]$ and [110]. On the other hand, in several works [55,141,142,143] the PL polarization anisotropy of elongated QDs along their longest axes have been reported.

To summarize above results, the optical polarization anisotropy of QDs can be caused by mixing of heavy-hole and light-hole states [146] that may be induced by asymmetric lateral confinement and anisotropic lateral strain [141]. The asymmetric lateral confinement due to an asymmetric dot shape may result in stronger lateral polarization along the direction the QD is elongated

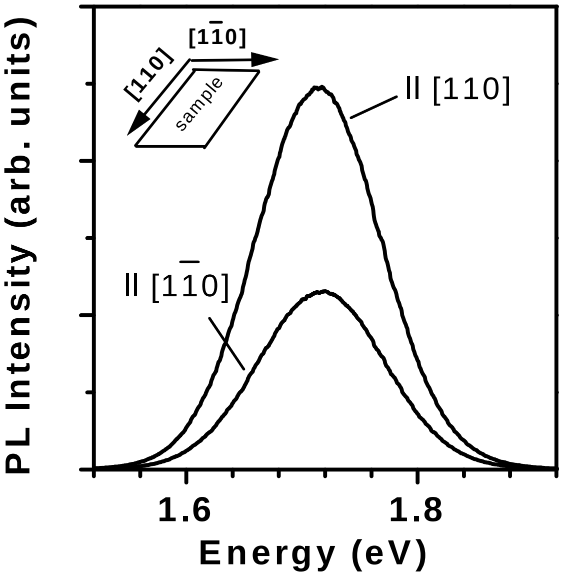

Figure 5.29: Low-temperature PL spectra (10 K) of a single layer of buried InP/$In_{0.48}Ga_{0.52}P$ QDs polarized along [1$\bar{1}$0] and [110]. The orientation of the sample is sketched in the upper-left edge.

in [144]. Additionally, the level crossing between hole states may result in optical anisotropy [147] that will be discussed in more detail in Section 6.3.2.

On the other hand, the structural properties of the $In_{0.48}Ga_{0.52}P$ matrix may also cause anisotropy in the optical transition of InP QDs. Wei et al. have demonstrated that (In,Ga)P alloy ordering induces anisotropy in the optical transition intensities [114]. Sugisaki et al. observed a strong optical polarization dependence of InP/$In_{0.48}Ga_{0.52}P$ QDs, which have nearly equal base size along [1$\bar{1}$0] and [110] directions [148]. They found, moreover, strong anisotropy also for the PL signal from $In_{0.48}Ga_{0.52}P$ layer. The authors suggest that the PL anisotropy from QDs is induced by anisotropic strain in the $In_{0.48}Ga_{0.52}P$ matrix because of lateral change in alloy composition along [1$\bar{1}$0] and [110] directions [148]. In our case, though, we do not observe any PL polarization anisotropy from $In_{0.48}Ga_{0.52}P$ and therefore, we can exclude the impact of matrix and buffer on PL polarization anisotropy from InP QDs and conclude that the measured PL anisotropy here is induced by the dots.

Nonzero magnetic field

For a further study of the origin of the polarization anisotropy we performed polarization-dependent PL measurements in a magnetic field **B** perpendicular to the surface of sample.

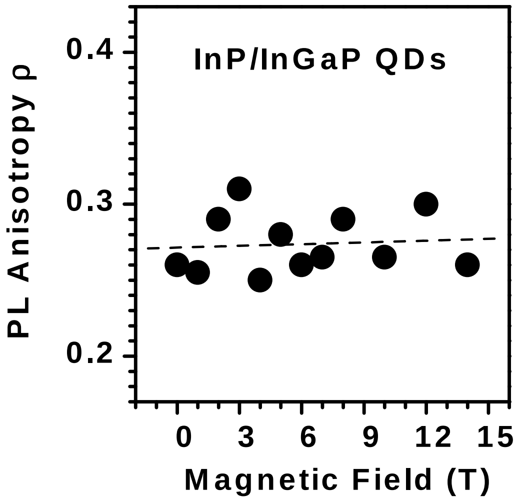

Figure 5.30: Polarization anisotropy ρ of InP/In$_{0.48}$Ga$_{0.52}$P QDs as a function of magnetic field perpendicular to the surface, measured at 10 K. The dashed line is a guide to the eye.

Generally, the magnetic confinement length λ_B is given by the cyclotron radius

$$\lambda_B = \sqrt{\frac{\hbar}{e_0 B}} \tag{5.7}$$

At about zero magnetic field the magnetic confinement length is much larger than the dot diameters. With increasing magnetic field the magnetic confinement length becomes gradually smaller. Finally, at a critical magnetic field B_c the magnetic confinement length and the dot diameter have the same value. Only for magnetic fields higher than B$_c$ the magnetic field energy determines the quantization energy.

For dots having average base length between 15 and 40 nm, B_c is between 2.5 T and 0.4 T, respectively; that means that at the latest for B higher than 2.5 T, the magnetic field determines the quantization energy in our dots. However, because of the broad PL line, we do not observe any energy shift of QD PL line dependent on magnetic field.

Figure 5.30 shows the PL polarization anisotropy ρ of InP QDs as a function of magnetic field, measured at 10 K. Apparently, ρ does not systematically depend on magnetic field when B rises from 0 to 14 T. The average value of background polarization anisotropy in this magnetic field is 27%. If the PL polarization anisotropy is due to the level crossing between hole states [147] (see Sec. 6.3.2) or the coupling between dots [149], the background polarization anisotropy should be magnetic field dependent. On the other hand, if the PL polarization anisotropy is mainly because of the anisotropic shape of the dots that causes an anisotropy in strain distribution, ρ should be nearly magnetic field independent.

In the case of elongated dots, most of the strain in dots is accommodated by the elastic deformation along the shortest axis. The asymmetric lateral strain results in the mixing of heavy-hole and light-hole states and causes the optical polarization anisotropy [146, 150].

Our results support that the optical polarization anisotropy in InP/$In_{0.48}Ga_{0.52}P$ QDs is because of their asymmetric shape and the dots are elongated along [110] direction, which confirms the results from structural analysis in this system (see also Chapter 7).

5.4.3 Dynamics of carrier recombination

Pryor et al. calculated the electronic structure of pyramidal InP QDs embedded in $In_{0.48}Ga_{0.52}P$ matrix [151] using the envelope approximation and including the effects of strain, piezoelectric polarization, and mixing among six valence bands. According to their calculation, the electrons are confined entirely inside the InP dot, whereas the holes are confined to multiple pockets in and around the dots. Such spatial separation of holes and electrons gives rise to an indirect heterointerface and a type-II system. Furthermore, based on Pryor's model, Janssens et al. theoretically investigated the exciton properties in InP/$In_{0.48}Ga_{0.52}P$ type-II QDs [152].

The results from time-resolved luminescence spectroscopy on our dots, however, do not indicate any trace of typical recombination dynamics in type-II systems. The low-temperature transients (10 K) from a QD sample containing 4 ML InP is shown in Figure 5.4.3. The solid line depicts the simple exponential decay with time constant τ=120 ps. The carrier lifetime in the other QD samples was also in the range of several hundred picoseconds (100–500 ps), in agreement with other time-resolved studies [153, 85, 154]. This carrier lifetime is typical for QD heterostructures having direct interfaces, i.e. type I, coinciding with our calculated band alignment as discussed in 5.4.1. In the case of type-II QDs, when the electrons localize within the dots and holes around the dots, the electron-hole overlap is smaller than for a type I, leading to a longer carrier decay time in nanosecond ranges, known from other type-II QDs such as GaAs/GaSb [155].

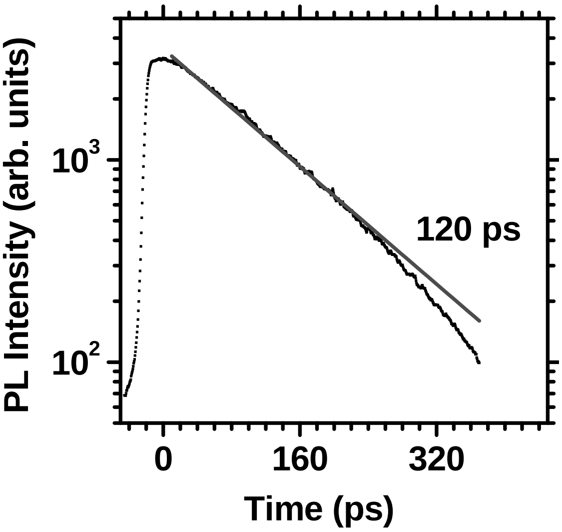

Figure 5.31: PL transient from a QD sample containing 4 ML InP coverage. The transient is detected at peak maximum (1.73 eV) and 5 K. The solid line shows the fit with the corresponding time constant.

In addition to results from time-resolved spectroscopy, the PL of InP/ $In_{0.48}Ga_{0.52}P$ QDs has been investigated under high pressure by Ulrich et al. [156]. This powerful technique can provide information on electronic structure of dots. The high-pressure PL indicated that both electrons and holes were located inside dots.

Altogether, we believe that Pryor's calculation is not realistic and cannot explain the experimental results, which point out that InP/$In_{0.48}Ga_{0.52}P$ QDs are type I.

A closer look at the time-resolved luminescence spectra shows that the transients may be better fitted using a biexponential decay model. Here, the reason may be a superposition of recombination processes in different dots due to lateral coupling. Such biexponential decay behavior is also reported for vertically coupled InP/$In_{0.48}Ga_{0.52}P$ QDs [154].

5.5 Conclusions

The growth, structural, and optical properties of $In_{0.48}Ga_{0.52}P$ lattice matched to GaAs as well as of InP quantum dots have been described and discussed.

Our results indicate that the grown $In_{0.48}Ga_{0.52}P$ alloy is almost disordered and ordering effects cannot change significantly the properties of the samples containing quantum dots.

The formation of QDs begins via the Stranski-Krastanow mechanism after deposition of a critical InP coverage of 3 ML. Intense PL from the InP quantum dots was observed between 1.6 and 1.75 eV. This optical emission is attributed to the direct transitions between the electrons and heavy-holes confined in the InP dots. The PL peak energy can be explained well using a realistic multivalley effective-mass approximation based on a type-I band alignment. The type-I band alignment of InP/$In_{0.48}Ga_{0.52}P$ QDs was furthermore confirmed by the carrier lifetime of about 100–500 ps, which is typical for type-I systems.

Chapter 6

InP/GaP system

6.1 Introduction

Analogous to the InP/$In_{0.48}Ga_{0.52}P$ system, InP QD formation on GaP via the Stranski-Krastanow mechanism is expected under proper growth conditions [47,157,158], driven by the 7.7% lattice mismatch between InP and GaP, which is 4% higher than between InP and $In_{0.48}Ga_{0.52}P$.

Optical emission from the direct-bandgap InP islands embedded in the indirect GaP matrix is expected to lie between the InP and GaP bandgaps in visible range [158]. The use of GaP as substrate has further potential advantages of larger strain and larger bandgap difference, allowing more flexibility in varying the emission wavelength. Additionally, structures on GaP could take advantage of a well-developed LED technology. Furthermore, using GaP rather than GaAs as the substrate allows easier extraction of the emitted light for vertical structures, since the substrate is transparent to the respective wavelength.

In this chapter the growth, structural, and optical properties, together with carrier dynamics and electronic structure of InP QDs in and on GaP will be presented and discussed.

Section 6.2 surveys the growth and structural properties: Because of the influence of the epitaxial GaP matrix on the InP QDs, first the growth of bulk GaP will be demonstrated, followed by the discussion of growth and structural properties of InP/GaP quantum structures, i.e. QWs and QDs. Section 6.3 surveys and discusses the optical properties of InP/GaP QWs and QDs and concludes with the discussion of carrier dynamics in this material system.

6.2 Growth and structural properties

6.2.1 Epitaxial GaP

GaP has been the most widely used material for light emitting diodes in the last decades and, hence, numerous groups have studied the growth and properties of this III-V compound. The growth of GaP using GSMBE has been reported in detail in [159, 160, 161].

Growth conditions

Samples were grown on (001)-GaP substrates; prior to growth, the substrates were etched in a solution of $4HCl : 4HNO_3 : 5H_2O$ [160]. After oxide desorption at a temperature of about 620°C, a 200–500 nm GaP layer was grown at a temperature between 500°C and 590°C and at a rate between 1 μm/h and 0.9 μm/h. It should be noted that the growth temperature during epitaxy on GaP substrate is obtained only from the thermocouple and the pyrometer was not usable due to large bandgap difference between GaP and GaAs, the pyrometer having been calibrated for the latter (see also Sec. 3.2.2). To have a P-stabilized surface, the PH_3 flux was kept sufficiently high.

During the growth process the RHEED patterns were monitored. The surface showed almost a (2×4)-reconstruction, indicating a P-stabilized surface (anion rich) that is also observed and has been calculated by other groups [159, 162, 163, 164, 165]. However, analogous to the growth of other III-V compounds, the change of III/V ratio can give rise to other surface reconstruction and at very low PH_3 flux the surface shows a (4×4)-reconstruction, which indicates a Ga-stabilized surface (cation rich), in agreement with most reports [163, 164, 165].

Three-dimensional surface: According to Reference [160], growth temperatures lower than 570°C result in three-dimensional growth surface, independently of III/V ratio, due to a reduction in the mobility of the Ga atoms on the GaP surface. We do not observe, though, the formation of three-dimensional surface at lower temperatures (500–570°C); the difference in calibration of temperature maybe gives rise to this different observation. On the other hand, we have observed that for very high PH_3 flux three-dimensional growth surface can occur; we suggest that the reason may be again the low mobility of the Ga atoms on the surface.

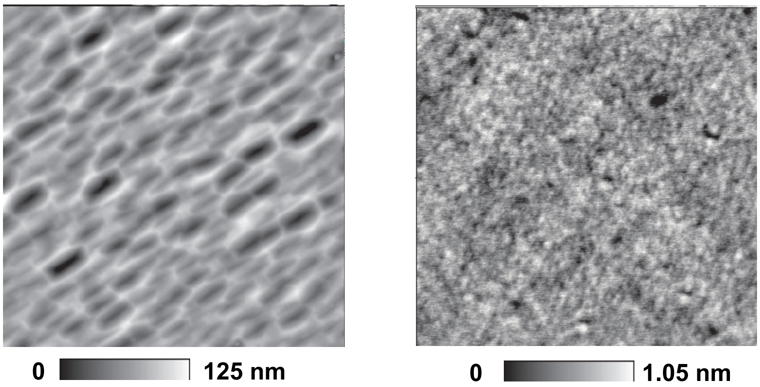

Figure 6.1: Atomic force micrographs of two GaP samples (measured size was $8.5 \times 8.5\ \mu\mathrm{m}^2$) grown at the same temperature (500°C) and rate (0.9μm/h) but under different PH_3 flux: The flux for sample with three-dimensional surface (left image) was 30% higher than for sample with smooth surface (right image). The height is scaled by different contrast given in the boxes on the bottom of images.

Furthermore, the two-dimensional surface growth of GaP at a low temperature of about 200°C using gas-source molecular beam epitaxy has been reported [166].

Oval defects: The other difficulty with GaP epitaxy is the control of oval defects. In MBE-grown GaAs layer the formation of this kind of defect is related often to the substrate preparation, incomplete removal of Ga oxides, or to the Ga source cells [167,168]. On the other hand, the study of oval defects in MOMBE-grown InP demonstrated that the origin of oval defects is the surface contamination and their density is independent of the growth parameters and only their size can be impacted by growth temperature and III/V ratio [169]. In the case of GaP epitaxial layer, we do not find any relation between presence

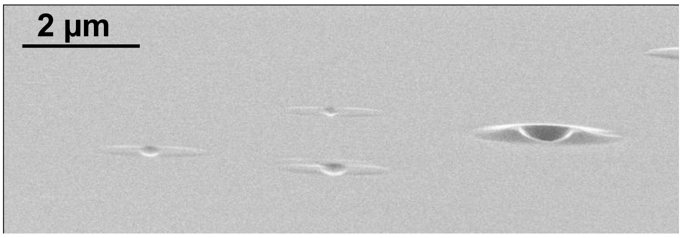

Figure 6.2: Scanning electron micrograph of the surface of epitaxial GaP, including oval defects. The sample was tilted about 45° (20 kV, 2.05 pA).

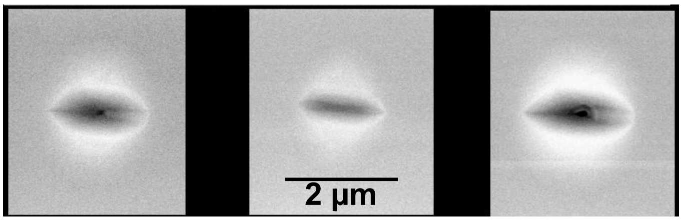

Figure 6.3: Plan-view SEM image of oval defects (20 kV, 16.5 pA).

of oval defects and substrate preparation or incomplete removal of Ga oxides. Since we are using the same Ga source for all samples, the defects can neither be attributed to the quality of Ga. According to our observation, however, the density of oval defects becomes lower when the growth temperature is reduced.

6.2.2 InP/GaP quantum wells

Two-dimensional, defect-free growth of InP on GaP is limited to very thin layers because of the large lattice mismatch of 7.7% between the two materials. After deposition of only about 1.8 monolayers of InP the formation of dots is observed (see Sec. 6.2.3). Thin InP layers embedded in (001)-GaP have already been studied using spectroscopic ellipsometry [170]. This section will present and discuss the growth of such ultrathin layers.

Growth conditions

The initial growth steps for samples containing InP quantum wells have been described in Section 6.2.1. After growth of 200 nm GaP buffer at 500°C and at a rate of 0.9 μm/h, the desired coverage of InP was deposited at a rate of 0.8 ML/s (0.22 μm/h). We measure the InP coverage in ML on the GaP surface taking into consideration the enlargement of the vertical InP lattice constant under compressive in-plane strain (6.730×10^{14} indium atoms/cm^2 in a compressed monolayer). Each sample contains a 1–9 periods InP/GaP superlattice with GaP thickness of 4 nm and InP thickness between 0.5 and 1.6 ML, dependent on sample. The resulting structures were capped with 10 nm GaP. The growth process was monitored using reflection high-energy electron diffraction; during GaP and InP growth, the surface showed a (2×4)-reconstruction, indicating two-dimensional growth.

Structural properties

Structural properties of the samples were characterized using double crystal X-ray diffractometry and atomic force microscopy. The AFM data confirm the absence of islanding in the structures.

Figure 6.4 displays experimental (004) rocking curves together with simulations from dynamical diffraction theory. Due to the InP/GaP superlattice, satellite peaks (denoted as S_{-1}, S_0, and S_1) appear in the proximity of the GaP substrate reflection (denoted as P). The position of the zero-order satellite peak S_0 with respect to P is connected to the mean vertical elastic strain inside the superlattice and, therefore, yields information on the average amount of indium. Consequently, S_0 shifts from -1000 to -2000 arcsec as the InP coverage is increased from 0.8 to 1.5 ML. Good agreement between experiment and simulations is achieved (see Fig. 6.4); the best fit parameters (d_{GaP} = 42.5 Å, d_{InP} =2.6, 4.0, and 5.3 Å) agree with the RHEED data as monitored during growth. Furthermore, the existence of pendellösung fringes in the experimental rocking curves reflects the high structural quality of the InP/GaP layers.

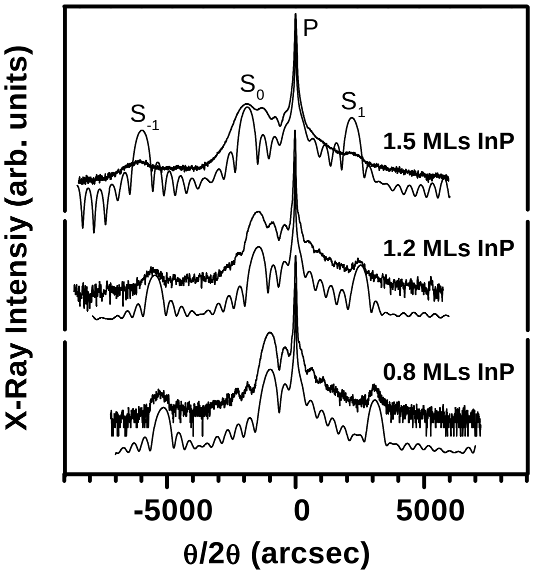

Figure 6.4: X-ray rocking curves (004) of InP/GaP superlattices with different InP coverage along with respective simulations (solid lines, below the curves). The best fits are obtained using d_{GaP} = 42.5 Å, d_{InP} =2.6, 4.0, and 5.3 Å for the lower, middle, and top curve, respectively. With decreasing InP coverage, the zero-order superlattice satellite (S_0) shifts from -2000 to -1000 arcsec towards the GaP substrate peak (P).

6.2.3 InP/GaP quantum dots

The growth of large (400 nm in lateral size and 100 nm in height) relaxed InP islands on GaP using organometalic vapor-phase epitaxy after deposition of about 1.2 ML InP is reported in Reference [47]. Likewise, Junno et al. reported the formation of relaxed InP QDs on GaP after deposition of about 3 ML InP using chemical beam epitaxy [157]; according to their studies, the height of islands changed between 5 and 20 nm. This section will discuss and demonstrate the growth and structural properties of our own InP quantum dots grown on and in GaP.

Growth conditions

After oxide desorption, a 200 nm GaP buffer layer was grown at 500–565°C at a rate of 0.9 μm/h. The growth was then interrupted while the substrate temperature was being reduced. Subsequently, the desired coverage of InP was deposited at 410–490°C, followed by a growth interruption of 60 s. The InP growth rate has been varied between 0.08 and 0.22 μm/h for different samples. Each sample contains one to five periods InP/GaP with InP coverage between 1.8 and 5.8 ML and GaP thickness of 5–20 nm, dependent on sample. The resulting structures were capped with GaP. At the beginning of InP growth, the RHEED pattern appeared streaky, indicating two-dimensional growth (see Sec. 6.2.2), and became gradually spotty and less intense after deposition of about 1.8 ML of InP (three-dimensional growth). The samples used for atomic force microscopy and scanning electron microscopy studies were grown without cap layer.

Structural properties

The quality of InP and GaP layers were examined in the first step by X-ray measurements. DCXD studies reveal a good structural quality of the InP/GaP samples. Figure 6.5 displays experimental (004) rocking curves together with simulations using dynamical diffraction theory for a sample containing 5 periods InP/GaP with InP thickness of about 0.65 nm (2.1 ML) and GaP thickness of about 12.6 nm. The cap layer thickness is 15 nm. Analogous to the InP/GaP QWs (Fig. 6.4), due to the InP/GaP superlattice, pronounced satellite peaks (denoted as S_{-2}, S_{-1}, S_0, and S_1) appear beside the GaP substrate reflection (P). The existence of pendellösung fringes in the experimental rocking curves once more confirm a good structural quality.

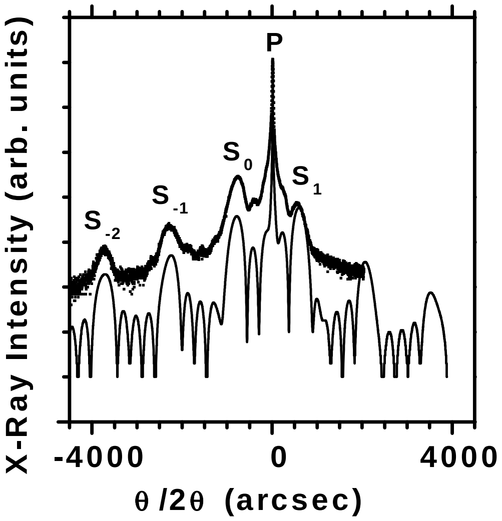

Figure 6.5: X-ray rocking curves (004) of InP/GaP QDs (dots) and respective simulation (solid lines).

Both the *in situ* RHEED measurements and the AFM studies indicate that dot formation begins after deposition of about 1.8 ML of InP. The size and the area density are strongly dependent on growth conditions.

Effect of InP coverage: AFM investigation of samples grown under same conditions (temperature, PH_3 pressure, growth rate) with different InP cov-

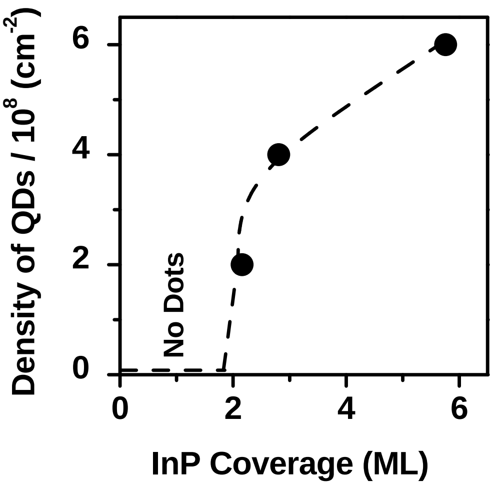

Figure 6.6: Area density (dots per 10^8 cm^2) as function of InP coverage. The samples were grown under same conditions; data have been obtained from AFM studies. The dashed line is a guide to the eye and indicates the evolution of dot formation.

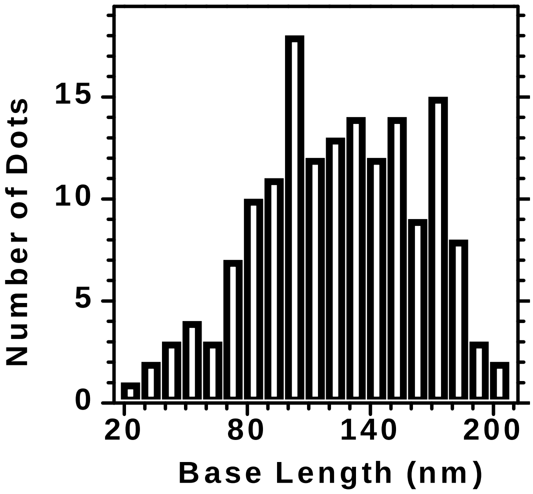

Figure 6.7: Histogram of the lateral size of quantum dots in the sample containing 5.8 ML InP coverage; data have been obtained from AFM measurement.

erage has shown that the dot density changes in the range of 2–6×10^8 cm^{-2} for samples with InP coverage between 1.9 and 5.8 ML grown at 450°C with a rate of about 0.08 ML/s (see Fig. 6.6). Apparently, the size of dots is nearly independent of InP coverage. The average lateral length and the height for the sample containing 5.8 ML InP are about 100 nm and 20 nm, respectively (Fig. 6.8). A relatively broad distribution of dot base size with standard deviation of 40 nm is found for this sample (see Fig. 6.7). The amount of InP contained in the wetting layer (whose thickness is determined from both the onset of QD formation and from PL measurements) and in the QDs (as determined from their dimensions and densities measured with AFM) is consistent with the total amount of InP deposited.

These dots are significantly larger than those typically observed in other systems with high lattice mismatch. Island size depends on a variety of factors including the specific properties of the material system and the growth conditions, one of which is the effect of PH_3 flux that will be discussed next in this section.

Furthermore, higher magnification AFM images reveal that the larger islands in our distribution are probably composed of two up to four smaller dots that have conglomerated (”quantum flower”, see Fig. 6.9); a detailed statistical analysis shows no indication, however, of a multi-modal size distribution (Fig. 6.7). Preference for cluster nucleation (”flowering”) may be here either

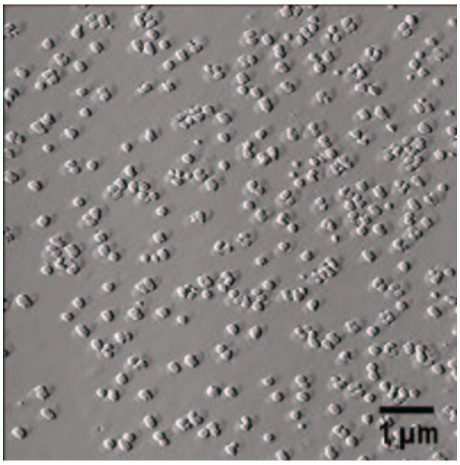

Figure 6.8: Atomic force micrograph of InP quantum dots with 5.8 ML InP coverage on a (001)-GaP surface.

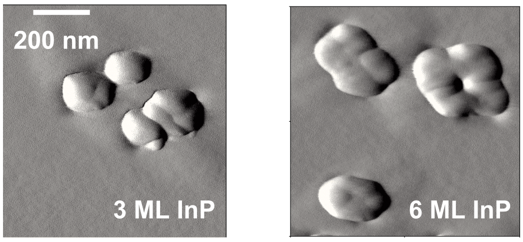

Figure 6.9: Atomic force micrograph of large dots from two samples containing 3 and 5.8 ML InP.

because of reduction of the surface energy (Oswald ripening) or because of already existing dots.

Additionally, the large size of the InP/GaP QDs compared to other III-V QDs can be explained by the total strain energy. The total strain energy in the continuum mechanical model is proportional to the elastic constant and the square of the lattice-mismatch degree [10]. Because of larger elastic constants in bulk InP than in bulk InAs [11], a higher strain energy in the InP/GaP system is expected, which should lead to earlier strain relaxation and larger dots (see also Sec. 2.5).

Effect of PH_3 flux: According to our observations, higher phosphorus flux leads to smaller quantum dots. This agrees with what is reported for InP/GaP-MOVPE islands in Reference [47]. The same effect has also been observed for the InAs/GaAs system, resulting in QDs as large as 100 nm [51]. Figure 6.10 shows an AFM image from a sample containing 3 ML InP. The dots in this sample are significantly smaller than those in Figure 6.9 because of the higher PH_3 flux used. Furthermore, higher PH_3 flux results in an increase of QD area density. The data for the two samples from Figure 6.9 and Figure 6.10 are compiled in Table 6.1.

PH_3 flux	**area density**	**base length**	**height**
1.5	2×10^8	100	18
2.2	5×10^9	25	3

Table 6.1: Area density per cm^2 and average base length and height in nm of InP QDs grown under different PH_3 flux (SCCM), data have been obtained from AFM studies. InP coverage is about 3 ML.

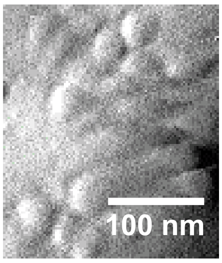

Figure 6.10: AFM micrograph of a sample containing 3 ML InP grown under high PH_3 flux.

Geometry of InP quantum dots: SEM studies of the uncapped InP reveal a truncated pyramidal shape for large QDs (see Fig. 6.11). SEM cannot provide, however, information on the shape of small and capped dots. As for TEM studies, the plan-view image of InP/GaP QDs does not appear like the typical TEM images from other III-V QD systems (see also Sec. 5.3.2). Figure 6.12 shows dark-field plan-view TEM images of a QD sample containing 2.1 ML InP. The average base length of QDs for this sample is about 19.5±0.6 nm; the height of the dots, according to high-resolution TEM, is between 3 and 5 nm. The interpretation of these TEM images is not straightforward. The high-resolution TEM image is also not helpful because of high noise; the image exhibits a diffuse shape for dots. Altogether, it is very difficult to make statements about the shape of small InP/GaP dots.

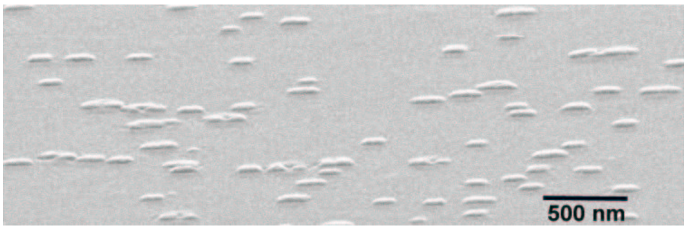

Figure 6.11: Scanning electron micrograph of InP quantum dots.

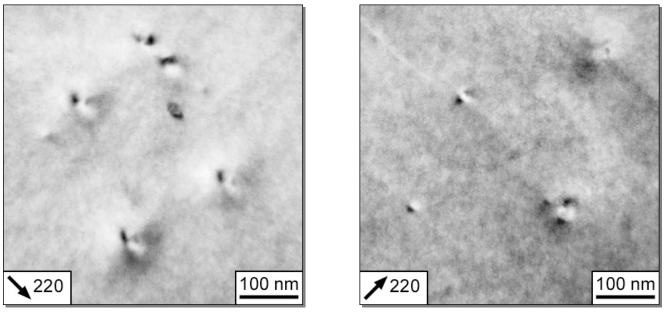

Figure 6.12: Dark-field plan-view TEM image of a QD sample containing 2.1 ML InP coverage. Average base length of dots is 19.5±0.6 nm.

6.3 Optical properties and carrier dynamics

Optical properties are determined by the electronic structure, which depends strongly on the structural properties of quantum dots and on strain. To obtain the electronic structure of InP quantum structures, we will again apply our simple model described in Section 5.4.1.

6.3.1 Electronic structure

To obtain the electronic structure of QDs, we first calculate the band alignment between the strained InP layer and the GaP matrix.

The band alignment, including strain effects, is estimated using the model-solid theory by Van de Walle [7]. For the resulting band alignment we calculate the localization energies for both electrons and heavy holes as functions of InP thickness. Because the lateral dimensions of the QDs are much larger than their vertical dimensions (see Sec. 6.2.2), analogous to InP/$In_{0.48}Ga_{0.52}P$ system, we neglect the lateral confinement effects and also model the QDs as slices (see Sec. 5.4.1). Within this simple, multivalley effective-mass approximation, we find that for the InP/GaP QWs with InP coverage thinner than about 3 nm (8 ML), the Γ-like electrons in InP layer are located at a higher energy than the X states in the GaP layer — for instance, in the case of ultrathin QW (thinner than 1 nm) the Γ-like electrons in InP layer are about 500 meV higher in energy than GaP X states — leading to localization of electrons in the X valley in the GaP. Hence, the structure is type II (see Fig 6.15). Our model indicates that for the QDs, on the other hand, the Γ-like electrons in InP are located approximately at the same energy as the X valley in the GaP matrix, implying that the electrons localize in both materials. For this reason, the electrons in both the InP and GaP layer are similarly available for carrier recombination, and the band alignment for InP QDs embedded in a GaP matrix is either type I or a mixing of type I and type II. Figure 6.13 shows the corresponding band alignment for ultrathin InP QWs and InP QDs (modeled as quantum slice). It should be noted that this simple model cannot give the exact image of electronic structures of QDs and in order to obtain the realistic electronic structure, it is necessary to compare our model with the experimental results discussed in the next sections.

6.3.2 Optical emission from ultrathin InP/GaP quantum wells

In the related material system, InP/$In_{0.48}Ga_{0.52}P$, intense photoluminescence due to radiative recombination of heavy-holes and electrons in both InP QDs

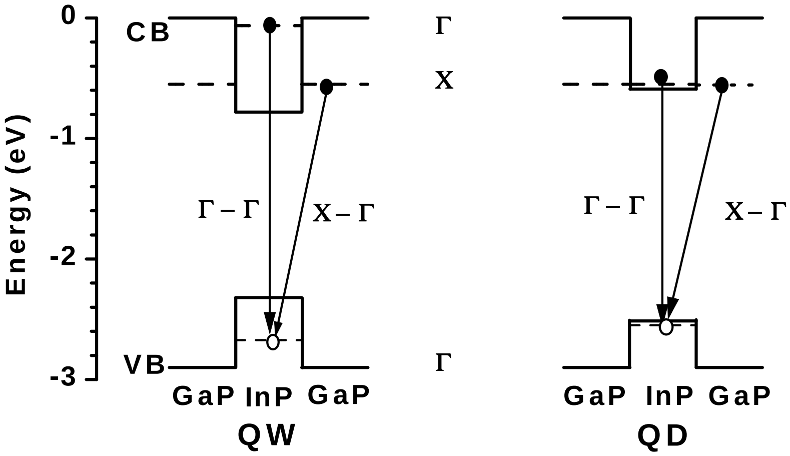

Figure 6.13: Valence and conduction band alignment schema of the pseudomorphic InP/GaP QW and QD. The arrows indicate the possibilities of electron-hole recombination.

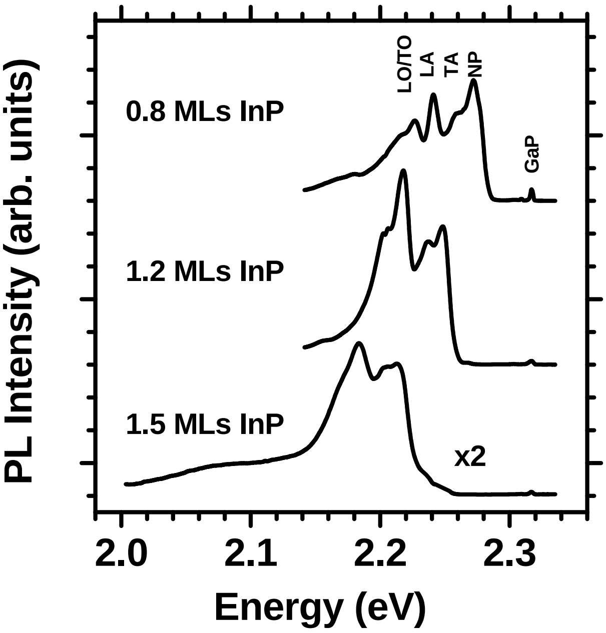

Figure 6.14: Photoluminescence spectra of samples with different InP coverage measured at 5 K.

and InP QWs embedded in $In_{0.48}Ga_{0.52}P$ is observed at energies between 1.6 and 1.9 eV (see Sec. 5.4). Similarly, optical emission from InP QWs embedded in the indirect GaP matrix is expected to lie between the InP and GaP bandgap.

Photoluminescence of InP/GaP quantum wells

Figure 6.14 shows the PL spectra of three InP/GaP structures. The InP layers in the structures remain two-dimensional because the InP coverage is considerably lower than the critical thickness for island formation [158]. The measurements were carried out at 5 K with an excitation density of about 20 W/cm^2 provided by the 325 nm line of a He-Cd laser; the emission was dispersed in a 1 m monochromator and detected by a CCD camera. The PL emission from the sample with 0.8 ML of InP consists of four intense PL lines in the energy range of 2.22–2.28 eV with full width at half maximum of 15±2 meV. The total emission intensity grows linearly with increasing excitation power density between 1 and 20 W/cm^2. Samples with more InP coverage have similar emission with all lines redshifted. These PL spectra are also similar to those of $GaAs_xP_{1-x}$/GaP [171,172,173] and AlP/GaP [174] type-II quantum wells. The energy differences between the highest energy PL line and the other three transitions are 12, 30, and 40 meV for all samples. The energy separations between

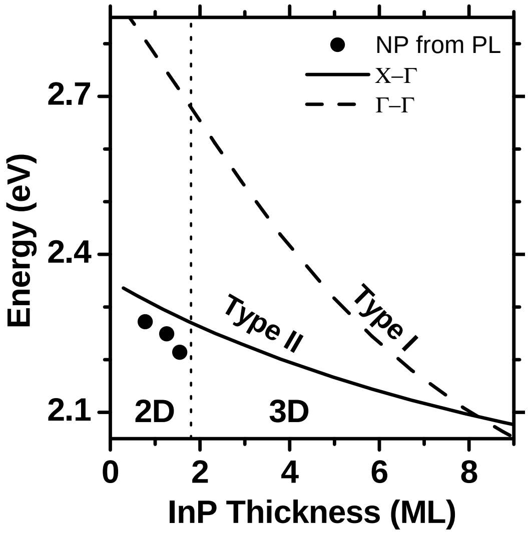

Figure 6.15: Calculated recombination energies of electron and heavy hole in InP/GaP structures as functions of InP nominal thickness for type-II (solid line) and type-I (dashed line) system. Solid circles show the experimental no-phonon PL peak energies.

the peaks and the independence of these separations with respect to InP coverage suggest that the three emissions peaks with lower energy are phonon replicas of the highest-lying peak. The separations agree well with the transversal acoustic (TA), longitudinal acoustic (LA), and either transversal optical (TO) or longitudinal optical (LO) phonon near the X points in the GaP Brillouin zone with energies of 13.2, 30.4, and 44–45 meV, respectively [175, 176]. These energies are not appreciably changed for $\mathrm{In}_y\mathrm{Ga}_{1-y}\mathrm{P}$ with small In mole fraction [175]. Thus, we identify the highest energy peak in each spectrum as the no-phonon (NP) emission and the lower energy peaks as its phonon replicas. In contrast to the similar $\mathrm{GaAs}_x\mathrm{P}_{1-x}$/GaP system, albeit with much thicker quantum wells [172], the relative intensity of this no-phonon line compared to the other three lines does not appear to decrease with the decreasing thickness of the InP layer. In these very thin InP layers, however, the Γ-X mixing is probably strongly affected by interface roughness, the interdiffusion of In and Ga, and disorder. The broad emission at the lower energy side of the PL spectrum for the 1.5 ML QW could be related to defects in the highly strained two-dimensional InP layer, which also result in the somewhat decreased total PL intensity compared to structures with thinner InP. Note that island formation already occurs for InP depositions of 1.8 ML (see Sec. 6.2.3), only slightly thicker than this 1.5 ML sample.

The calculated electron to heavy-hole transition energy as function of InP thickness for both the type-I transitions (Γ-valley electrons in the first subband of the InP quantum well with heavy holes in the InP) and type-II transitions (X-valley electrons in the GaP with heavy holes in the InP) is shown in Figure 6.15. Our calculations also include the coupling of adjacent InP quantum wells, since the superlattice constant ($d_{\mathrm{InP}}+d_{\mathrm{GaP}}$) is less than 5 nm. This calculated energy configuration resembles that of the $\mathrm{GaAs}_x\mathrm{P}_{1-x}$/GaP system, whose PL spectra are also similar [171]. The same QW thickness dependence of band alignment has also been observed for essentially unstrained GaAs/AlAs QW structures [177, 178]. The calculated type-I transitions have energies exceeding 2.7 eV for InP coverage of less then 2 ML, while the calculated type-II transitions lie between 2.25 and 2.35 eV. As seen in Figure 6.14, measured energies of the no-phonon transitions (solid circles in Fig. 6.15) are between 2.2 and 2.3 eV, in very good agreement with the calculated type-II transitions and much lower than the calculated type-I transitions. A type-I relationship becomes favorable when the InP is thicker than about 8 ML, a thickness only realizable in QDs [158]. Thus, the experimentally determined PL energies for the 2D InP films are in much better agreement with the calculation assuming a type-II system.

Raman scattering

To obtain information about the phonons in strained layers, we performed Raman spectroscopy on ultrathin InP/GaP QWs. Figure 6.16 shows the Raman

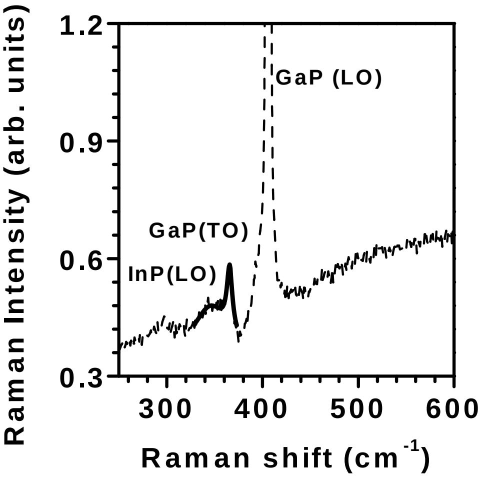

Figure 6.16: Raman spectrum of strained InP/GaP QWs (dashed line). The solid line exhibits the fit using: InP(LO)=43 meV and GaP(TO)=45 meV.

spectrum of a sample containing nine periods InP/GaP with InP thickness of about 0.4 nm and GaP thickness of about 4 nm. The longitudinal optical phonon from GaP is a well-known feature. We can also see the scattering from transversal optical phonon in GaP shifted by 365.7 cm^{-1} (45 meV) and weak scattering from LO phonon in InP shifted by 345.8 cm^{-1} (45 meV). The strain-induced shifts of the GaP LO phonons indicate the misfit strains, which are known to exist in this monolayer superlattice.

Time-resolved photoluminescence

In order to investigate the dynamics of carrier recombination in InP/GaP heterostructures, we performed time-resolved PL measurements at 5 K. The transients exhibit an exponential decay with a decay time of 19±1 ns detected at different energies (NP, TA, LA, LO), which is nearly independent of the InP coverage in the range of 0.8 to 1.5 ML. Figure 6.17 shows the PL transients detected at 2.24 eV (a) and 2.27 eV (b) along with their fits.

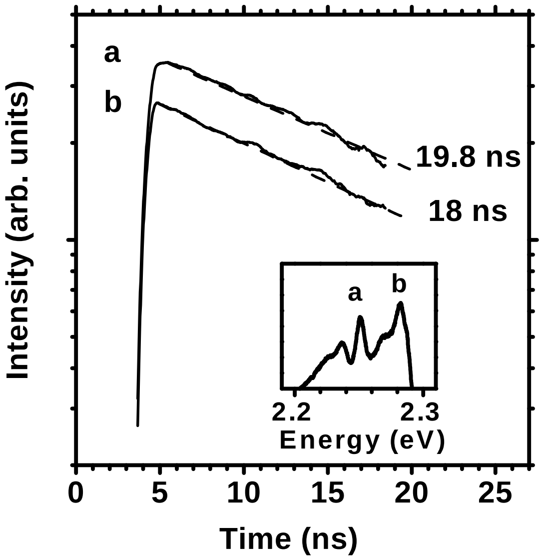

Figure 6.17: PL transients from the sample with 0.8 ML InP coverage. The transients were detected at 2.24 eV (a) and 2.27 eV (b) at 5 K. The dashed lines show the fit with the corresponding time constant. The inset shows the PL spectrum with the positions of the detection energies marked by a and b.

The results from time-resolved PL further confirm our band alignment modeling: Compared to the carrier lifetime in a thin strained type-I system of about 100 ps [179], the significantly longer carrier lifetime for ultrathin InP/GaP QWs can only be explained by a type-II band alignment in this system.

6.3.3 Optical emission from InP/GaP quantum dots

The growth of InP quantum dots is also reported in References [47, 157]. However, the dots in both publications do not exhibit any luminescence. Junno et al. reported unsuccessful photoluminescence and cathodoluminescence measurements [157]. They assume the large strain in the system to change the conduction band confinement into zero and this to be the reason of no luminescence from InP/GaP heterostructures.

This section presents and discusses the emission from InP QDs embedded in GaP matrix.

Photoluminescence of InP/GaP quantum dots

Figure 6.18 shows the PL spectra of three InP/GaP structures, one containing strained two-dimensional InP layers (sample A) and the others QDs (samples B and C). For comparison, the luminescence from the epitaxial GaP buffer is also shown. The InP/GaP samples consist of five periods containing 0.5 ML (QW sample), 1.9 ML (QD sample B), and 2.1 ML InP (QD sample C), respectively. The InP growth rate was about 0.08 μm/h for sample B and 0.22 μm/h for

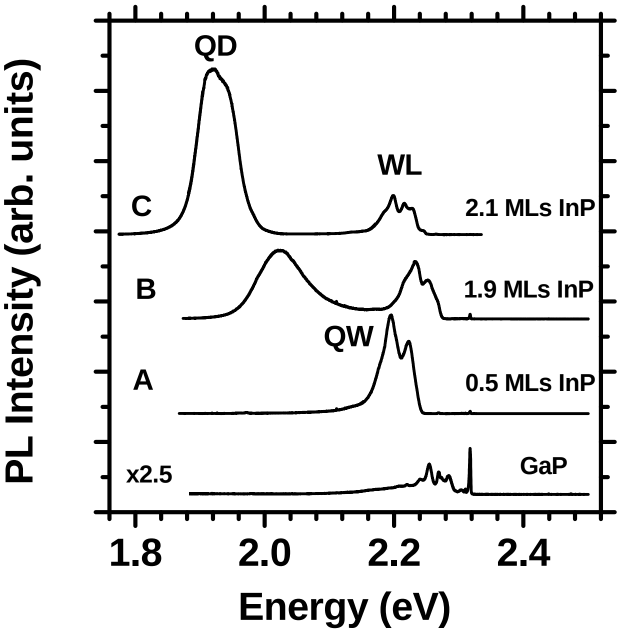

Figure 6.18: Photoluminescence spectra of samples with different InP coverage measured at 5 K, excited by the 325 nm line of a He-Cd laser.

sample A and C. The measurements were carried out at 5 K, excitation was done using the 325 nm line of a He-Cd laser with a density of about 20 W/cm^2.

The PL emission from the two-dimensional InP sample consists again of two intense and relatively narrow lines separated by 30 meV (see the discussion about PL line shape in Section 6.3.2). For InP coverage greater than 1.8 ML, both RHEED and AFM indicate three-dimensional growth resulting in quantum dots (see Sec. 6.2.3). The PL from such samples includes additional emission at about 2.0 eV, being attributed to radiative recombination of heavy-holes and electrons in the dots. The reason for the redshift of the QD luminescence in sample C compared to that from sample B can be the higher InP coverage in sample C. The PL associated with the 2D InP wetting layer remains, but is shifted to lower energy and is weaker. These effects resemble those of the InAs/GaAs system and indicate that a part of the wetting layer is consumed in the formation of the QDs [180].

All PL spectra of InP/GaP QD samples indicate a simple Gaussian shape whose width is determined by the size distribution in a QD ensemble [129]. At low excitation density (3 W/cm^2) the full width at half maximum of the PL line, dependent on growth conditions, varies between 40 and 70 meV.

Temperature-dependent photoluminescence: Figure 6.19 shows the temperature evolution of the PL from an InP/GaP QD sample. The excitation density was 10 W/cm^2. As the temperature is increased from 5 K, the luminescence shifts from the wetting layer to the QDs due to the interplay between various capture and recombination channels. At 80 K the PL from the wetting layer vanishes. This behavior is similar to what we observe in the InAs/GaAs system and in the GaSb/GaAs system [121].

In the temperature dependence of the PL, two distinct temperature regimes can be recognized. In the first regime (5–80 K) the overall PL intensity increases, whereas, in the second regime (80–300 K) it decreases (see Fig. 6.20). The integrated PL intensity is proportional to the number of excited electron-hole pairs that radiatively recombine. This radiative recombination, and with it the total PL intensity, is determined by two effects:

(1) The increase of PL intensity with increasing temperature at lower temperatures may result from electrons which were in the GaP barrier and in the InP wetting layer thermally escaping into the QDs where the recombination rate is much higher. On the other hand, the rise of PL intensity could also

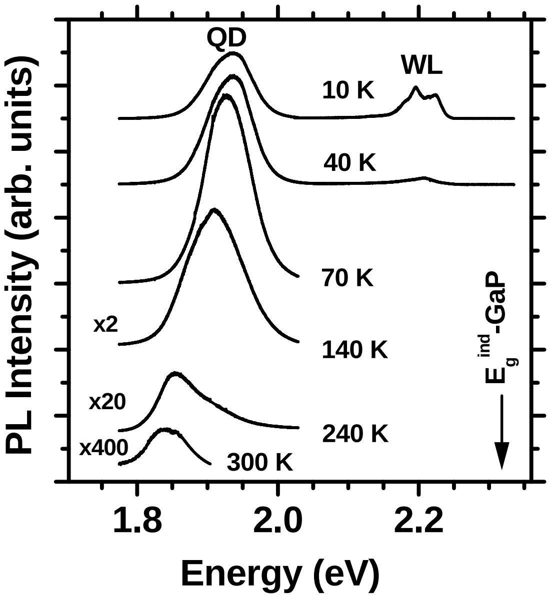

Figure 6.19: Temperature dependence of the PL spectra of sample C with InP QDs resulting from 2.1 ML InP coverage.

be due to the existence of QDs with type-II band alignment or existence of vacancies in the InP QDs which capture some of the excited electrons. The captured electrons are localized lower than Γ valley in the InP QD and recombine nonradiatively [181]. Only when the electrons can gain energy and are released into the Γ-valley state in the InP QD, for example by thermic activation during increasing of temperature, the electron-hole pairs are able to recombine radiatively, resulting in higher overall-PL intensity.

(2) The decrease of PL intensity with increasing temperature at higher temperatures is mainly due to the reduced spatial localization of the electron population and therefore to a decrease in the electron-hole overlap.

For temperatures below 80 K the first effect is stronger than the second one. Therefore, we observe an increasing integrated PL intensity, whereas for temperatures above 80 K, the second effect dominates and we observe a decreasing integrated PL intensity.

Using the temperature dependence of the luminescence intensity, we determine the activation energy of heavy holes in the QDs. For temperatures higher than 220 K, the localization energy of electrons can be neglected compared the localization energy of heavy holes. Thus, the slope of a plot for temperatures higher than 220 K gives the activation energy for heavy holes; we obtain an

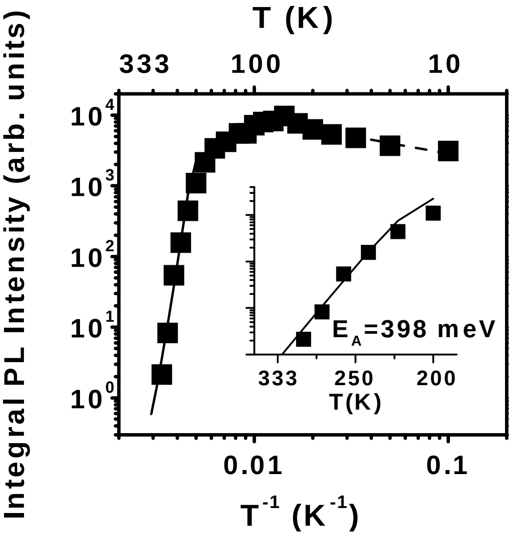

Figure 6.20: Integrated PL intensity as function of inverse temperature. The activation energy is derived from the slope of the solid line.

activation energy of 398 ± 20 meV, which is the energy difference between the heavy-hole subband and the valence band discontinuity, $\Delta E_v - E_{hh1}$. This activation energy also corresponds to the energy difference between the QD luminescence and the GaP indirect bandgap, indicating that the GaP X-states have approximately the same energy as the Γ-like lowest electronic subband in the InP (see Fig. 6.20) in agreement with the band alignment modeling discussed in Section 6.3.1.

The analysis of temperature evolution of the PL linewidth for QD samples with different InP coverage indicates that the linewidth is not significantly affected by the temperature rising, as expected for PL from QDs.

In order to obtain information on the dynamics of carrier recombination in InP QDs, we determined the activation energy of heavy holes in the QDs. We have analyzed the integrated PL intensity from the QDs as a function of inverse temperature (see Fig. 6.20). For temperatures higher than 220 K the localization energy of electrons can be neglected against the localization energy of heavy holes. Hence, the slope of a plot for temperatures higher than 220 K gives the activation energy of heavy holes; we obtain an activation energy of 398 ± 20 meV, which corresponds to the energy difference between the QD luminescence and the GaP indirect bandgap. This result agrees with our band alignment modeling and indicates that the Γ valley in the InP QDs is approximately aligned with the X valley in the GaP matrix (see Fig. 6.21);

however, this result cannot provide any indication whether the band alignment is type I or a mixing of type I and type II, which was discussed in Section 6.3.1

The temperature dependence of the PL maxima from InP QDs is typical for III-V semiconductors [136], i.e., shifting toward lower energy with increasing temperature due to the temperature dependence of the bandgap (see the discussion of the temperature dependence of bandgap in Sec. 5.4.1). However, the small difference in temperature dependence evolution of InP bulk and GaP bulk does not allow to distinguish whether it rather follows the temperature dependence of the first or latter (see Fig. 6.22).

Excitation density-dependent photoluminescence: Figure 6.23 shows the photoluminescence spectra as function of excitation density, obtained from a QD sample containing 2.1 ML InP. As expected, the PL peak position exhibits a weak blueshift by about 10 meV when the excitation power increases by factor 100. The same behavior has been observed for ultrathin InP QWs having type-II band alignment; apparently, although the nonequilibrium holes and electrons are confined spatially separated in such type-II structure, the dipole layer formation cannot affect the electron states significantly. Dipole layer formation is typical for type-II systems and leads to a strong blueshift of the PL peak with increasing of excitation density [155]. Since the impact of dipole layer formation on the energy of the X state is vanishing, the localized electrons in the GaP matrix stay at the same energy and only the energy level

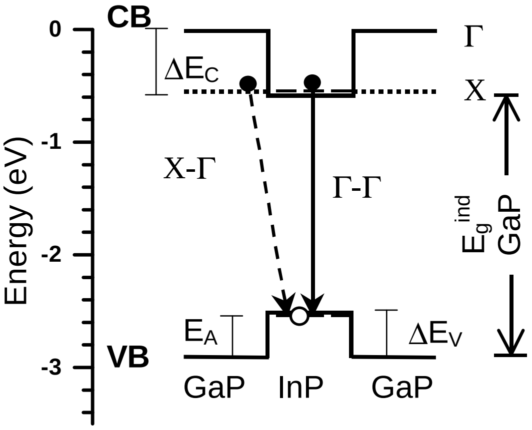

Figure 6.21: Band alignment schema of the InP QD embedded in GaP matrix along with respective activation energy for heavy holes (E_A) obtained from Arrhenius plot in Fig. 6.20. The arrows indicate two possibility of electron-hole recombination.

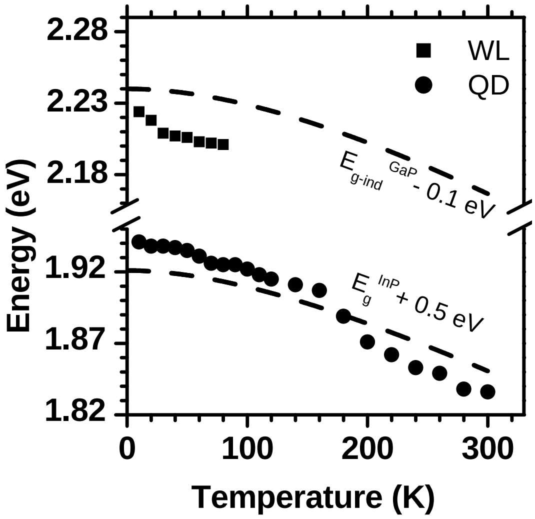

Figure 6.22: Temperature dependence of the PL peak maximum for the QDs (circles) and for the wetting layer (squares) from sample with 2.1 ML InP coverage. The dashed lines indicate the InP and GaP bandgap according to Varshni equation (Eq. 5.3), shifted in energy scale; fit parameters: $\alpha_{InP} = 4.9 \times 10^{-4}$ eV/K, β_{InP}=327 K, $\alpha_{GaP} = 6.2 \times 10^{-4}$ eV/K, and $\beta_{GaP} = 460$ K [137].

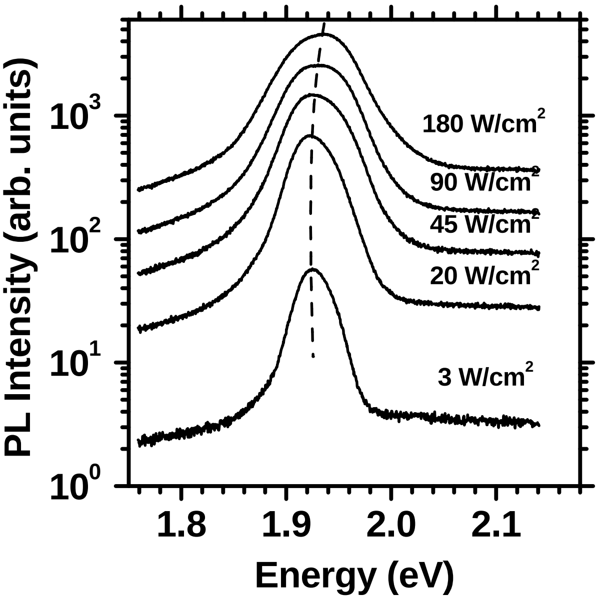

Figure 6.23: PL spectra from the sample with 2.1 ML InP coverage at different excitation densities. The dashed line shows the energy shift.

of the confined holes in the InP layer can be affected by the formation of dipole layer. Thus, we do not observe the blueshift typical for type-II systems. On

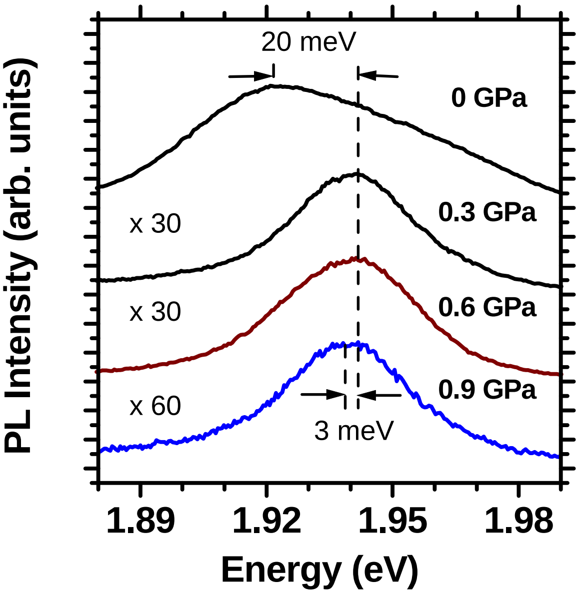

Figure 6.24: PL spectra from the sample with 2.1 ML InP coverage at different hydrostatic pressure. The dashed lines show the energy shift.

the other hand, in the case of InP QDs, the holes are again confined inside the dots, whereas electrons might be partly localized in the dots and partly in the GaP X valley. In such a mixed type I-II system the dipole layer formation does not significantly affect the band alignment and the reason for the blueshift is just the higher energy of confined carriers when the generated carrier density increases [182].

Furthermore, with rising excitation density the FWHM increases from 39 to 75 meV (see Fig. 6.23), indicating the participation of excited states.

Pressure-dependent photoluminescence: High-pressure studies of the low-temperature PL of quantum dots are a powerful method for getting information on electronic subband structure and have been demonstrated in InAs/GaAs [183, 184] and InP/$In_{0.48}Ga_{0.52}P$ [156] systems. This method is based on the very different pressure dependence of the conduction band minima at the X and Γ points in the Brillouin zone; information is obtained mainly by adjusting the energy levels into Γ-X degenerations.

To clarify the band alignment of InP/GaP QDs, we have investigated the samples using photoluminescence measurements under hydrostatic pressure up to 10 GPa. For the experiments the samples were chemically thinned in a solution of 4HBr : $100CH_3OH$ to a total thickness of about 30 μm and then cut into pieces of about 100 × 100 μm^2. The measurements were performed at 4 K using a diamond-anvil cell [185].

Figure 6.24 shows the PL spectra at different hydrostatic pressures. At ambient pressure the PL peak of the QDs is at about 1.922 eV and its intensity is two orders of magnitude larger than that of the wetting layer. With increasing pressure the QD emission diminishes abruptly in intensity and the energy of the PL maximum first blueshifts by about 20 meV at 0.3 GPa and then it redshifts by about 3 meV before the PL signal vanishes at around 1.2 GPa.

Higher pressure shifts Γ point in InP to higher energy until Γ-X crossover occurs at a very low pressure of less than 0.3 GPa. The slight redshift of the QD PL peak under pressure is typical for indirect in **k**-space but spatially direct recombination processes from the conduction band X valleys to hole states at the Brillouin zone center [186]. This result indicates that the peak at 1.922 eV (ambient pressure) is attributed to direct optical transitions between the two lowest electron and hole Γ-point states confined in the InP dots and, thus, a type-I band alignment for the InP/GaP QDs.

Since the bulk moduli of GaP and InP are different (see Table 2.1), one expects the X-valley splitting ΔE_X in the dots being reduced due to a pressure-induced relaxation of the built-in stress caused by lattice mismatch. The X-valley splitting for a zinc-blende crystal under a tensile uniaxial stress along [100] is given by

$$\Delta E_X = \Xi_u \frac{C_{11} + 2C_{12}}{C_{11}} \varepsilon_{xx} \tag{6.1}$$

where Ξ_u denotes the deformation potential at the Brillouin zone boundaries, C_{11} and C_{12} are elastic constants and ε_{xx} is the in-plane component of the strain tensor [187]. In fact, the QD emission is quenched at around 1.2 GPa most likely because of the X_{xy} valleys (for momentum in the layer planes) becoming higher in energy than the X states of the GaP barrier material. For the GaP X states, the X_{xy} is by $\Delta E_X/3$ lower than the degenerated X valley.

It should be noted that the PL spectrum at ambient pressure exhibits a slight shoulder at the higher energy side that vanishes rapidly with increasing pressure. The origin of this shoulder may be the the spatially indirect optical transition between localized electrons in the GaP X valleys with holes in the InP.

Polarization dependence photoluminescence: The linear polarization of the emitted light from the InP QDs was investigated. Figure 6.25 shows PL

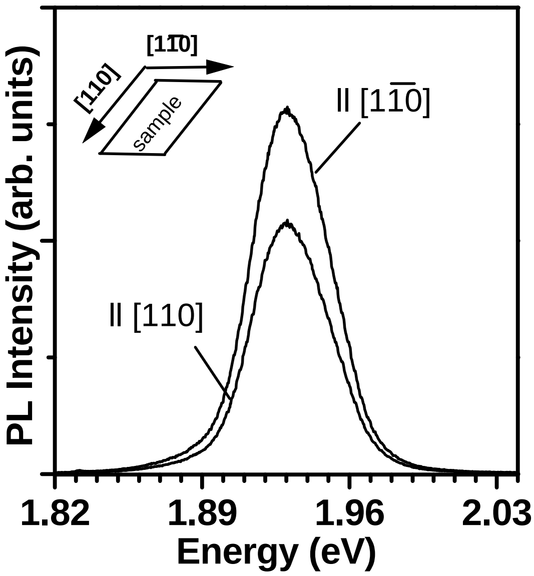

Figure 6.25: PL spectra polarized linearly along [110] and [1$\bar{1}$0] at 10 K from a InP/GaP QD sample containing 2.1 ML InP. The orientation of the sample is sketched in the upper-left edge.

spectra polarized linearly along [110] and [1$\bar{1}$0] at 10 K from an InP/GaP QD sample containing 2.1 ML InP. The spectra reveal a background polarization anisotropy

$$\rho = \frac{I_{[1\bar{1}0]} - I_{[110]}}{I_{[1\bar{1}0]} + I_{[110]}} \approx 19\%, \tag{6.2}$$

$I_{[1\bar{1}0]}$ and $I_{[110]}$ denoting the overall-PL intensity along the [1$\bar{1}$0] and [110] directions. No PL polarization anisotropy was observed between [100] and [010] direction. The PL polarization anisotropy of the two-dimensional wetting layer and InP/GaP QW samples vanishes.

The origin of PL polarization anisotropy in general has already been discussed in Section 5.4.2. Similarly to the InP/In$_{0.48}$Ga$_{0.52}$P system, for a closer study of the origin of PL polarization anisotropy ρ we have investigated PL polarization dependence on magnetic fields (see Fig. 6.26). When the magnetic field is increased the PL polarization anisotropy reduces gradually and at 14 T, ρ is only 8%.

Since the magnetic confinement length $\lambda_B = (\hbar/eB)^{1/2}$ at 1.5 T is about 20 nm, for the dots, having average base length of 20 nm, at magnetic fields higher than 1.5 T magnetic confinement is more dominant than spatial confinement. However, we do not observe any effects of magnetic field on both the

PL line shape or the PL peak position. The reason could be the broad PL line shape.

As discussed in Section 5.4.2, the dots' geometry-induced PL anisotropy should be nearly independent of magnetic field, on the other hand, the background polarization anisotropy due to the mixing of the heavy-hole and the light-hole states [189] or level crossing between hole states [147] might be magnetic field dependent.

Figure 6.27 shows an example of the calculation of magnetic field-dependent optical anisotropy by Takagaki [188] for InP QDs having rectangular geometry. This calculation is based on a model for the level crossing mechanism [147]. Because of the nearly parabolic band of the electrons, the two lowest electron states have a large energy separation. Hence, to simplify the calculation, only the lowest electron level has been taken into account. The wave function of this electron ground state has naturally s-type symmetry. As for the holes, the uppermost hole levels are separated with very small energy gaps. Similar to InAs dots [147], Takagaki's calculation yields that the highest hole state (hole ground state) does not have the s-type symmetry. This means that the optical transition takes place between the ground electron state and an excited hole state. With magnetic field, these levels shift in energy. As a consequence of the hole state having the predominantly s-type nature being not the ground state, the hole levels cross each other at certain magnetic fields. This is called level crossing and that is when we see the maximum optical anisotropy. In contrast

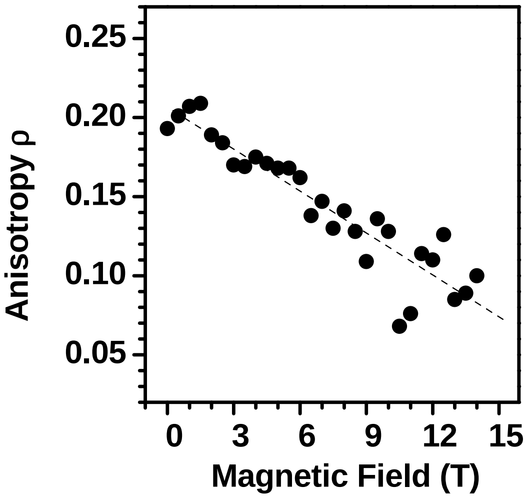

Figure 6.26: Polarization anisotropy ρ of QDs as a function of magnetic field, measured at 10 K. The dashed line is a guide to the eye.

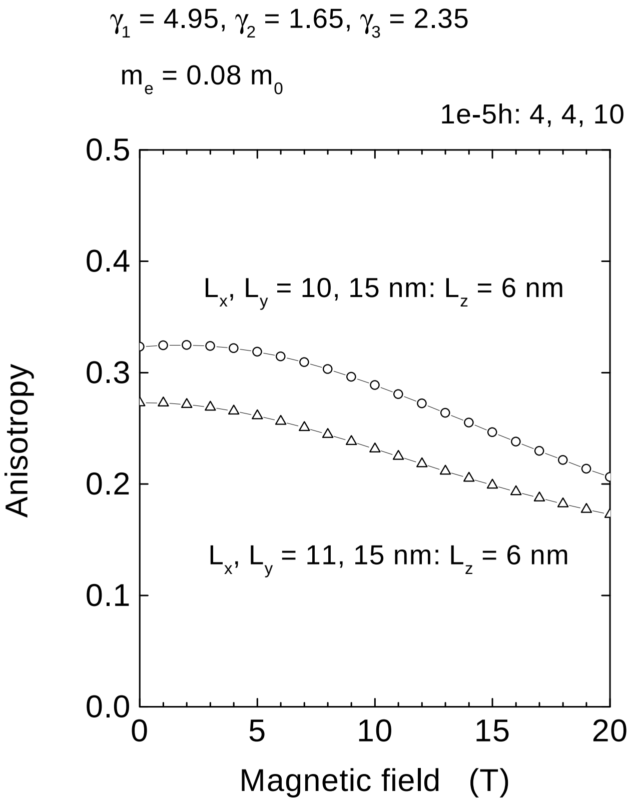

Figure 6.27: Calculation of the magnetic field dependence of optical anisotropy for InP quantum dots having rectangular geometry for two different sizes [188]. γ_1, γ_2, and γ_3 are the Luttinger parameters for InP.

to the level crossing calculation for InAs QDs by Takagaki et al. [147], where the s-type hole state was found among the top four hole states, in case of the InP dots the s-type symmetry was often found in the fifth level and the five hole levels must be taken into account [188].

To conclude, our experimental observations can be interpreted in terms of the level crossing mechanism and we can exclude the impact of dot geometry. However, it should be noted, due to the interplay of various parameters — for example, the strain effect and mixing of heavy-hole and light-hole states — it is very difficult to make a final statement about the origin of the optical anisotropy from InP QDs here.

6.3.4 Carrier dynamics in InP/GaP quantum dots

Williamson et al. calculated the electronic structure of a spherical InP QD embedded in GaP matrix [190]. According to their calculation, when the di-

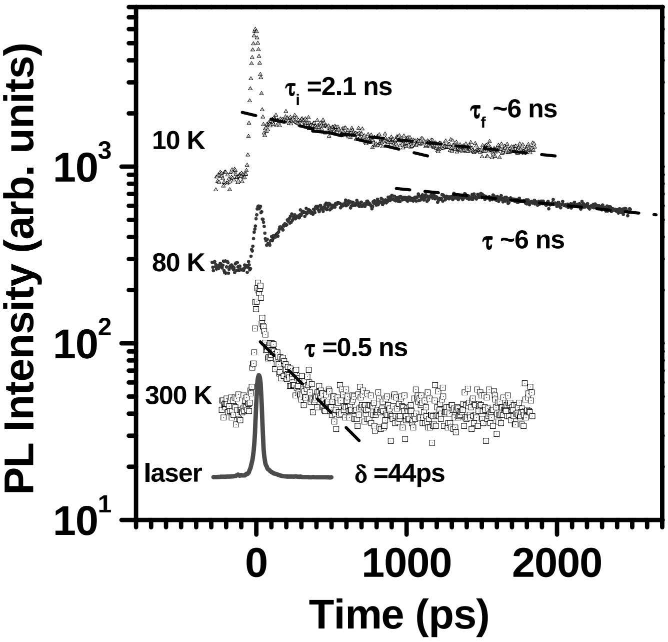

Figure 6.28: PL transients from a InP/GaP QD sample containing 2.1 ML InP coverage at three different temperatures, excited by the 395 nm line. The transient is detected at peak maximum (1.94 eV for 10 and 80 K and 1.85 eV for 300 K). The dashed line shows the fit with the corresponding time constant.

ameter of the InP QD (d_{QD}) is smaller than 6 nm, the Γ-like electrons in InP layer are localized at a higher energy than X states in the GaP layer and the band alignment of the dot is type II. However, they found that the strain in the InP/GaP system induces a new conduction state, which is lower in energy than the X valley in the unstrained GaP matrix and the Γ-like electrons in InP layer in a way that the electrons are localized in real space at the interface between the InP QD and the GaP barrier. This new interface conduction (IC) state is indirect in reciprocal space. Therefore, for large spherical InP QDs ($d_{QD} \geq$ 6nm) also an indirect transition is predicted. The calculated dipole transition matrix element between the IC state and the Γ-like holes in InP is five orders of magnitude smaller than for a typical type-I system [190], resulting in a smaller optical transition probability and a longer carrier lifetime.

For further study of the band structure and exploration of the carrier dynamics we have performed time-resolved PL measurements. The low-temperature transient (10 K) from QDs in the 2.1 ML InP/GaP QD sample fits with a bi-exponential decay with two different time constants τ_i and τ_f (Fig. 6.28), whereas the transient from the wetting layer can be fitted by a simple exponential decay with time constant τ_W. The initial (τ_i) and final (τ_f) decay times for the QD transient are about 2.1 ns and 6 ns, respectively. The decay times remain practically unchanged between 1.9 and 1.95 eV. The observed carrier lifetime for the other QD samples was also in the range of 2 ns. Additionally, we have observed for structures with two-dimensional InP (a pure type-II system) a decay time of about 25 ns.

Our results show that the initial decay time τ_i for the InP/GaP QDs is much shorter than the decay time of a pure type-II system and that supports our band alignment assumption for InP/GaP QDs that we are not dealing with a type-II system. The decay times, however, in the InP/GaP dots are longer than the decay times for the pure type-I InP/$In_{0.48}Ga_{0.52}P$ QDs, which are in the range of 100–500 ps (see Sec. 5.4.3). Generally, the radiative decay time τ_{rad} in a simple one-level model is given by

$$\tau_{rad} \propto \frac{1}{f} \tag{6.3}$$

where f denotes the oscillator strength and for excitonic recombination is given by the electron-hole overlap. If we assume an electron-hole overlap of 100% for an ideal type-I QD at low temperature and a carrier lifetime of about 500 ps as measured for InP/$In_{0.48}Ga_{0.52}P$ QDs, we expect for the dots with a carrier decay time of 2 ns an electron-hole overlap of about 25%. This value is too high for an indirect type-II system; although in the case of a mixed type-I-II QD system, when the electrons partly localize inside the dots and partly in the GaP matrix, the electron-hole overlap is smaller than for a type-I and larger than for a type-II system, resulting in an oscillator strength between that of type-I and type-II systems, which causes a carrier decay time longer than typical decay time in a type-I and shorter than in a type-II system. The amount of mixing (ζ) can be determined using perturbation theory that says ζ to be inversely proportional to the energy separation ΔE of the Γ-electron state in InP and the X-electron state in GaP:

$$\zeta = \frac{A}{\Delta E} \tag{6.4}$$

where A denotes the matrix element, whose value depends on the mechanism of the mixing process [191]; the optical matrix element for transition in type-II band alignment M_{II} is given by

$$M_{II} \approx M_I \left\langle \psi^e_{GaP} | \psi^e_{InP} \right\rangle \frac{A}{\Delta E} \tag{6.5}$$

where M_I is the optical matrix element for transition in type-I band alignment. ψ^e_{GaP} and ψ^e_{InP} are the slowly varying electron envelope wave functions in GaP and InP, respectively. Finally, the ratio of radiative lifetimes for type I (τ_I) and type II (τ_{II}) is given by [191]

$$\frac{\tau_{II}}{\tau_1} \approx \frac{\Delta E^2}{A^2} \frac{1}{\left\langle \psi^e_{GaP} | \psi^e_{InP} \right\rangle^2}. \tag{6.6}$$

If we assume such mixed system and that the carriers are able to recombine via only these two channels having time constants $\tau_I = 500$ ps and τ_{II}=25 ns for type-I and type-II band alignment, the participation of carriers in radiative recombination via the indirect type-II channel must be very low.

It should be noted that also for type-I InAs/GaAs QDs carrier lifetimes of about 1–2 ns have been reported [192,193,194] and compared to this material system, our InP/GaP QDs could as well be type I.

Now the question is whether the carriers can recombine radiatively via the indirect type-II channel or whether we are dealing with a pure type-I system. This question might be clarified by investigation of temperature-dependent transients PL. Figure 6.28 shows the low-temperature transient described above together with PL transients at 80 and 300 K that can be fitted by simple exponential decay with time constants τ_{80}=6 ns and τ_{300}=500 ps.

The lifetime for a free exciton in a quantum well is inversely proportional to the exciton population at $k = 0$ [195,196]. At finite temperatures, an increased thermal broadening of the free exciton distribution will reduce the $k = 0$ exciton population resulting in an increase of the exciton lifetime. In contrast to that, for the localized excitons in ideal QDs, thermal broadening has no effect on the exciton distribution in **k**-space. Thus, the exciton lifetime should be nearly temperature independent, in contrast to our observed decay time increase from 2 ns (10 K) up to 6 ns (80 K). One potential argument for the increasing decay time would be the activation of thermionic emission; though, this effect should result in a poorer PL efficiency of the QDs. The overall PL intensity, however, is at 80 K by a factor of three larger than that at 10 K. Apparently, the origin of increased decay time must be other mechanisms and the dynamics between the absorption and emission states here is very complicated: Although the carrier decay time is increased, the radiative recombination probability becomes larger. Such effect may occur when some new energy levels can participate in the radiative recombination only from a certain temperature up and the trapped carriers recombine radiatively via this new channel with a longer decay time; the large dots are, for instance, one potential recombination channel. To clarify this effect, theoretical modeling is necessary.

At higher temperature, the carrier lifetime decreases to a value of 500 ps (300 K) due to activation of thermionic emission and increase of nonradiative lifetime, as our observation.

Furthermore, the rise time is relatively large; at 10 K it is about 200 ps and increases rapidly up to about 1.5 ns for the transient taken at 80 K. Note that the sample was excited by 3.1 eV (395 nm), which is higher than the direct bandgap of GaP. At such measurement conditions, a large portion of the excited electrons can be captured by the GaP barrier and escape from that into the dots during the temperature increase by gaining thermal energy. At room temperature, the QDs are the most efficient recombination channel and the carriers are immediately trapped in the dots and consequently, the rise time is near zero.

The final decay time τ_f can be explained from the carrier transfer between dots of different sizes. In small dots the carriers are confined stronger than in large dots. On the other hand, the confinement levels in large dots are at lower energies. Thus, the carriers can travel from the smaller dots into the larger ones and, consequently, have a larger decay time [194].

It should be noted that we do not obtain optical emission from every InP QD sample and the optical properties in this material system are strongly dependent on the growth conditions. One reason can be the complicated band alignment of the InP dots, which depends on the dot geometry and can also be indirect in both **k**- and real space. Furthermore, we found that the samples containing dots with an average base length larger than 50 nm do not exhibit any PL, perhaps due to the relaxation of dots.

To summarize, our results from time-resolved PL of InP/GaP quantum dots do not provide direct evidence of a type-II band alignment. However, we may not exclude the existence of type-II band alignment for a part of dots, but we conclude that most of the dots having optical emission are type I. Our result is in contrast to modeling from Williamson et al. [190] (see the beginning of this section), who predicted an indirect type-II band structure for InP/GaP and a five orders of magnitude smaller dipole transition matrix element between the interface conduction state and the Γ-like holes in InP, which must result in a carrier lifetime range of several seconds and in vanishing radiative electron-hole transition. Therefore, we do not believe that the interface conduction state has any impact on the optical emission from InP/GaP QDs.

6.4 Conclusions

The growth, structural and optical properties of ultrathin InP QWs and self-assembled InP QDs on and in indirect (001)-GaP have been described and demonstrated. The QDs appear to form via the Stranski-Krastanow mechanism after a critical InP coverage of 1.8 ML is reached.

Intense PL from the QW structures is observed between 2.17 and 2.28 eV. The PL is explained as resulting from the spatially indirect recombination of electrons from the GaP X valleys with holes in InP and their phonon replicas. The highest energy no-phonon line of each PL spectrum can be explained well, using a realistic multivalley effective-mass approximation calculation based on a type-II band alignment. The type-II band alignment is further confirmed by the carrier lifetime of about 19 ns, which is much longer than in type-I systems.

InP deposition greater than the critical thickness for dot formation results in InP islands whose size is dependent on the growth conditions. Supercritical InP deposition under a sufficiently high PH_3 flux results in relatively small and dense dots with optical emission peaks between 1.9 and 2.0 eV, depending on InP coverage. This energy is 0.5 eV higher than the InP bulk bandgap due to strain, quantum confinement, and probably also Ga interdiffusion. This luminescence persists to above room temperature, but decreases due to the holes being thermally excited out of the QDs. Our band alignment modeling exhibits for InP dots a border case between type I and type II. However, the results from pressure-dependent PL indicate that the optical emission is attributed to the direct transitions between the two lowest electron and hole Γ-point states confined in the InP dots. This result is supported by the observed carrier lifetime of about 2 ns and, hence, we suggest a type-I band alignment for InP/GaP QDs. Potential application as a light emitter in this range, but with higher efficiency than for currently-used systems, is promising.

Chapter 7

Ordering of InP quantum dots

7.1 Introduction

Advantageous for QD-based optoelectronic devices is the formation of coherent (defect-free), ordered arrays of uniform quantum dots. The present chapter surveys the ordering of InP quantum dots embedded in and on the surface of $In_{0.48}Ga_{0.52}P$ on (100)-oriented GaAs substrates. This chapter is organized as follows: First, planar ordering of quantum dots will be discussed and the experimental results for both uncapped and buried InP quantum dots will be presented. In section 7.3 vertical ordering in the $InP/In_{0.48}Ga_{0.52}P$ system will be demonstrated and discussed.

7.2 Planar ordering

For planar ordering of quantum dots three modes must be taken into account: ordering in shape, ordering in size, and ordering in position (see Fig. 7.1).

In a dilute dot array, where the average distance between quantum dots is larger than their average lateral size, the shape equilibration of the dots

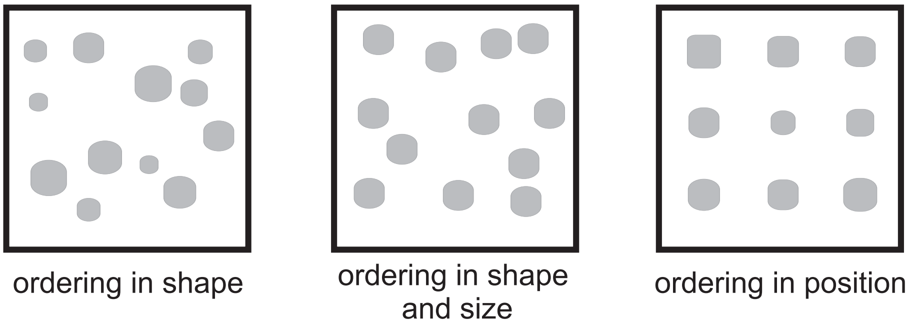

Figure 7.1: Illustration of ordering of quantum dots.

occurs due to material migration on a single quantum dot, which is faster than the mass transfer between different dots. The equilibrium shape of a strained coherent quantum dot can be derived by minimizing its total energy with respect to its shape. The total energy is estimated by the sum of surface energy (considering facets formation) and elastic energy in the thermodynamic model. For a quantum dot with volume V the surface energy is of course proportional to the surface area and scales with $V^{2/3}$. The elastic energy scales linearly with volume. Hence, equilibrium shape of a quantum dot depends on volume and from the theoretical point of view, for any given volume of a quantum dot there is an equilibrium shape [39].

In the opposite case, for a dense dot array the average distance between quantum dots is in the order of their average lateral size. Therefore, material migration on a single quantum dot and mass transfer between quantum dots can occur on the same degree. Hence, the shape ordering may happen by material exchange between quantum dots or by Ostwald ripening (see Sec. 3.4.1).

If the quantum dots can equilibrate, the change of the total energy of a heteroepitaxial system containing QDs may be described as a function of the dot size in a thermodynamic model [31]. Hence, the optimum size of quantum dots can be derived again by minimizing the total energy with respect to the QD size. Shchukin et al. have calculated the phase diagram for the stability of a square lattice of coherently strained islands and found that there is some region where the islands have optimum size and do not undergo ripening [31].

On the other hand, the real conditions during growth of InP quantum dots are far from the thermodynamic model. The growth of a cap layer or cool-down of the heteroepitaxial system immediately after formation of quantum dots may destroy the equilibration of QDs. In such a case, the kinetics of quantum dot formation governs the growth. Kinetic models consider microscopic processes observed during formation of self-organized quantum dots such as deposition and diffusion, and attachment and detachment of adatoms to dots. Additionally, the strain field is calculated using elasticity theory [197, 198, 199, 200].

In kinetic models the strain results in two effect: First, it reduces the energy barrier for diffusion of adatoms and second, strain energy at the edge of island rises with island size in such a way that for large islands the bonding energy of edge atoms is lower than the strain energy at the edge, leading to the detachment from the island. Both effects cause a stabilization of the quantum dot size due to kinetic mechanisms [197, 198]. According to the kinetic model, small islands grow faster than large ones. When the islands reach a certain size they stop to grow and in such a way the ordering in size is simulated in this model. Ordering of quantum dots in position can be explained by this model, too [197]. It is to note that from an experimental point of view the kinetic factors may change strongly with different growth procedures being used, as shown by Patella et al. [201].

If the quantum dots are ordered in shape, size, and position, the highest degree of ordering will be reached.

The planar ordering of the uncapped quantum dots in this work is investigated using the two-dimensional fast Fourier transformation (FFT) of AFM data (AFM power spectra) together with grazing incidence small-angle X-ray scattering (GISAXS) and diffuse X-ray scattering experiments. The planar ordering of the buried quantum dots (capped dots) is investigated using the plan-view transmission electron microscopy (TEM) together with grazing incidence X-ray diffraction (GID).

7.2.1 Uncapped quantum dots

To study the planar ordering effects in position of quantum dots independently of their shape and size, I have processed AFM data using two-dimensional fast Fourier transformation. The AFM data are from several samples grown under same conditions with different InP coverage. A size of 1 μm^2 has been maintained for AFM examination in all cases (Fig. 7.2). The samples contain three layers InP separated by 15 nm $\text{In}_{0.48}\text{Ga}_{0.52}\text{P}$; the growth was finished with deposition of InP layer and, hence, the InP quantum dots at the surface are uncapped. Only the centers of dots in AFM images are Fourier transformed; therefore, the AFM power spectra (Fig. 7.2) characterize only the spatial ordering of the dot positions and are independent of shape and size. From the AFM power spectra it can be seen that with increasing InP coverage the center of the Fourier spectra ($|q| < 3 \times 10^{-2}\text{Å}^{-1}$) changes from a circle-like to a square-like pattern (Fig. 7.2). Obviously, for the samples with more InP coverage, a two-dimensional lattice of dots becomes increasingly important. For these samples, ordering is increased not only in that the dot period becomes less volatile, but also in the appearance of directional ordering of the dot positions. Apparently, increase of QD density and of their lateral size force the dots into ordering. This leads to the formation of well-ordered domains (Fig. 7.3). The domains exhibit uniform shape as well as ordering in size (relative standard deviation

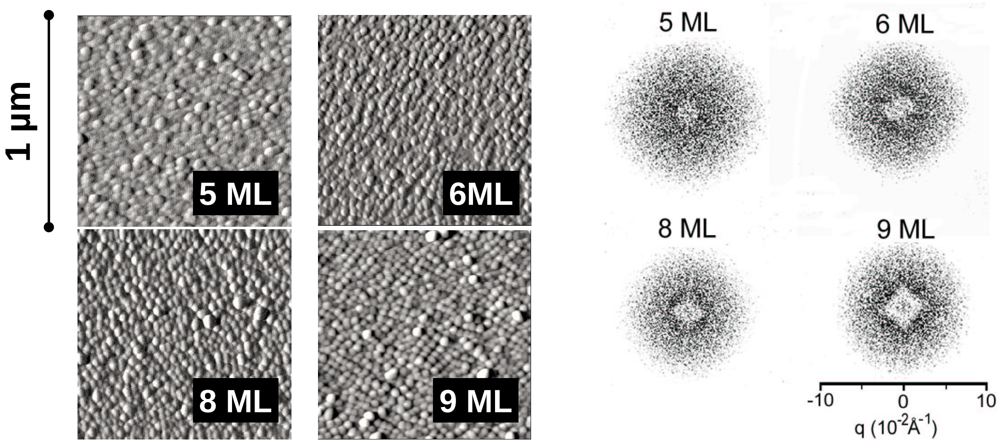

Figure 7.2: AFM images and their Fourier spectra in 1 μm^2 fields of several samples.

$< 9\%$). The size of a such well-ordered domain is between 400 and 600 nm^2.

The simulations for self-organized island formation in strained material systems using a kinetic model by Barabsi [197] predicts an improvement of ordering in position for high island density, which is associated with more InP coverage. The same effect is observed for In$_x$Ga$_{1-x}$As quantum dots in GaAs [202].

To better quantify the planar ordering as well as the ordering in shape and size, GISAXS measurements have been done. Due to better statistics compared with the respective AFM power spectrum, the GISAXS intensity pattern allows a richer quantitative analysis. The diffuse scattering image exhibits strong correlation peaks along the four $\langle 100 \rangle$ directions, indicating that ordering is

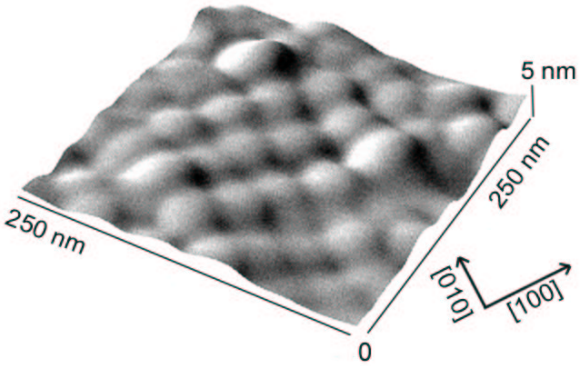

Figure 7.3: AFM image of the sample containing 9 ML InP.

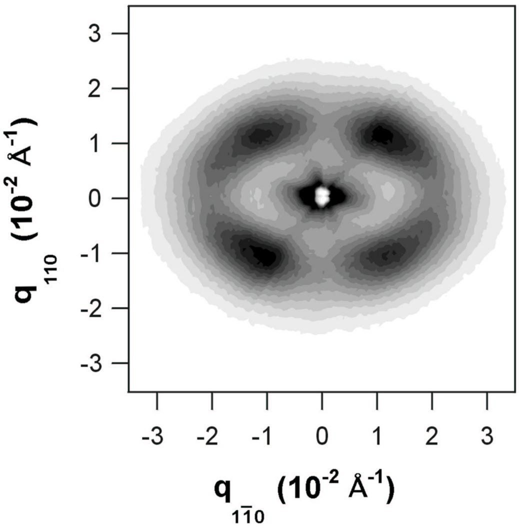

Figure 7.4: GISAXS intensity pattern of sample with three times 9 ML InP, the last InP layer is uncapped (Fig. 5.15a). Highest intensity is indicated by black, lowest intensity by white (linear scale). The angle of incidence, was chosen as $\alpha_i = 0.40°$. The four peaks indicate strong dot-to-dot correlation along the $\langle 100 \rangle$ directions with a mean distance of $\overline{d}_{[100]} = \overline{d}_{[010]} = 40$ nm.

predominant along these directions (see Fig. 7.4). This result is consistent with AFM and TEM data. Although the overall shape of the diffuse scattering is ellipsoidal, the four correlation peaks form a square, indicating a four-fold symmetry of ordering. From the peak spacing of the GISAXS intensity pattern we can evaluate a mean dot-to-dot distance of $\overline{d}_{[100]} = \overline{d}_{[010]} = 40$ nm for the sample with 9 ML InP coverage, whose AFM data is also depicted in Figure 7.2. This value agrees with that of the AFM power spectrum and the TEM data (see Sec. 5.3.2). We also observe ordering along all other azimuthal directions with different dot-to-dot distances along [110] ($\overline{d}_{[110]} = 46$ nm) and along $[1\bar{1}0]$ ($\overline{d}_{[1\bar{1}0]} = 30$ nm), respectively (Fig. 7.5).

There is a remarkable difference between the AFM power spectrum (Fig. 7.2) and the GISAXS intensity pattern (Fig. 7.4): The overall shape of GISAXS is ellipsoidal with the long axis collinear with [110], whereas the AFM power spectra show a circular shape. Note that in the AFM power spectra only the dot positions are considered, whereas with GISAXS both the dot shape and dot-to-dot correlation contribute to the scattered intensity. Consequently, we attribute the observed differences to the shape of elongated dots with the long axis along [110] and the short one along $[1\bar{1}0]$. However, due to missing "thickness fringes" in the diffraction pattern — as often observed [203, 63] — a quantitative analysis is difficult. Possibly, the QD size distribution is not narrow enough. It is interesting to note that the GISAXS signal mainly arises from the uncapped QDs at the surface, whereas the signal from the buried QDs is given by a small shoulder only. The latter can be explained by the small difference in electron density between the InP QDs and the embedding $In_{0.48}Ga_{0.52}P$ host lattice, whereas for uncapped QDs a high electron difference is present. A quantitative analysis requires theoretical simulation for diffuse intensity. This should include the exact dot-to-dot correlation function containing both shape and dot distances.

To distinguish between the GISAXS signal from buried and uncapped dots, we have performed GISAXS measurements on samples containing a single uncapped QD layer. Figure 7.6 shows an AFM image of a sample containing 5 ML uncapped InP. The estimated average island base length resulting from statistical analysis of AFM data is about 45 ± 10 nm and 30 ± 10 nm along [110] and $[1\bar{1}0]$, respectively. The GISAXS measurement performed on this sample indicate again an elliptically shaped intensity distribution (see Fig. 7.7) reflecting the asymmetric quantum dot shape, which agrees well with the AFM results. Additionally, there are four strong peaks indicating a positional ordering of quantum dots along $\langle 100 \rangle$ directions. Apparently, these peaks are weaker than the peaks from Figure 7.4. It is difficult, however, to compare both GISAXS patterns (Fig. 7.4 and 7.7). The reason is that the lateral ordering in position

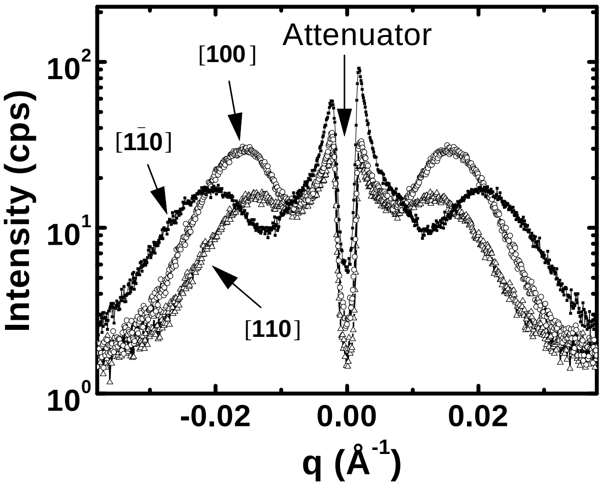

Figure 7.5: GISAXS intensity (Fig. 7.4) for selected orientations of the scattering vector $\mathbf{q}$. The respective scattering vector $\mathbf{q}$ is collinear with $[1\bar{1}0]$, [110], and [100]. Open triangles correspond to a sample with a $In_{0.48}Ga_{0.52}P$ cap layer. The specular beam at q=0 has been attenuated.

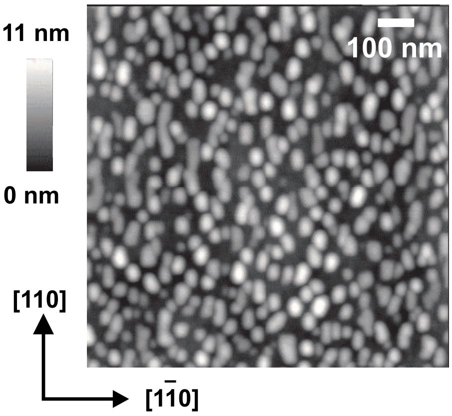

Figure 7.6: AFM image of uncapped InP quantum dots.

of quantum dots may be enhanced by both effects: increase of InP thickness and vertical correlation due to stacked structures. But it is certain that the capped dots in a single InP layer are ordered in position.

The anisotropic shape of quantum dots will be discussed later in Section 7.2.3.

7.2.2 Buried quantum dots

In contrast to GISAXS, grazing incidence diffraction (GID) is, additionally, sensitive to strain inside the sample and can, thus, be used as a probe for buried QDs [204]. Moreover, through appropriate choice of the angles of incidence and exit, α_i and α_f (see Chapter 4), the information depth Λ can be varied. At or below the critical angle of total external reflection ($a_c \approx 0.27°$),

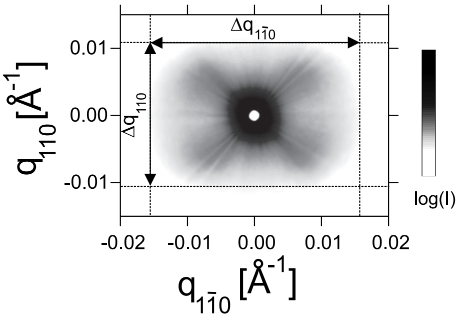

Figure 7.7: In-plane GISAXS pattern of the sample containing a single InP layer on the surface (uncapped QDs). Four peaks, which are due to positional ordering of QDs along the ⟨100⟩ directions superimpose on the elliptically shaped intensity distribution. Highest intensity is indicated by black, lowest intensity by white (logarithmic scale).

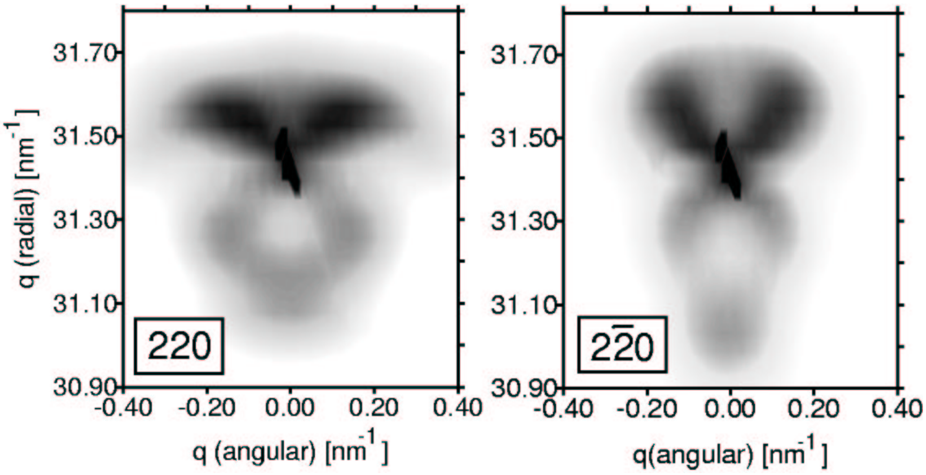

Figure 7.8: In-plane GID map. The measurements were performed at the critical angle of total external reflection **(a)** around 220, and **(b)** around $2\bar{2}0$ reciprocal lattice points. Highest intensity is indicated by black, lowest intensity by white (logarithmic scale).

the scattering is restricted to a depth of $\Lambda = 5$ nm, whereas at larger angles Λ may exceed the total thickness of the multilayer. Figures 7.8a and 7.8b show the in-plane intensity distribution of a 10-period InP/$In_{0.48}Ga_{0.52}P$ quantum dot superlattice sample with InP thickness of 5 ML separated by 5 nm $In_{0.48}Ga_{0.52}P$ layers. The in-plane intensity distribution was measured in the proximity of the 220 and $2\bar{2}0$ reciprocal lattice points, respectively. The strong central peak at $q_{radial} = 31.4$ nm^{-1} arises from scattering in the perfect part of the $In_{0.48}Ga_{0.52}P$ matrix and partly from the underlying GaAs substrate, while the surrounding diffuse scattering is mainly due to strain fluctuations. In the diffuse regime we observe — in correspondence to GISAXS — four strong correlation peaks that are attributed to in-plane positional ordering along the $\langle 100 \rangle$ directions.

On-zone bright field images in plan-view TEM indicate ordering in position also for buried quantum dots (see Sec. 5.3.2). It seems that the InP quantum dots are aligned with their edges to the $\langle 100 \rangle$ directions, which is in contrast to the results from GISAXS studies. As demonstrated by Liao et al., however, the interpretation of TEM images requires multiple-beam dynamical image simulation [70].

7.2.3 Shape anisotropy and strain distribution

From AFM studies, GISAXS, and GID patterns it has been concluded that the investigated InP quantum dots are elongated in [110] direction. This is in contrast to observations by other groups. Jin-Phillip et al. have reported on InP/$In_{0.48}Ga_{0.52}P$ QDs extended along the $[1\bar{1}0]$ direction [128]. However, the lateral anisotropy $\alpha = |c-d| / (c+d)$ in their case is about 50% and significantly larger than in our case, where it is less than 20% (c and d denote the axes of the dots in $[1\bar{1}0]$ and [110] direction, respectively). Likewise, Sugisaki et al. found elongated InP islands along $[1\bar{1}0]$ [148]. It is interesting to note that InAs QDs grown on (001)GaAs also tend to elongate along the $[1\bar{1}0]$ direction [55,141,144].

To avoid misinterpretation of crystallographic orientation of the samples, the $[1\bar{1}0]$ and [110] directions are controlled by the orientation of oval defects on the backside of GaAs substrate. The results agree with the data specified by the providers.

Generally, the orientation of QDs is dependent on the surface symmetry determined by the surface reconstruction and by the anisotropy of adatom diffusion, which is typically larger in $[1\bar{1}0]$ than along [110].

The reason for our InP QDs being elongated in [110] direction is not yet clear. Possibly, the observed (2×1) surface reconstruction for the $In_{0.48}Ga_{0.52}P$ matrix (see Chapter 5) may have induced the shape anisotropy. To explain this shape anisotropy, theoretical modeling is required. As discussed in Section 7.2, the equilibrium shape of quantum dots can be described by a kinematic model. Such calculation may explain the asymmetric shape in terms of total energy minimizing.

Note that the miscut of substrate also affects the equilibrium shape. Miscut larger than 2° results in a small enough terrace width on the substrate surface to change the size, shape, and positional correlation of quantum dots [205]. The terrace width, additionally, depends on the state of step bunching at the sample surface that may be changed by employing different growth conditions and different buffer layer thicknesses. For the investigated samples, however, the miscut, as estimated from X-ray measurements, is smaller than 0.05°, corresponding to a terrace width of at least 300 nm, which is far too high to affect the InP quantum-dot formation.

To obtain more information on the shape anisotropy of quantum dots, strain distribution inside and around QDs is studied using X-ray diffuse scattering (see Chapter 4) along with respective kinematic simulations [206, 207].

How can strain relaxation provide information on the shape of quantum dots? From elasticity theory it is known that the strain distribution inside a quantum dot (at a given fixed shape) is independent of QD size [208]. However, as will be discussed here, it is strongly dependent on the shape of quantum dot. Study of strain distribution, therefore, may serve as a sufficiently sensitive method for the investigation of QD shape.

Examination of dot shape in such a way, however, is an indirect method: The measured X-ray scattering pattern is compared with respective kinematic simulations using linear elasticity theory. Because the simulation is strongly dependent on structural parameters such as shape, size, and chemical composition, the calculation can be refined until satisfactory agreement with experiment is achieved. A detailed description of this method is given in References [209] and [210].

The linear elasticity theory has been used successfully for the InAs/GaAs system with lattice mismatch of about 7% [130]. Therefore, we can use this theory in good approximation for the InP/$In_{0.48}Ga_{0.52}P$ system having lower lattice mismatch (about 3.8%). The continuum elastic properties of III-V materials exhibit four-fold spatial symmetry. In particular, the [110] and [$1\bar{1}0$] directions are treated equivalently. Although, different strain relaxation may occur due to asymmetric shape of QD along these two directions. Note that, considering exact atomistic two-fold symmetry, Pryor et al. have implemented the strain relaxation for quantum dots [211] in their calculation. They found, however, that the anisotropic strain relaxation due to the shape of dots is much stronger than due to two-fold symmetry.

Figures 7.9a and 7.9b show the measured X-ray diffuse intensity patterns near the $1\bar{1}3$ and 113 reciprocal lattice points for uncapped InP quantum dots. The diffuse intensity is widely spread out in reciprocal space and peak position is shifted by $\delta q_{1\bar{1}0}$ for $q_{1\bar{1}0}$ and δq_{110} for q_{110}. Both $q_{1\bar{1}0}$ and q_{110} are found from the $In_{0.48}Ga_{0.52}P$ buffer reflection, which is marked by vertical white lines in Figure 7.9. The $\delta q_{1\bar{1}0}$ and δq_{110} shifts are in good agreement to the respective mean values of the total elastic strain components (averaged over the entirety of QDs)

$$\begin{aligned} \langle \varepsilon_{110} \rangle &= -\tfrac{\delta q_{110}}{q_{110}} \\ \langle \varepsilon_{1\bar{1}0} \rangle &= -\tfrac{\delta q_{1\bar{1}0}}{q_{1\bar{1}0}} \end{aligned} \tag{7.1}$$

if the $In_{0.48}Ga_{0.52}P$ buffer is used as reference. Evaluation of the measurements depicted in Figure 7.9 results in mean values of the total strain $\langle \varepsilon_{110} \rangle = (5.0 \pm 0.5) \times 10^{-3}$ and $\langle \varepsilon_{1\bar{1}0} \rangle = (9.2 \pm 0.5) \times 10^{-3}$. According to these results, the elastic relaxation is quite different for the [110] and [1$\bar{1}$0] directions, indicating the elongation of the QDs along the [110] direction. The reason is here that the lattice in the elongated direction can relax more efficiently due to the effect of the underlying GaAs substrate and $\mathrm{In}_{0.48}\mathrm{Ga}_{0.52}\mathrm{P}$ buffer. This yields smaller mean values of the total strain in the [110] direction.

In contrast to the results for the [110] and [1$\bar{1}$0] directions, the diffuse X-ray intensities near the 404 and 044 reciprocal lattice points are similar. This proves that the strain fields along the [100] and [010] direction are equal (see Fig. 7.10), which is related to a closely equivalent lateral size of the QDs for these directions. This result agrees well with the statistical analysis of AFM data discussed in Section 5.3.2, which indicates a high degree of symmetry.

Modeling: Only with a careful modeling a deeper understanding of the experimental data is possible. The following steps are used for our modeling: Firstly, a certain island modeling is created, which includes the shape, size, and lattice mismatch of the QDs. Secondly, the elastic strain field inside and around the dots is calculated numerically applying the finite element method on linear elasticity theory. Finally, this strain field is used to calculate the diffuse X-ray scattering within the kinematic scattering approach. The shape and size in simulation are refined until the best agreement with experimental data is achieved.

For the first step we found that there is somewhat reduced lattice mismatch of about 2.58% between the QDs and the $\mathrm{In}_{0.48}\mathrm{Ga}_{0.52}\mathrm{P}$ buffer and the simulation can only be fitted to the measurements using this value. The reduced lattice mismatch by about 1% may be explained by intermixing of indium and gallium during growth of InP quantum dots, which is not surprising and has been reported by other groups [71]. The measured average mismatch corresponds to $\mathrm{In}_{0.83}\mathrm{Ga}_{0.17}\mathrm{P}$ QDs. Our value of 2.58% is the average lattice mismatch; however, a gradient of the chemical composition inside the QDs is not excluded; but the quantum dots used for the simulation are modeled as having a homogeneous chemical composition.

The shape of quantum dot used for the simulation is a truncated pyramid with shallow faces and rectangular base, which is known from TEM studies. The remaining free parameters of the simulations are the respective QD base

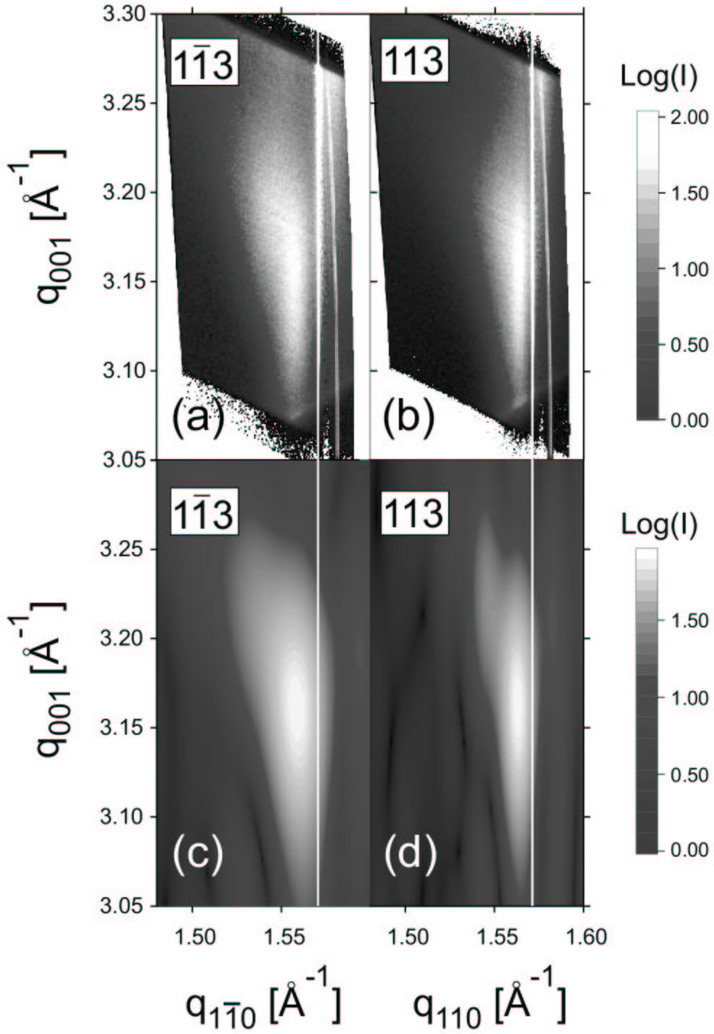

Figure 7.9: X-ray diffuse scattering of uncapped InP quantum dots near the $1\bar{1}3$ and 113 reciprocal lattice points ((a) and (b)) and respective simulations ((c) and (d)). The deposited InP material is 5 ML. Highest intensity is indicated by white, lowest intensity by black (logarithmic scale). The $\mathrm{In}_{0.48}\mathrm{Ga}_{0.52}\mathrm{P}$ buffer layer and GaAs Bragg peaks are black, located at $q_{001} = 3.335$ Å^{-1} and $q_{110} = q_{1\bar{1}0} = 1.572$ Å^{-1}, as depicted by vertical white lines.

widths $w_{[110]}$ and $w_{[1\bar{1}0]}$ along [110] and [$1\bar{1}0$] direction, and the QD height h. A very good agreement with experimental data is achieved for $w_{[110]}$=50±5 nm, $w_{[1\bar{1}0]}$=30±5 nm, and h=7±1 nm. These resulting values from simulation agree well with AFM data for this sample.

The simulated X-ray diffuse scattering near the $1\bar{1}3$ and 113, and 044 reciprocal lattice points (Fig. 7.9c, Fig. 7.9d and Fig. 7.10c) shows that

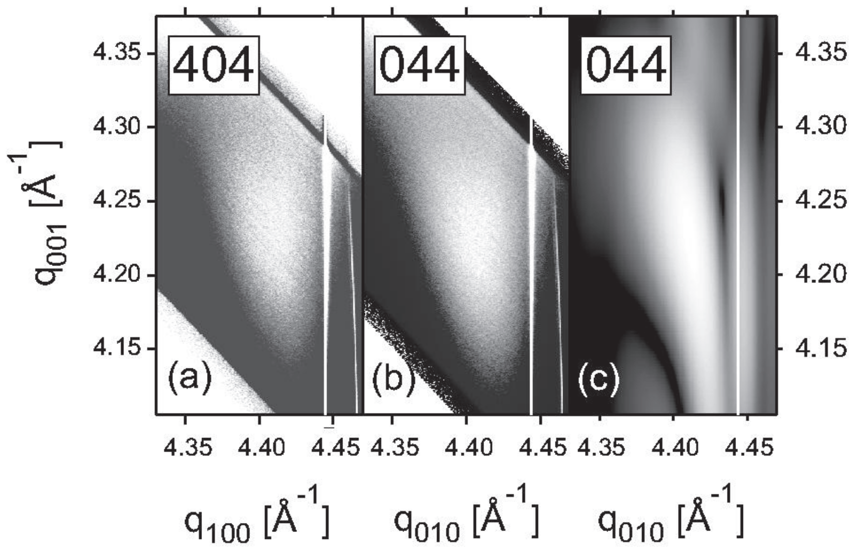

Figure 7.10: Measured X-ray diffuse scattering of uncapped InP quantum dots near the 404 (**a**) and 044 reciprocal lattice points (**b**) and respective simulation (**c**). The deposited InP material is 5 ML. Highest intensity is indicated by black, lowest intensity by white (logarithmic scale). The $In_{0.48}Ga_{0.52}P$ buffer layer and GaAs Bragg peaks are located at $q_{001} = 4.445 Å^{-1}$ and $q_{100} = q_{010} = 4.445 Å^{-1}$ as depicted by vertical white lines.

- the simulations reproduce the overall shape of experimental diffuse intensity patterns, indicating that the calculated elastic strain field fits to the real one,
- the absolute positions of maxima in the diffuse intensity distribution in reciprocal space are identical for experiment and simulation (considering the given error bars),
- the experimentally determined and simulated values of the mean degree of asymmetry

  $$\langle\alpha\rangle = \frac{\langle\varepsilon_{1\bar{1}0}\rangle}{\langle\varepsilon_{110}\rangle} \tag{7.2}$$

  are $\langle\alpha\rangle_{exp} = 1.84 \pm 0.10$ and $\langle\alpha\rangle_{sim} = 1.71 \pm 0.10$, respectively and agree within the estimated uncertainties.

Because the QD size at fixed shape does not affect the strain distribution, only two of three free parameters $w_{[110]}$, $w_{[1\bar{1}0]}$, and h are independent. The geometric aspect ratios

$$Q_1 = \frac{\langle w_{110} \rangle}{2h} \text{ and } Q_2 = \frac{\langle w_{1\bar{1}0} \rangle}{2h} \tag{7.3}$$

associate the width w and height h of quantum dot. When the QD height at fixed base width ($w_{[110]}$, and $w_{[1\bar{1}0]}$) increases, the strain inside the dot may relax more efficiently, which is demonstrated in Figure 7.11; here, the mean total strain components $\langle \varepsilon_{110} \rangle$ and $\langle \varepsilon_{1\bar{1}0} \rangle$ were evaluated from the peak position in simulated X-ray diffuse scattering maps and are plotted as functions of the dot height h. However, at fixed QD height, $\langle \varepsilon_{110} \rangle$ and $\langle \varepsilon_{1\bar{1}0} \rangle$ inversely scale with the QD base widths $w_{[110]}$ and $w_{[1\bar{1}0]}$, respectively. Consequently, the mean degree of asymmetry $\langle \alpha \rangle$ varies linearly with the lateral aspect ratio Q_1/Q_2 (Fig. 7.11b). This scaling behavior facilitates the refinement of the simulation.

The linear scaling behavior of $\langle \varepsilon \rangle$ can be demonstrated by finite element calculations. First, we consider a pyramid-shape QD with $w_{[110]}$=50 nm, $w_{[1\bar{1}0]}$=30 nm, and h=7 nm. Figure 7.12 shows the calculated $\langle \varepsilon_{110} \rangle$ and $\langle \varepsilon_{1\bar{1}0} \rangle$ in respective $(1\bar{1}0)$ and (110) planes through the symmetry axis of the pyramid. The calculation proves again that $\langle \varepsilon_{110} \rangle$ and $\langle \varepsilon_{1\bar{1}0} \rangle$ are different inside the quantum dot and also for the underlying $\mathrm{In}_{0.48}\mathrm{Ga}_{0.52}\mathrm{P}$ buffer; furthermore, within the dot the mean total strain components monotonically increase when we go away from the wetting layer. This means that areas inside the dot close to z=0 (uppermost layer of the wetting layer or bottom of dot) are strongly stressed and not able to relax horizontally. Only with increasing z elastic relaxation may take place to some extend. This behavior is better to be seen in the selected line scans for $\langle \varepsilon_{110} \rangle (z)$, $\langle \varepsilon_{1\bar{1}0} \rangle (z)$, and $\alpha(z) = \varepsilon_{1\bar{1}0}(z)/\varepsilon_{110}(z)$, which are illustrated in Figure 7.13. Note that the dot is nowhere totally relaxed and ε_{110}, and $\varepsilon_{1\bar{1}0}$ are always smaller than the average lattice mismatch between the dot and buffer of about 2.58%. Hence, the ratio $\alpha(z)$ is nearly constant for QD height up to about 10 nm and it is estimated as $\alpha(z) \approx 1.5$. This is the reason why we obtain the linear scaling law for the mean total strains (see Fig. 7.12).

At sufficiently large QD height, however, there is a different case, which is illustrated in Figure 7.13b. In this plot, the line scan is for a pyramid having the same base widths as we had above ($w_{[110]}$=50 nm, $w_{[1\bar{1}0]}$=30 nm), but with a larger height of h=15 nm. In this case, both ε_{110} and $\varepsilon_{1\bar{1}0}$ are converting at the top of the pyramid. Consequently, $\alpha(z)$ is locally varying inside the dot. This can also be seen in Figure 7.12a for a 15 nm high QD, where the mean

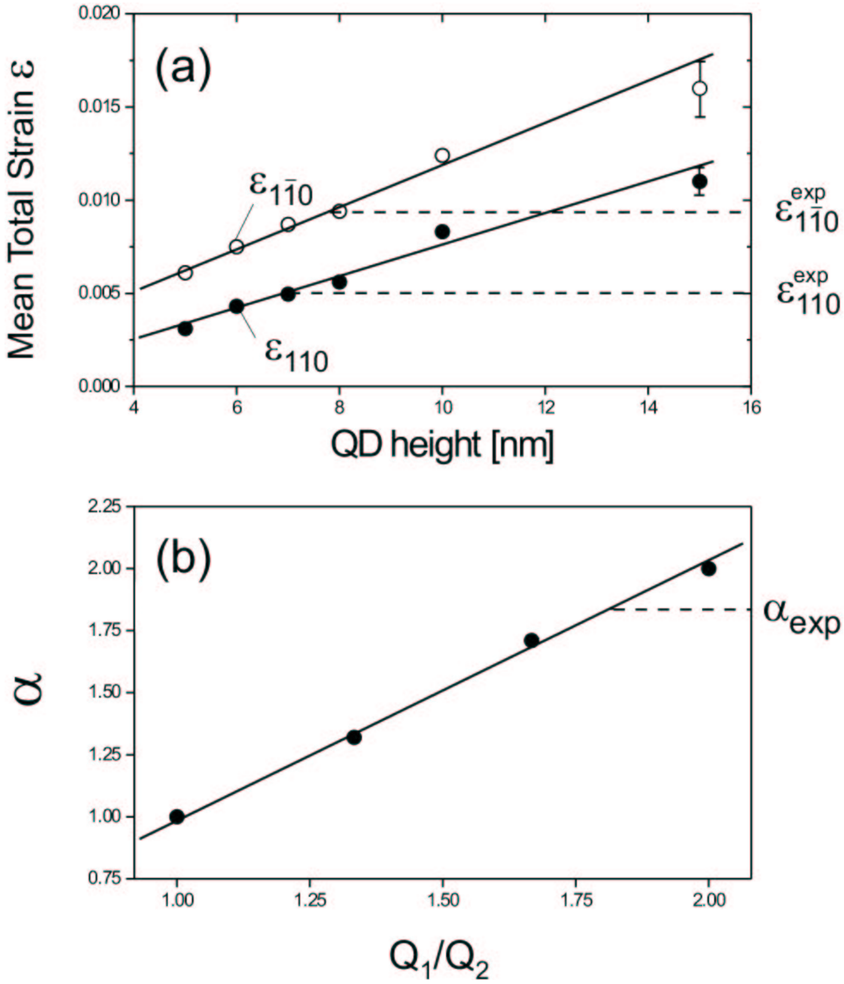

Figure 7.11: **(a)** Mean total strain as a function of the dot height for uncapped QDs along [110] (solid circles) and [$1\bar{1}0$] (open circles) obtained from calculated scattering maps in Fig. 7.9. **(b)** Calculated mean asymmetry ratio $\langle\alpha\rangle$ as a function of the lateral aspect ratio Q_1/Q_2. The dashed lines depict the respective experimental values obtained again from Fig. 7.9. Solid lines are a guide to the eye.

total strain components show deviations from the linear scaling law.

Pay attention to the fact that the *calculated* diffuse scattering in Figure 7.9 and Figure 7.10 shows "fringes" (intensity oscillations) due to pronounced shape-induced diffuse scattering. On the other hand, as expected, for *measured* diffuse scattering the real size distribution of QDs destroys the "fringes". As mentioned before, however, the strain field scales solely with geometric aspect ratios Q_1 and Q_2. Hence, a possible QD size distribution does not change

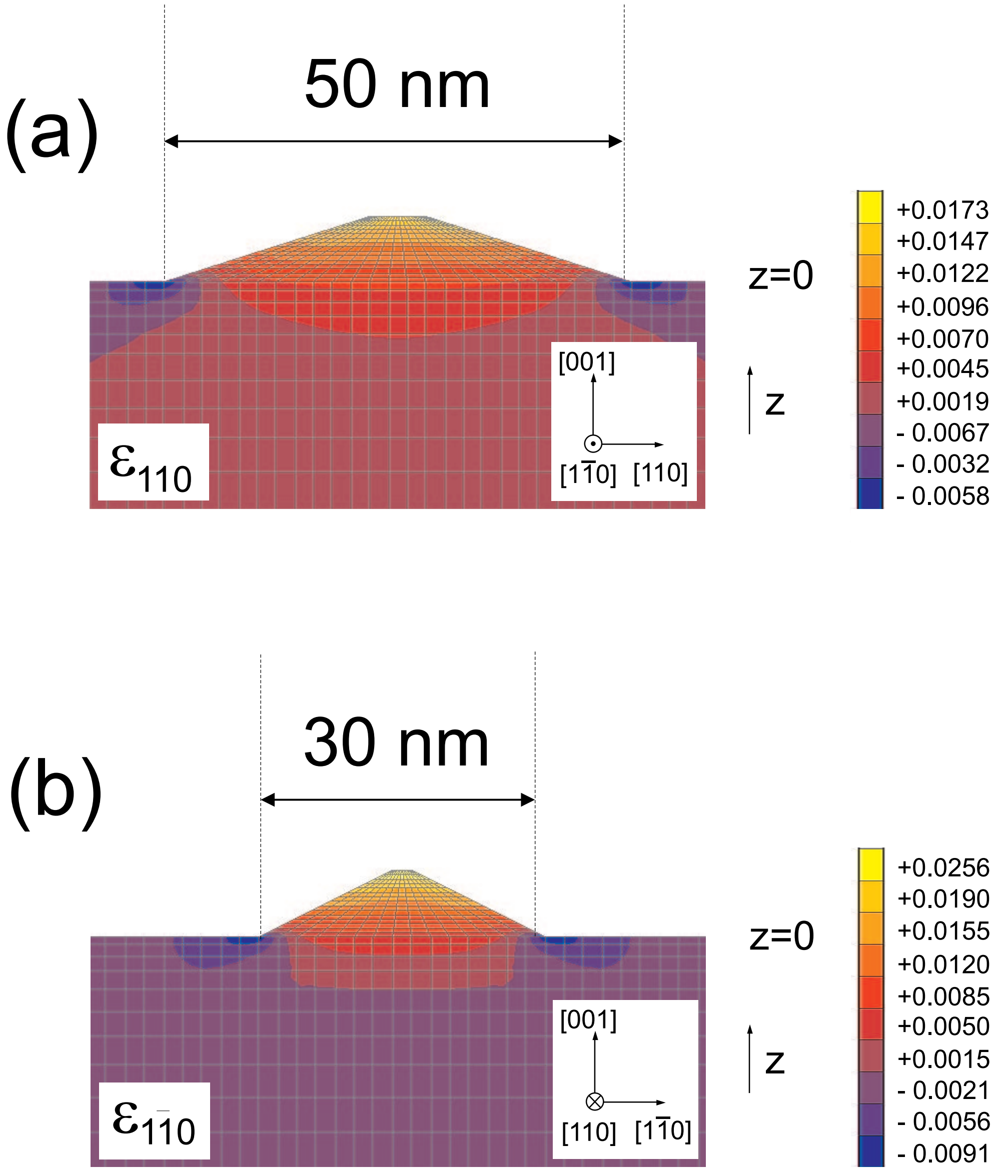

Figure 7.12: Calculated strain tensor components **(a)** ε_{110} in $(1\bar{1}0)$ plane and **(b)** $\varepsilon_{1\bar{1}0}$ in (110) plane, through the symmetry axis of a strained InP pyramidal island ($w_1 = 50$, $w_2 = 30$, and h=7 nm) on a $In_{0.48}Ga_{0.52}P$ buffer.

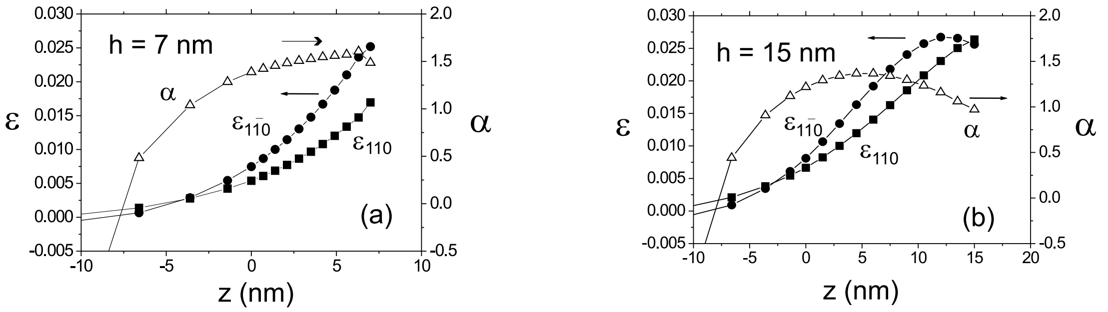

Figure 7.13: **(a)** Selected line scans through symmetry axis of the pyramidal island in Fig. 7.12 for $\varepsilon_{110}(z)$ (solid squares), $\varepsilon_{1\bar{1}0}(z)$ (solid circles), and $\alpha(z) = \varepsilon_{1\bar{1}0}/\varepsilon_{110}$ (open triangles). **(b)** Respective line scans through a pyramidal island having w_1=50 nm, w_2=30 nm, and h=15 nm.

the distribution of strain that induced X-ray diffuse scattering pattern in reciprocal space as long as the dot shape remaining the same. The good agreement between experiment and simulation is, therefore, indicative of a rather uniform shape of the QDs.

To conclude, the evaluated geometric aspect ratios for a modeled facetted pyramid dot with rectangular base are $Q_1 = 3.57$ and $Q_2 = 2.14$ and correspond to QD side faces that are tilted by 15.6° and 25.0° with respect to the (001) surface. Hence, the side faces are close to (115) (tilt of 15.8°) and (113) (tilt of 25.2°) facets.

7.3 Vertical ordering

The common belief is that when an array of coherently strained dots is capped, it creates a strain field in the surrounding matrix [212]. This strain field affects the nucleation of QDs in the next stacked array of dots. It may be figured as providing a template for dot alignment in that array. Therefore, the vertical stacking of many layers of QDs enhances the lateral and vertical ordering.

The vertical ordering of InP quantum dots in the stacked structures is investigated using cross-section transmission electron microscopy together with grazing incidence X-ray diffraction (GID). Because the GID measurements are performed at $\alpha_i = \alpha_f = a_c$ (see Chapter 4), mainly the strain field of the $In_{0.48}Ga_{0.52}P$ cap layer near the surface is probed. Obviously, the strain caused by the InP QDs penetrates through the upper $In_{0.48}Ga_{0.52}P$ layer to the next interface where it may create nucleation centers for the following layer of InP

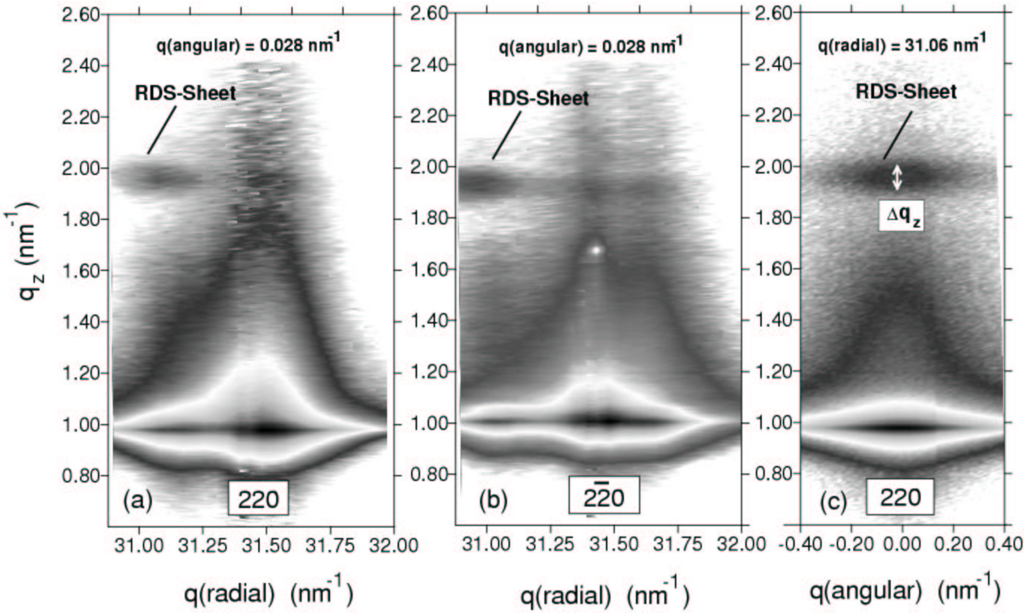

Figure 7.14: GID out-of plane intensity distribution of a sample containing 10 periods InP/$In_{0.48}Ga_{0.52}P$ QD superlattice along angular and radial directions, respectively. The resonant diffuse scattering (RDS) sheet at ($q_z = 2$ nm^{-1}) is due to the first multilayer satellite.

QDs. Hence, in the above way, vertical spatial correlation of the InP QDs layers can be studied.

Figure 7.14 depicts vertical cuts of a superlattice sample (the sample was described in Section 7.2.2). As can be clearly seen, the diffuse scattering pattern is concentrated in a resonant diffuse scattering sheet (RDS sheet) around the first multilayer satellite ($q_z = 1.95$ nm^{-1}), proving strong vertical correlation of the QD layers. Evaluation of the vertical width, δq_z, results in a vertical correlation length of about ξ=60 nm which is comparable with the total multilayer thickness of 65 nm.

The RDS sheet is symmetrical with respect to $q_{angular}$ (Fig. 7.14c), but is shifted towards lower values of q_{radial} (Fig. 7.14a,b). We, thus, probe areas inside the multilayer that exhibit horizontal dilatation (total strain). Finite element calculations show that these areas are basically located **(1)** inside the QD itself, and **(2)** in the $In_{0.48}Ga_{0.52}P$ matrix above and below the QD, whereas compressed areas are located close to the QD edges. As can be seen in Figure 7.14a and Figure 7.14b, lattice dilatation is less pronounced along [220] compared to [2$\bar{2}$0]. The mean total strain in these two directions can be calcu-

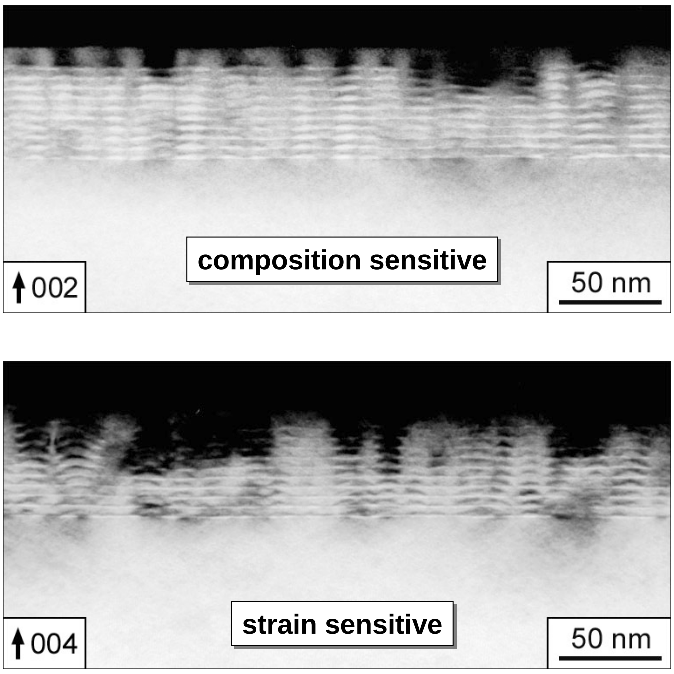

Figure 7.15: Dark-field cross sectional TEM images of InP/$In_{0.48}Ga_{0.52}P$ QD superlattice measured under two different beam conditions: Composition sensitive and strain sensitive (see Sec. 5.3.2).

lated from the shift δq_R of the RDS sheet with respect to the crystal truncation rod at $q_{radial} = 31.44$ nm^{-1}. We obtain the following mean total strain values: $< \varepsilon_{110} > = 0.013 \pm 0.002$ and $< \varepsilon_{1\bar{1}0} > = 0.016 \pm 0.002$, respectively. This distinct difference of mean total strain is explained with different QD elongation along [110] and [1$\bar{1}$0] and our results imply an elongated QD along [110]. This is in agreement with the GISAXS intensity distribution and X-ray diffuse scattering.

Furthermore, the cross-section TEM micrographs indicate a strong vertical correlation between stacked QDs. Figure 7.15 shows the cross sectional TEM from the same sample.

7.4 Conclusion

Our results show strong lateral ordering of the QDs along the four ⟨100⟩ directions as well as vertical correlation of the dot positions through the entire multilayer stack. The data indicate that the degree of planar ordering rises with increasing InP deposition time and, therefore, with increasing quantum

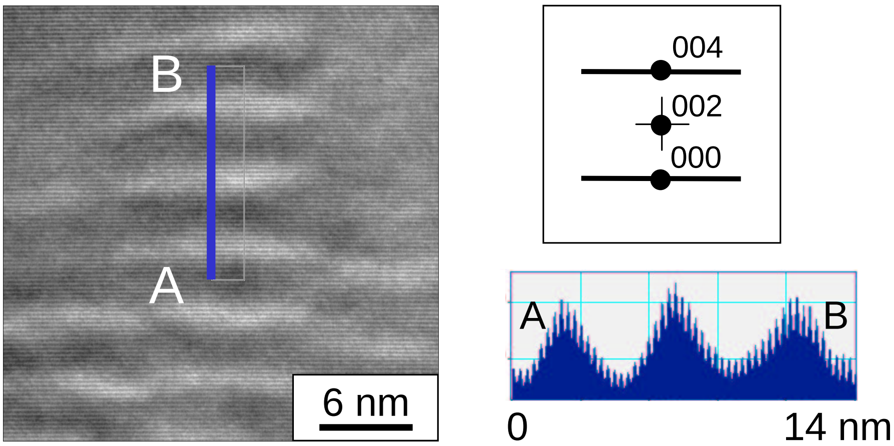

Figure 7.16: High-resolution TEM image of stacked InP QDs (bright) embedded in $In_{0.48}Ga_{0.52}P$ matrix (dark). The dots are well correlated. The small plot on the right indicates the line scan of brightness value from A to B in TEM image; the beam condition is depicted on top of that (Bragg condition).

dot density. This enhancement in ordering is seen both in that the dot period is less variable and in the appearance of longer-ranged ordering of the dots on the surface. Both ordering of position, as seen in the AFM power spectra, and the ordering of dot size and shape seen in the GISAXS and GID contribute to the degree of total ordering. These effects can be investigated independently of each other by studying the differences between the AFM power spectra and GISAXS.

In addition, GISAXS and GID show a distinct asymmetry of diffuse scattering with respect to the [110] and $[1\bar{1}0]$ directions. This behavior is interpreted as QD elongation along [110].

Furthermore, the correlation between stacked InP QDs has been proved using GID and cross-section TEM studies.

Chapter 8

Thermal annealing of InP quantum dots

8.1 Introduction

The control of the density, size and shape and consequently, of the optical properties of quantum dots is not limited to epitaxy alone by a careful choice of growth parameters, but can also be done using post-growth methods. Rapid thermal annealing (RTA) has proved to be an effective way to change the properties of dots. Several groups have shown that RTA results in a blueshift of the interband transition energy in quantum dots. Moreover, a decrease in the interlevel spacing and a narrowing of the photoluminescence line have been reported [213, 214, 215, 216, 217].

This chapter presents our results from photoluminescence studies of annealed InP/$In_{0.48}Ga_{0.52}P$ and InP/GaP quantum dots.

8.2 Experimental details

The process of rapid thermal annealing was done using a STEAG SHS100 reactor unit. The system was heated by tungsten halogen lamps; pyrometers were used for temperature measurement. The temperature was increased with a constant ramp of 15 K/s. The annealing temperature was kept constant for the anneal time t_A. For more information on the equipment refer to [218].

PL measurements were carried out at 5 K using the 325 nm line of a He-Cd laser; the emission was dispersed in a 1 m monochromator and was detected by a charge-coupled device camera. All measurements were done with an excitation density of 20 W/cm^2.

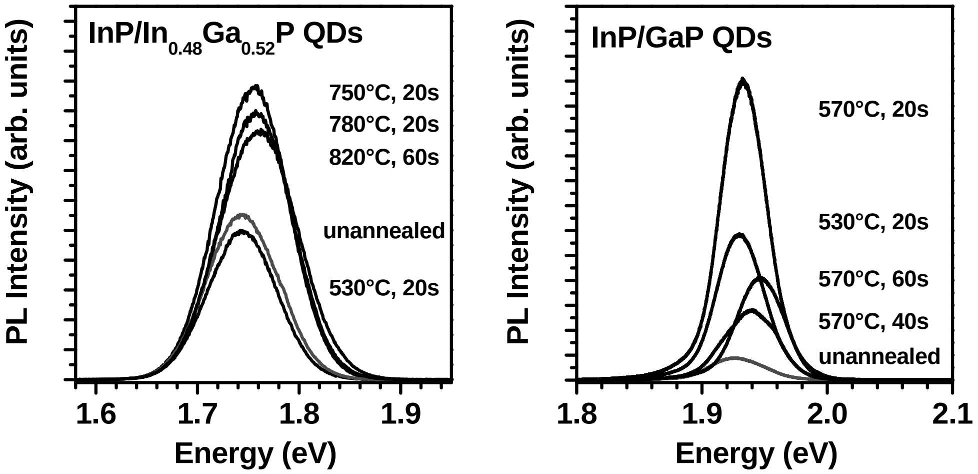

Figure 8.1: PL spectra of annealed QD samples. InP coverage was 4.5 ML and 2.1 ML for InP/$In_{0.48}Ga_{0.52}P$ and InP/GaP samples, respectively. The corresponding applied temperature and the duration of annealing are exhibited on the right. For comparison, the spectra from unannealed (as grown) samples are shown.

8.3 Results and Discussion

Figure 8.1 shows the PL spectra of unannealed and annealed samples containing InP QDs. Photoluminescence from annealed InP dots in both material systems, i.e. InP/$In_{0.48}Ga_{0.52}P$ and InP/GaP, is blueshifted; furthermore, annealing can result in an increase in PL intensity. The obtained data are compiled in Table 8.1.

system	**T_{max}**	**t_A (s)**	**ΔE (meV)**	**I_{an}/I_{un}**
InP/$In_{0.48}Ga_{0.52}P$	750°C	20	4	1.9
	780°C	20	9	1.8
	820°C	60	14	1.7
InP/GaP	530°C	20	4	7
	570°C	20	6	15
	570°C	40	14	3.5
	570°C	60	21	5

Table 8.1: Temperature and time of annealing for several InP samples along with the results from PL measurements: Value of PL blueshift ΔE compared to the unannealed sample and the ratio of integral PL intensity I_{an}/I_{un} between annealed and unannealed samples.

From studies on InAs/GaAs QDs it is known that the anneals induce indium-gallium interdiffusion within each quantum dot, causing changes in size, shape, and composition. Hence, new optical properties [213, 214, 215]. To explore the interdiffusion effects in InP QDs, we have applied a model that is based on the following assumptions: Initially we consider the QDs to have a rectangular band alignment for electrons and holes. This band alignment is then altered by an interdiffusion of gallium into the InP dots during the annealing process. As a consequence, the interface is smeared out, resulting in a higher ground state energy for both electrons and holes and, hence, in a blueshift in the PL spectrum [218]. For quantitative analysis one has to solve Fick's diffusion equation

$$\frac{\partial}{\partial t}C(x,t) = D\frac{\partial^2}{\partial x^2}C(x,t) \tag{8.1}$$

with given initial values and boundary conditions. $C(x,t)$ represents the gallium content. Assuming a constant Ga reservoir at the edge of the barrier $C_S = 0.5$ and a Ga content that vanishes deep in the barrier, Fick's diffusion equation is solved through

$$C(x,t) = C_S\ (1 - \mathrm{erf}(\frac{x}{x_D})) \tag{8.2}$$

$x_D = 2\sqrt{Dt_A}$ is the diffusion length, t_A is the anneal time; erf is the error function. D stands for the temperature dependent diffusion coefficient:

$$D(T) = D_0\ exp\left(\frac{-E_a}{k_B T}\right) \tag{8.3}$$

E_a is the activation energy; D_0 represents the pre-factor.

With this information we can first analyze the energy shift as a function of the diffusion length by using a numerical simulation, the so called shooting method, and after that we can determine the activation energy and pre-factor by fitting our data to the numerical analysis. Figure 8.2 shows the energy shift as function of the diffusion length for both InP/$\mathrm{In_{0.48}Ga_{0.52}P}$ QDs and InP/GaP QDs. The best fits are obtained using activation energy E_a of 3.1 and 0.64 eV, and pre-factor D_0 of 1.8×10^{11} and 84 $\mathrm{nm^2/s}$ for InP/$\mathrm{In_{0.48}Ga_{0.52}P}$ and InP/GaP, respectively [218].

The published activation energies in III-V heterostructures vary from 0.32 eV [219] to 7.43 eV [220]. This broad range is due to various diffusion mechanisms for the interdiffusion process. In case of the InP/$\mathrm{In_{0.48}Ga_{0.52}P}$ the creation of vacancies and the diffusion of vacancies are the origin of activation

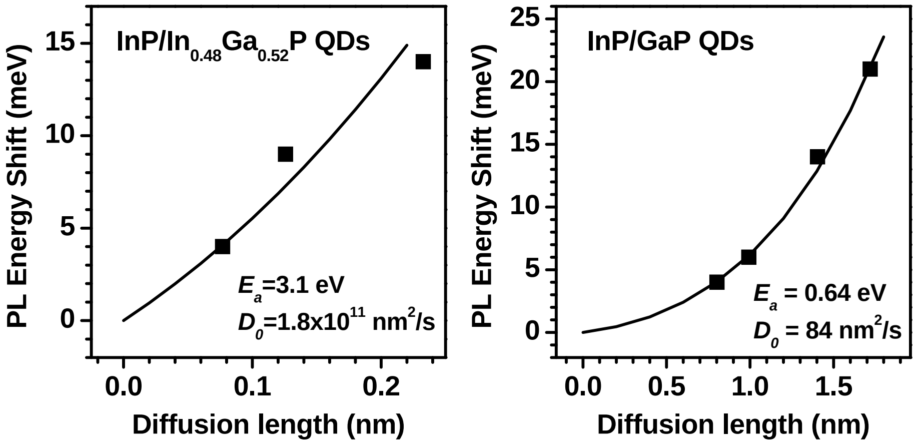

Figure 8.2: Numerical simulation (solid line) and experimental data (solid squares) for InP/$In_{0.48}Ga_{0.52}P$ and InP/GaP QDs. The used parameters for simulation are also shown.

energy. The obtained value for InP/$In_{0.48}Ga_{0.52}P$ QDs is in good agreement with the activation energy of 3.2 ± 0.2 eV in InP-GaP bulk material [221] due to indium and gallium interdiffusion. The obtained activation energy for InP/GaP, on the other hand, is significantly lower than that from other systems [219, 220, 221, 222]. This low activation energy can be explained by an excess of vacancies in such a way that the concentration of vacancies is higher than that in the thermal equilibrium. Consequently, diffusion of vacancies is the main origin of the obtained activation energy. Since vacancies could be nonradiative recombination centers, their diffusion due to thermal annealing can result also in a higher PL intensity. Furthermore, an excess of vacancies in InP/GaP QDs as compared to InP/$In_{0.48}Ga_{0.52}P$ QDs can explain the higher increase in PL intensity in the former system.

The nine orders of magnitude difference between the pre-factors of InP/ $In_{0.48}Ga_{0.52}P$ and InP/GaP is also remarkable. One possible reason for this may be the use of different substrates (GaAs and GaP). The effect of substrate material on the pre-factor has already been observed [223, 224, 225]. In addition to that, several groups demonstrated that annealing in a gallium rich environment results in a lower pre-factor than for an As rich environment [226, 227, 228, 229]. So, once more because of the different substrates, it is possible here that the InP/$In_{0.48}Ga_{0.52}P$ samples on GaAs were annealed in a more As rich environment as compared to the InP/GaP samples on GaP.

A change of dot shape and size may also lead to a shift of the PL peak as well as to an increase in PL intensity. To study that, we investigated the samples using transmission electron microscopy. Our studies reveal that, as with other semiconductors, the annealing process mended the defects in our samples, which may result in higher PL intensity. In the case of InP/$In_{0.48}Ga_{0.52}P$ QDs we observed a slight change of dot shape; the annealed dots are more asymmetric (about 10%) (see also Sec. 7.2.3). Whether this slight change can explain the energy shift is not clear and to clarify that, it is necessary to calculate the electronic structure of QDs using a model that includes the dot geometry. In the case of InP/GaP QDs, however, we observed an increase in dot density by factor ten from 10^8 to 10^9 dots/cm^2; this higher dot density can result in higher PL intensity. In contrast, the size of dots is not changed. Since the cross-sectional TEM studies do not indicate any material migration from wetting layer into dots, the reason for the higher dot density in annealed samples is not clear. The diffusion of indium from the matrix into the dots can be a possible reason for that. Although, it should be noted once more that the analysis of TEM data is not straightforward because of the poor statistical information and the limitations of this method (see also Sec. 4.2.8).

8.4 Conclusion

The effect of rapid thermal annealing on optical properties of InP quantum dots has been demonstrated. The PL spectra of annealed QDs in both $In_{0.48}Ga_{0.52}P$ and GaP matrix show a greater intensity as well as a blueshift. We attribute the blueshift to an interdiffusion of Ga from the matrix into the QDs. Our numerical simulation, using Fick's diffusion equation, results in an activation energy of 3.1 eV and 0.64 eV for the InP/$In_{0.48}Ga_{0.52}P$ and the InP/GaP system, respectively. The distinction in the activation energies can be explained with different diffusion processes for the two systems. In the InP/$In_{0.48}Ga_{0.52}P$ system this process is governed by thermal creation and diffusion of vacancies, whereas for the InP/GaP system it is mainly ruled by vacancy diffusion alone.

Chapter 9

Summary and outlook

In this work the growth of self-assembled InP quantum dots, as well as their optical properties and associated carrier dynamics are presented and discussed. The QDs were grown in and on the two materials $\mathrm{In_{0.48}Ga_{0.52}P}$ (lattice matched to GaAs) and GaP.

Under the proper growth conditions, formation of InP dots via the Stranski-Krastanow mechanism was observed. The critical InP coverage for 2D-3D transition was found to be 3 ML for the InP/$\mathrm{In_{0.48}Ga_{0.52}P}$ system and 1.8 ML for the InP/GaP system. It was found from the structural characterization that the InP/GaP QDs are larger and, consequently, less dense compared to the InP/$\mathrm{In_{0.48}Ga_{0.52}P}$ QDs; hence, InP dots on GaP tend to be strain-relaxed.

Intense photoluminescence from InP quantum dots in both material systems was observed. The PL from InP/GaP QDs peaks between 1.9 and 2 eV and is by about 200 meV higher in energy than the PL line from InP/$\mathrm{In_{0.48}Ga_{0.52}P}$ QDs mainly due to the bandgap difference between both matrix materials (see Fig. 9.1). The optical emission from dots is attributed to direct transitions between the electrons and heavy-holes confined in the InP dots, whereas the photoluminescence from a two-dimensional InP layer embedded in GaP is explained as resulting from the spatially indirect recombination of electrons from the GaP X valleys with holes in InP and their phonon replicas. The type-II band alignment of InP/GaP two-dimensional structures was further confirmed by the carrier lifetime above 19 ns, which is much higher than in type-I systems. The band alignment modeling for dots was supported by the observed carrier lifetime of 100–500 ps for InP/$\mathrm{In_{0.48}Ga_{0.52}P}$ QDs and 2 ns for InP/GaP QDs. Further evidence for a type-I band alignment for InP/GaP QDs is given by the results from pressure-dependent PL measurements.

The InP/$\mathrm{In_{0.48}Ga_{0.52}P}$ QDs tend to form ordered arrays when InP coverage

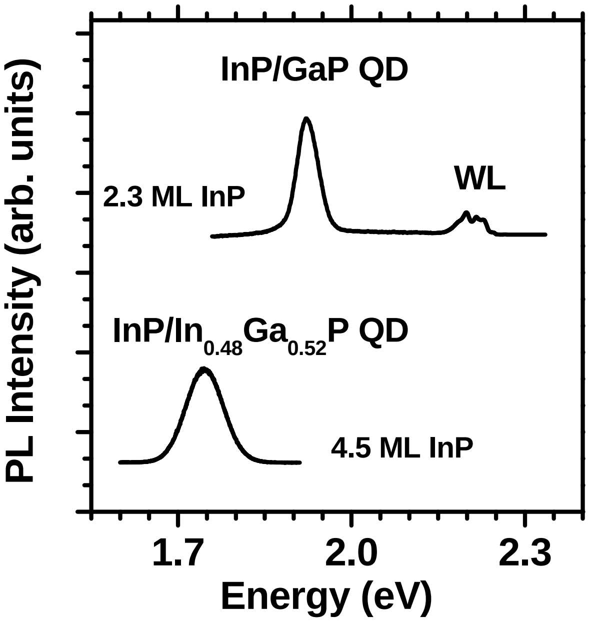

Figure 9.1: PL spectra of InP/In$_{0.48}$Ga$_{0.52}$P and InP/GaP QDs.

is increased. Coherent, ordered arrays of uniform quantum dots are advantageous for QD-based optoelectronic devices. Furthermore, the InP quantum dots in both systems show a more intense photoluminescence signal after rapid thermal annealing.

Altogether, InP QDs are an attractive system for optical application. The optical gain and lasing in InP/In$_{0.48}$Ga$_{0.52}$P QDs has been demonstrated by Moritz et al.; the vertical-cavity surface-emitting laser based on InP/In$_{0.48}$Ga$_{0.52}$P QDs has recently been fabricated [230,231]. Ryou et al. succeeded in fabricating photopumped red-emitting laser using aluminum in the matrix (In$_{0.5}$Al$_{0.3}$Ga$_{0.2}$P) [232]. All of these structures were grown on GaAs substrate. The use of GaP as the substrate, however, could take advantage of a well-developed light-emitting diode technology [233]. Additionally, using the transparent GaP rather than GaAs allows easier extraction of the emitted light for vertical structures such as vertical-cavity lasers. This work has demonstrated that InP QDs embedded in indirect GaP matrix are promising for application as a light emitter with higher efficiency than the currently-used systems.

Bibliography

[1] Y. Arakawa and H. Sakaki. Multidimensional quantum well laser and dependence of its threshold current. *Appl. Phys. Lett.*, 40(11):939–941, 1982.

[2] J.M. Moison, F. Houzay, F. Barthe, L. Leprince, E. Andr, and O. Vatel. Self-organized growth of regular nanometer-scale InAs dots on GaAs. *Appl. Phys. Lett.*, 64(2):196–198, 1994.

[3] D. Leonard, M. Krishnamurthy, C.M. Reaves, S.P. Denbaares, and P.M. Petroff. Direct formation of quantum-sized dots from uniform coherent islands of InGaAs on GaAs surfaces. *Appl. Phys. Lett.*, 63(23):3203–3205, 1994.

[4] D.L. Huffaker, G. Park, Z. Zou, O.B. Shchekin, and D.G. Deppe. Direct formation of quantum-sized dots from uniform coherent islands of InGaAs on GaAs surfaces. *Appl. Phys. Lett.*, 73(18):2564–2566, 1998.

[5] G. Park, O.B. Shchekin, S. Csutak, D.L. Huffaker, and D.G. Deppe. Room-temperature continuous-wave operation of a single-layered 1.3 μm quantum dot laser. *Appl. Phys. Lett.*, 75(21):3267–3269, 1999.

[6] F. Capasso and G. Margaritondo, editors. *Heterojunction Band Discontinuities: Physics and Device Applications.* Elsevier Science Publishers B.V., Amsterdam, 1987.

[7] C. Van de Walle. Band lineups and deformation potentials in the model-solid theory. *Phys. Rev. B*, 39(3):1871–1883, 1989.

[8] J.R. Chelikowsky and M.L. Cohen. Nonlocal pseudopotential calculations for the electronic structure of eleven diamond and zinc-blende semiconductors. *Phys. Rev. B*, 14(2):556–582, 1976.

[9] S.C. Jain, M. Willander, and H. Maes. Stresses and strains in epilayers, stripes and quantum structures of III-V compound semiconductors. *Semicond. Sci. Technol.*, 11(5):641–671, 1996.

[10] A.S. Saada. *Elasticity: Theory and Application.* Robert E. Krieger Publishing Co., Florida, 1989.

[11] S. Adachi. Material parameter of InGaAsP and related binaries. *J. Appl. Phys.*, 53(12):8775–8792, 1982.

[12] L. Banyai, Y.Z. Hu, M. Lindberg, and S.W. Koch. Third-order optical non-linearities in semiconductor microstructures. *Phys. Rev. B*, 38(12):8142–8153, 1988.

[13] L.L. Chang and K. Ploog, editors. *Molecular Beam Epitaxy and Heterostructures.* Nato ASI. Martinus Nijhoff Publishers, Boston, 1985.

[14] M.A. Herman and H. Sitter. *Molecular Beam Epitaxy.* Springer-Verlag, Berlin, 1989.

[15] M.B. Panish. Molecular beam epitaxy of GaAs and InP gas source for As and P. *J. Electrochem. Soc.*, 127:2729, 1980.

[16] M.B. Panish and S. Sumski. Gas source molecular beam epitaxy of $Ga_xIn_{1-x}P_yAs_{1-y}$. *J. Appl. Phys.*, 55(10):3571–3576, 1984.

[17] W.T. Tsang. Chemical beam epitaxy of InP and GaAs. *Appl. Phys. Lett.*, 45(11):1234–1236, 1984.

[18] A.S. Jordan and A. Robertson. Equilibrium gas-phase composition and thermodynamic properties including subhydirids in the pyrolysis of AsH_3 and PH_3. *J. Crystal Growth*, 128(1–4):488–493, 1993.

[19] M.B. Panish and H. Temkin. *Gas Source Molecular Beam Epitaxy: Growth and Properties of Phosphorus Containing III-V Heterostructures.* Springer-Verlag, Berlin, 1993.

[20] Y.-C. Cheng, S. Chi, S.-T. Chou, and K.-F. Huang. Temperature and annealing effects on photoluminescence spectra of $(InAs)_1/(GaP)_2$ superlattices grown by solid-source molecular beam epitaxy. *Jpn. J. Appl. Phys.*, 39, Part2(10A):L968–L971, 2000.

[21] D. Palloks. Wachstum und Untersuchungen von GaAs-basierten InAs- und InAs/GaAs-Systemen hinsichtlich ihrer Anwendbarkeit als MWIR-Diodendetektoren. Master's thesis, Institut für Physik, Humboldt-Universität zu Berlin, 1998.

[22] Eurotherm Regler GmbH. *Universalregler/programmregler serie 902–904*, 1996.

[23] E.J. Heller and M.G. Lagally. In situ scanning tunneling microscopy observation of surface morphology of GaAs(001) grown by molecular beam epitaxy. *Appl. Phys. Lett.*, 60(21):2675–2677, 1992.

[24] H. Lüth. *Surfaces and interfaces of solid materials.* Springer-Verlag, Berlin, 1998.

[25] F.C. Frank and J.H. van der Merwe. In *Proc. Roy. Soc. Lond. A*, volume 198, page 205, 1949.

[26] M. Volmer and A. Weber. *Zeit. Phys. Chem.*, 119:277, 1926.

[27] I.N. Stranski and L. Krastanow. In *Sitzungsberichte d. Akad. d. Wissenschaften in Wien, Abt. IIb, Band 146*, page 797. 1937.

[28] E. Bauer. Phänomenologische Theorie der Kristallabscheidung an Oberflächen. *Zeit. Kristallog.*, 110:372–394, 1958.

[29] E. Bauer and H. Popper. Recent advances in epitaxy. *Thin Solid Films*, 12(1):167–185, 1972.

[30] C. Ratsch and A. Zangwill. Equilibrium theory of the Stranski-Krastanov epitaxial morphology. *Surf. Sci.*, 293:123–131, 1993.

[31] V.A. Shchukin, N.N. Ledentsov, P.S. Kop'ev, and D. Bimberg. Spontaneous ordering of arrays of coherent strained island. *Phys. Rev. Lett.*, 75(16):2968–2971, 1995.

[32] I. Daruka and A.-L. Barabasi. Dislocation-free island formation in heteroepitaxial growth: A study at equilibrium. *Phys. Rev. Lett.*, 79(19):3708–3711, 1997.

[33] I. Daruka and A.-L. Barabasi. Equilibrium phase diagrams for dislocation free self-assembled quantum dots. *Appl. Phys. Lett.*, 72(17):2102–2104, 1998.

[34] W. Ostwald. Über die vermeintliche Isometric des roten und gelbem Quacksilberoxyds und die Oberflächenspannung fester Körper. *Zeit. Phys. Chem.*, 34:495–503, 1900.

[35] M. Zinnke-Allmang, L.C. Feldman, and M.H. Grabaw. Clustering on surfaces. *Surf. Sci. Rep.*, 16:377–463, 1929.

[36] D. Vanderbilt and L.K. Wickham. Evolution of thin-film and surface microstructure. In *Proc. Mater. Res. Soc. Symp.*, volume 202, page 505, 1991.

[37] B.J. Spencer and J. Tersoff. Dislocation energetics in epitaxial strained islands. *Appl. Phys. Lett.*, 77(16):2533–2535, 2000.

[38] J. Tersoff and R.M. Tromp. Shape transition in growth of strained islands: spontaneous formation of quntum wires. *Phys. Rev. Lett.*, 70(18):2782–2785, 1993.

[39] E. Pehlke, N. Moll, A. Kley, and M. Scheffler. Shape and stability of quantum dots. *Appl. Phys. A*, 65:525–534, 1997.

[40] D. Bimberg, M. Grundmann, and N.N. Ledentsov. *Quantum Dot Heterostructures.* J. Willy & Sons, Chichester, 1999.

[41] P.D. Wang, N.N. Ledentsov, C.M. Sotomayor Torres, P.S. Kop'ev, and V.M. Ustinov. Optical characterization of submonolayer and monolayer InAs structures grown in a GaAs matrix on (100) and high-index surfaces. *Appl. Phys. Lett.*, 64(12):1526–1528, 1994.

[42] K. Suzuki, R.A. Hogg, K. Tachibana, and Y. Arakawa. Density control of GaSb/GaAs self-assembled quantum dots (25nm) grown by molecular beam epitaxy. *Jpn. J. Appl. Phys.*, 37, Part2(2B):L203–L205, 1998.

[43] R. Leon, C. Lobo, A. Clark, R. Bozek, A. Wysmolek, A. Kurpiewski, and M. Kaminska. Different paths to tunability in III-V quantum dots. *J. Appl. Phys.*, 84(1):248–254, 1998.

[44] J. Johansson, N. Carlsson, and W. Seifert. Manipulations of size and density of self-assembled quantum dots grown by MOVPE. *Physica E*, 2:667–671, 1998.

[45] J. Oshinowo, M. Nishioka, S. Ishida, and Y. Arakawa. Area density control of quantum-size InGaAs/Ga(Al)As dots by metalorganic chemical vapor deposition. *Jpn. J. Appl. Phys.*, 33, Part2(11B):L1634–L1637, 1994.

[46] Q. Xie, N.P. Kobayashi, T.M. Ramachandran, A. Kalburge, P. Chen, and A. Madhukar. Strained coherent InAs quantum box islands on GaAs(100): Size equalization, vertical self-organization and optical properties. *J. Vac. Sci. Technol. B*, 14(3):2203–2207, 1996.

[47] Y. Nabetani, K. Sawada, Y. Furukawa, A. Wakahara, S. Noda, and A. Sasaki. Self-assembled InP islands grown on GaP substrate. *J. Crystal Growth*, 193(4):470–477, 1998.

[48] H. Saito, K. Nishi, and S. Sugou. Shape transition of InAs quantum dots by growth at high temperature. *Appl. Phys. Lett.*, 74(9):1224–1226, 1999.

[49] P. Ballet, J.B. Smathers, H. Yang, C.L. Workman, and G.J. Salamo. Scanning tunneling microscopy investigation of truncated InP/GaInP$_2$ self-assembled islands. *Appl. Phys. Lett.*, 77(21):3406–3408, 2000.

[50] R. Leon, C. Lobo, J. Zou, T. Romeo, and D.J.H. Cockayne. Stable and metastable InGaAs/GaAs island shapes and surfactantlike suppression of the wetting transformation. *Phys. Rev. Lett.*, 81(12):2486–2489, 1998.

[51] N.N. Ledentsov, M. Grundmann, N. Kirstaedter, O. Schmidt, R. Heitz, J. Böhrer, D. Bimberg, V.M. Ustinov, V.A. Shchukin, A.Yu. Egorov, A.E. Zhukov, S. Zaitsev, P.S. Kop'ev, Zh.I. Alferov, S. Ruvimov, P. Werner, U. Gösele, and J. Heydenreich. Ordered arrays of quantum dots: formation, electronic spectra, relaxation phenomena, lasing. *Solid-State Electron.*, 40(1–8):785–798, 1996.

[52] S. Yoon, Y. Moon, T.-W. Lee, H. Hwang, E. Yoon, Y.D. Kim, U.H. Lee, D. Lee, H.-S. Kim, and J.Y. Lee. Effects of growth intrruption on the evolution of InAs/InP self-assembled quantum dots. *J. Elec. Mater.*, 29(5):535–540, 2000.

[53] S. Fuchi, Y. Nonogaki, H. Moriya, Y. Fujiwara, and Y. Takeda. Effects of GaP cap layer growth on self-assembled InAs islands grown on GaP (001) by organometallic vapor phase epitaxy. *Jpn. J. Appl. Phys.*, 39, Part1(6A):3290–3293, 2000.

[54] C. Walther. *Korrelation elektronischer und struktureller Eigenschaften selbstorganisieter InAs-Nanostrukturen der Dimensionen 0 und 1 auf Verbindungshalbleitern.* PhD thesis, Institut für Physik, Humboldt-Universität zu Berlin, 2000.

[55] Y. Nabetani, T. Ishikawa, S. Noda, and A. Sasaki. Initial growth stage and optical properties of a three-dimensional InAs structure on GaAs. *J. Appl. Phys.*, 76(1):347–351, 1994.

[56] Bede Scientific Instrument Ltd., Durham. *Manual and software of RADS: Rocking Curve Analysis by Dynamical Simulation*, 2000.

[57] S. Takagi. Dynamical theory of diffraction applicable to crystals with any kind of small distortion. *Acta Crys.*, 15:1311, 1962.

[58] S. Takagi. *J. Phys. Soc. Japan*, 26:1239, 1969.

[59] D. Taupin. *Bull. Soc. Fr. Mineral. Cristallogr.*, 87:469, 1964.

[60] Bede Scientific Instrument Ltd., Durham. *QC2a Diffractometer: Operation and Reference Manual*, 1996.

[61] A. Guinier and G. Fournet. *Small Angle Scattering of X-Rays.* Wiley, New York, 1955.

[62] G.H. Vineyard. Grazing-incidence diffraction and the distorted-wave approximation for the study of surfaces. *Phys. Rev. B*, 26(8):4146–4159, 1982.

[63] M. Schmidbauer, Th. Wiebach, H. Raidt, M. Hanke, R. Köhler, and H. Wawra. Ordering of self-assembled SiGe islands studied by grazing incidence small-angle x-ray scattering and atomic force microscopy. *Phys. Rev. B*, 58(16):10523–10531, 1998.

[64] Measurements by M. Schmidbauer at HU Berlin.

[65] SEM measurements by S. Rogaschewski at HU Berlin.

[66] V.J. Morris, A.R. Kirby, and A.P. Gunning. *Atomic Force Microscopy for Biologist.* Imperial College Press, London, 1999.

[67] AFM measurements by K. Braune at HU Berlin.

[68] S. Amelinckx, D. van Dyck, J. van Landuyt, and G. van Tendeloo, editors. *Electron Microscopy: Principles and Fundamentals.* VCH, Weinheim, 1997.

[69] N.N. Ledentsov, V.A. Shchukin, M. Grundmann, N. Kirstaedter, J. Böhrer, O. Schmidt, D. Bimberg, V.M. Ustinov, A. Egorov, A. Zhukov, P. Kop'ev, S. Zaitsev, N. Gordeev, Zh.I. Alferov, A. Borovkov, A. Kosogov, S. Ruvimov, P. Werner, U. Gösele, and J. Heydenreich. Direct formation of vertically coupled quantum dots in Stranski-Krastanow growth. *Phys. Rev. B*, 54(12):8743–8750, 1996.

[70] X.Z. Liao, J. Zou, X.F. Duan, D.J.H. Cockayne, R. Leon, and C. Lobo. Transmission-electron microscopy study of the shape of buried InGaAs/GaAs quantum dots. *Phys. Rev. B*, 58(8):R4235–R4237, 1998.

[71] J. Johansson, V. Zwiller, C. Thelander, A. Gustafsson, W. Seifert, L. Samuelson, O. Malm, and L. Falk. Indium enrichment in $Ga_{1-x}In_xP$ self-assembled quantum dots. *J. Appl. Phys.*, 88(11):6378–6381, 2000.

[72] C.R. Brundle, C.A. Evans,Jr., and S. Wilson, editors. *Encyclopedia of Materials Characterization.* Butterworth-Hinemann, Boston, 1992.

[73] TEM measurements by H. Kirmse at HU Berlin.

[74] H. Kirmse. *Transmissionselektronmikroskopische Untersuchungen von II-VI-Verbindungshalbleitern unterschiedlicher Dimensionierung.* PhD thesis, Institut für Physik, Humboldt-Universität zu Berlin, 2000.

[75] S. Perkowitz. *Optical Characterization of Semiconductors: Infrared, Raman and Photoluminescence Spectroscopy.* Academic Press, London, 1993.

[76] C.F. Klingshirn. *Semiconductors Optics.* Springer-Verlag, Berlin, 1995.

[77] Paul-Drude-Institut für Festkörperelektronik, Hausvogteiplatz 5-7, 10117 Berlin, Germany.

[78] Time resolved PL measurements by H.-Y. Hao at Paul-Drude-Institut für Festkörperelektronik, Berlin.

[79] Raman scattering measurements by M. Ramsteiner at Paul-Drude-Institut für Festkörperelektronik, Berlin.

[80] P. Blood and J.W. Orton. *The Electrical Characterization of Semiconductors: Majority Carriers and Electron States.* Academic Press, London, 1992.

[81] J. Ahopelto, A. Atsushi Yamaguchi, K. Nishi, A. Usui, and H. Sakaki. Nanoscale InP islands for quantum box structures by hydride vapor phase epitaxy. *Jpn. J. Appl. Phys.*, 32, Part 2(1A/B):L32–L35, 1993.

[82] N. Carlsson, W. Seifert, A. Petterson, P. Castrillo, M.-E. Pistol, and L. Samuelson. Study of the two-dimensional-three-dimensional growth mode transition in metalorganic vapor phase epitaxy of GaInP/InP quantum-sized structures. *Appl. Phys. Lett.*, 65(24):3093–3095, 1994.

[83] S.P. DenBaars, C.M. Reaves, V. Bressler-Hill, S. Varma, W.H. Weinberg, and P.M. Petroff. Formation of coherently strained self-assembled InP quantum islands on InGaP/GaAs(001). *J. Crystal Growth*, 145(1–4):721–727, 1994.

[84] A. Kurtenbach, K. Eberl, and T. Shitara. Nanoscale InP islands embedded in InGaP. *Appl. Phys. Lett.*, 66(3):361–363, 1995.

[85] T. Okuno, H.W. Ren, M. Sugisaki, K. Nishi, S. Sugou, and Y. Masumoto. Time-resolved luminescence of InP quantum dots in a GaInP matrix: Carrier injection from the matrix. *Phys. Rev. B*, 57(3):1386–1389, 1998.

[86] O. Madelung, M. Schulz, and H. Weiss, editors. *Physics of group IV elements and III-V compounds, Landolt-Börnstein numerical data and relationships*, volume 17a of *New series III.* Springer-Verlag, Berlin, 1982.

[87] Y.K. Chen, M.C. Wu, J.M. Kuo, M.A. Chin, and A.M. Sergent. Self-aligned InGaAs/GaAs/InGaP quantum well lasers prepared by gas-source molecular beam epitaxy with two growth steps. *Appl. Phys. Lett.*, 59(23):2929–2931, 1991.

[88] Z.L. Liau, S.C. Palmateer, S.H. Groves, J.N. Walpole, and L.J. Missaggia. Low-threshold InGaAs strained-layer quantum-well lasers (=0.98 m) with GaInP cladding layers and mass-transported buried heterostructure. *Appl. Phys. Lett.*, 60(1):6–8, 1992.

[89] K. Tone, T. Nakayama, H. Iechi, K. Ohtsu, and H. Kukimoto. Selectively doped n-GaInP/GaAs heterostructures grown by MOCVD. *Jpn. J. Appl. Phys.*, 25:L429, 1986.

[90] A. Gomyo, K. Kobayashi, S. Kawata, I. Hino, T. Suzuki, and T. Yuasas. Studies of GaInP layers grown by metalorganic vapor phase epitaxy; effects of V/III ratio and growth temperature. *J. Crystal Growth*, 77(1–3):367–373, 1986.

[91] M.J. Hafich, J.H. Quigley, R.E. Owens, G.Y. Robinson, Du Li, and N. Otsuka. High quality quantum wells of InGaP/GaAs grown by molecular beam epitaxy. *Appl. Phys. Lett.*, 54(26):2686–2688, 1989.

[92] J.H. Quigley, M.J. Hafich, H.Y. Lee, R.E. Stave, and G.Y. Robinson. Growth of InGaP on GaAs using gas-source molecular-beam epitaxy. *J. Vac. Sci. Technol. B*, 7(2):358–360, 1989.

[93] B.T. McDermott, K.G. Reid, N.A. El-Masry, S.M. Bedair, W.M. Duncan, X. Yin, and F.H. Pollak. Atomic layer epitaxy of GaInP ordered alloy. *Appl. Phys. Lett.*, 56(12):1172–1174, 1990.

[94] Ph. Maurel, Ph. Bove, J.C. Garcia, and C. Grattepain. Metal-organicmolecular beam epitaxy of GaAs and GaInP. *Semicond. Sci. Technol.*, 6(4):254–260, 1991.

[95] W.T. Masselink, M. Zachau, T.W. Hickmott, and K. Hendrickson. Electronic and optical characterization of InGaP grown by gas-source molecular-beam epitaxy. *J. Vac. Sci. Technol. B*, 10(2):966–968, 1992.

[96] M. Usami, Y. Matsushima, and Y. Takahashi. Gas source molecular beam epitaxy growth of GaAs/InGaP superlattice as optical confinement layers in 0.98 m InGaAs/InGaP strained quantum well lasers. *J. Crystal Growth*, 150(Part 2):1344–1349, 1995.

[97] T. Suzuki, A. Gomyo, S. Iijima, K. Kobayashi, S. Kawata, I. Hino, and T. Yuasa. Band-GaP energy anomaly and sublattice ordering in GaInP and AlGaInP grown by metalorganic vapor phase epitaxy. *Jpn. J. Appl. Phys.*, 27(11):2098–2106, 1988.

[98] A. Gomyo, T. Suzuki, and S. Iijima. Observation of strong ordering in GaInP alloy semiconductors. *Phys. Rev. Lett.*, 60(25):2645–2648, 1988.

[99] T. Suzuki and A. Gomyo. Re-examination of the formation mechanism of CuPt-type natural superlattices in alloy semiconductors. *J. Crystal Growth*, 111(1–4):353–359, 1991.

[100] M. Kondow, H.Kabayashi, and S. Minagawa. Ordered structure in OMVPE-grown InGaP. *J. Crystal Growth*, 88(2):291–296, 1988.

[101] C. Nozaki, Y. Ohba, H. Sugawara, S. Yasuami, and T. Nakanisi. Growth temperature dependent atomic arrangements and their role on band-GaP of InGaAlP alloys grown by MOCVD. *J. Crystal Growth*, 93(1–4):406–411, 1988.

[102] M. Razeghi, P. Maurel, F. Omnes, S. Ben Armor, L. Dmowski, and J.C. Portal. First observation of the two-dimensional properties of the electron gas in GaInP/GaAs heterojunctions grown by low pressure metalorganic chemical vapor deposition. *Appl. Phys. Lett.*, 48(19):1267–1269, 1986.

[103] F. Omnes and M. Razeghi. Optical investigations of GaAs-GaInP quantum wells and superlattices grown by metalorganic chemical vapor deposition. *Appl. Phys. Lett.*, 59(9):1034–1036, 1991.

[104] Q. Liu, S. Derksen, A. Lindner, F. Scheffer, W. Prost, and F.-J. Tegude. Evidence of type-II band alignment at the ordered GaInP to GaAs heterointerface. *J. Appl. Phys.*, 77(3):1154–1158, 1995.

[105] S. Froyen, A. Zunger, and A. Mascarenhas. Polarization fields and band offsets in GaInP/GaAs and ordered/disordered GaInP superlattices. *Appl. Phys. Lett.*, 68(20):2852–2854, 1996.

[106] J. Dong, Z. Wang, X. Liu, D. Lu, and D. Wang. Photoluminescence of ordered GaInP grown by metalorganic vapor phase epitaxy. *Appl. Phys. Lett.*, 67(11):1573–1575, 1995.

[107] Y. Hsu, G.B. Stringfellow, C.E. Inglefield, M.C. DeLong, P.C. Taylor, J.H. Cho, and T.-Y. Seong. Quantum wells due to ordering in GaInP. *Appl. Phys. Lett.*, 73(26):3905–3907, 1998.

[108] M.C. DeLong, D.J. Mowbray, R.A. Hogg, M.S. Skolnick, M. Hopkinson, J.P.R. David, P.C. Taylor, S.R. Kurtz, and J.M. Olson. Photoluminescence, photoluminescence excitation and resonant raman spectroscopy of disordered and ordered GaInP. *J. Appl. Phys.*, 73(10):5163–5172, 1993.

[109] P. Ernst, C. Geng, F. Scholz, H. Schweizer, Y. Zhang, and A. Mascarenhas. Band-GaP reduction and valence-band splitting of ordered $GaInP_2$. *Appl. Phys. Lett.*, 67(16):2347–2349, 1995.

[110] P. Ernst, C. Geng, F. Scholz, and H. Schweizer. Ordering in $GaInP_2$ studied by optical spectroscopy. *Phys. Stat. Sol. (b)*, 193:213–229, 1996.

[111] M. Kondow, S. Minagawa, Y. Inoue, T. Nishino, and Y. Hamakawa. Anomalous temperature dependence of the ordered GaInP photoluminescence spectrum. *Appl. Phys. Lett.*, 54(18):1760–1762, 1995.

[112] F.A.J.M. Driessen, G.J. Bauhuis, S.M. Olsthoorn, and L.J. Giling. Effects of confined donor states on the optical and transport properties of ordered $GaInP_2$ alloys. *Phys. Rev. B*, 48(11):7889–7896, 1993.

[113] C. Geng, M. Moser, R. Winterhoff, E. Lux, J. Hommel, B. Höhing, H. Schweitzer, and F. Scholz. Ordering in strained GaInP quntum wells grown by metalorganic vapor phase epitaxy. *J. Crystal Growth*, 145(1–4):740–745, 1994.

[114] S.-H. Wei and A. Zunger. Optical properties of zinc-blende semiconductor alloys: Effects of epitaxial strain and atomic ordering. *Phys. Rev. B*, 49(20):14337–14351, 1994.

[115] A.K. Mäder and A. Zunger. Short- and long -range-order effects on the electronic properties of III-V semiconductor alloys. *Phys. Rev. B*, 51(16):10462–10476, 1995.

[116] J. Bettini, M.M.G. de Carvalho, M.A. Cotta, M.A.A. Pudenzi, N.C. Frateschi, A. Silva Filho, L.P. Cardoso, and R. Landers. Analysis of Be doping of InGaP lattice matched to GaAs. *J. Crystal Growth*, 208(1–4):65–72, 2000.

[117] F. E. G. Guimarães, B. Elsner, R. Westphalen, B. Spangenberg, H.J. Geelen, P. Balk, and K. Heime. LP-MOVPE growth and optical characterization of GaInP/GaAs heterointerfaces, quantum wells and quantum wires. *J. Crystal Growth*, 124(1–4):199–206, 1992.

[118] C.Y. Tsai, M. Moser, C. Geng, V. Härle, T. Foner, P. Michler, A. Hangleiter, and F. Scholz. Interface characterisitics of GaInP/GaAs double heterostructures grown by metalorganic vapor phase epitaxy. *J. Crystal Growth*, 145(1–4):786–791, 1994.

[119] R. Bhat, M.A. Koza, M.J.S.P. Brasil, R.E. Nahory, C.J. Palmstrom, and B.J. Wilkens. Interface control in GaAs/GaInP superlattices grown by OMCVD. *J. Crystal Growth*, 124(1–4):576–582, 1992.

[120] E. Vanelle, M. Mesrine, N. Grandjean, C. Deparis, and J. Massies. Interface effects on the photoluminescence of GaAs/GaInP quantum wells. *Jpn. J. Appl. Phys.*, 37, Part 1(1):15–22, 1998.

[121] F. Hatami, N.N. Ledentsov, J. Böhrer M. Grundmann, F. Heinrichsdorff, M. Beer, D. Bimberg, S. Ruvimov, P. Werner, U. Gösele, J. Heydenreich, U. Richter, V. Ivanov, B.Ya. Meltser, P.S. Kop'ev, and Zh.I. Alferov. Radiative recombination in type-II GaSb/GaAs quantum dots. *Appl.Phys. Lett.*, 67(5):656–658, 1995.

[122] A. Rosenauer, U. Fischer, D. Gerthsen, and A. Förster. Composition evaluation by lattice fringe analysis. *Ultramicroscopy*, 72(3–4):121–133, 1998.

[123] N. Carlsson, K. Georgsson, M. Montelius, L. Samuelson, W. Seifert, and R. Wallenberg. Improved size homogeneity of InP-on-GaInP Stranski-Krastanow islands by growth on a thin GaP interface layer. *J. Crystal Growth*, 156(1–2):23–29, 1995.

[124] L.R. Wallenberg, K. Georgsson, W. Seifert, N. Carlsson, J. Lindahl, and L. Samuelson. Transmission electron microscopy of InP Stranski-Krastanow islands burried in InGaP. *Phys. Stat. Sol. (a)*, 150:479–487, 1995.

[125] H.-W. Ren, M. Sugisaki, J.-S. Lee, S. Sugou, and Y. Masumoto. Highly uniform and small InP/GaInP self-assembled quantum dots grown by metal-organic vapor phas epitaxy. *Jpn. J. Appl. Phys.*, 38, Part1(1B):507–510, 1999.

[126] K. Georgsson, N. Carlsson, L. Samuelson, W. Seifert, and L.R. Wallenberg. Transmission electron microscopy investigation of the morphology of InP stranskikrastanow islands grown by metalorganic chemical vapor deposition. *Appl. Phys. Lett.*, 67(20):2981–2982, 1995.

[127] M.K. Zundel, P. Specht, K. Eberl, N.Y. Jin-Phillipp, and F. Phillipp. Structural and optical properties of vertically aligned InP quantum dots. *Appl. Phys. Lett.*, 71(20):2972–2974, 1997.

[128] N.Y. Jin-Phillipp and F. Phillipp. Strain distribution in self-assembled InP/GaInP quantum dots. *J. Appl. Phys.*, 88(2):710–715, 2000.

[129] W.-Y. Wu, J.N. Schulman, T.Y. Hsu, and U. Efron. Effect of size nonuniformity on the absorbtion spectrum of a semiconductor quantum dot system. *Appl. Phys. Lett.*, 51(10):710–712.

[130] M. Grundmann, J. Christen, N.N. Ledentsov, J. Böhrer, D. Bimberg, S.S. Ruvimov, P. Werner, U. Richter, U. Gösele, J. Heydenreich, V.M. Ustinov, A.Yu. Egorov, A.E. Zhukov, P.S. Kop'ev, and Zh.I. Alferov. Ultranarrow luminescence lines from single quantum dots. *Phys. Rev. Lett.*, 74(20):4043–4046, 1995.

[131] C.M. Reaves, V. Bressle-Hill, M. Krishnamurthy, S. Varma, P.M. Petroff, W.H. Weinberg, and S.P. DenBaars. InP islands on GaAs substrates: MOCVD growth of quantum-sized structures. In *Proc. of the sixth Inter. Conf. on InP and rel. mater.*, page 611, NY, 1994. IEEE.

[132] M. Califano and P. Harrison. Quantum box energies as a route to the ground state levels of self-assembled InAs pyramidal dots. *J. Appl. Phys.*, 88(10):5870–5874, 2000.

[133] M.A. Cusack, P.R. Briddon, and M. Jaros. Absorption spectra and optical transitions in InAs/GaAs self-assembled quantum dots. *Phys. Rev. B*, 56(7):4047–4050, 1997.

[134] T. Ezaki, N. Mori, and C. Hamaguchi. Electronic structures in circular, elliptic and triangular quantum dots. *Phys. Rev. B*, 56(11):6428–6431, 1997.

[135] S. Jeppesen, M.S. Miller, D. Hessman, B. Kowalski, I. Maximov, and L. Samuelson. Assembling strained InAs islands on patterned GaAs substrates with chemical beam epitaxy. *Appl. Phys. Lett.*, 68(16):2228–2230, 1996.

[136] Y.P. Varshni. Temperature dependence of the energy GaP in semiconductors. *Physica*, 34:149, 1967.

[137] M. Levinshtein, S. Rumyantsev, and M. Shur, editors. *Handbook series on semicond. parameters.* World Scientific Publishing Co., Singapore, 1996.

[138] D. Bimberg, M. Sondergeld, and E. Grobe. Thermal dissociation of exciton bounds to neutral acceptor in high-purity GaAs. *Phys. Rev. B*, 4(10):3451–3455, 1971.

[139] P.J. Dean. Absorption and luminescence of excitons at neutral donors in gallium phosphide. *Phys. Rev.*, 157:655, 1967.

[140] N.N. Ledentsov, M. Grundmann, J. Böhrer, F. Heinrichsdorff, M. Beer, D. Bimberg, S. Ruvimov, P. Werner, U. Gösele, J. Heydenreich, U. Richter, V. Ivanov, B.Ya. Meltser, P.S. Kop'ev, and Zh.I. Alferov. Radiative state in type-II GaSb/GaAs quantum wells. *Phys. Rev. B*, 52(19):14058–14066, 1995.

[141] N.N. Ledentsov, P.D. Wang, C.M. Sotomayor Torres, A.Yu. Egorov, M.V. Maximov, V.M. Ustinov, A.E. Zhukov, and P.S. Kop'ev. Optical spectroscopic studies of InAs layer transformation on GaAs surfaces. *Phys. Rev. B*, 50(16):12171–12174, 1994.

[142] V.A. Kulbachinskii, V.G. Kytin, R.A. Lunin, A.V. Golikov, I.G. Malkina, B.N. Zvonkov, and Yu.N. Safyanov. Peculiarities of optical and low-temperature transport properties of multi-layer InAs-GaAs structures with quantum dots. *Physica B*, 266:185, 1999.

[143] A. Weber, O. Gauthier-Lafaye, F.H. Julien, J. Brault, M. Gendry, Y. Desierres, and T. Benyattou. Strong normal-incidence ifrared absorption in self-organized InAs/ InAlAs quantum dots grown on InP(001). *Appl. Phys. Lett.*, 74(3):413–415, 1999.

[144] W. Yang, H. Lee, T.J. Johnson, P.C. Sercel, and A.G. Norman. Electronic structure of self-organized InAs/GaAs quantum dots bounded by {136} facets. *Phys. Rev. B*, 61(4):2784–2793, 2000.

[145] W.-L. Wang, J. Kim, and A. Zunger. Electronic structures of [110]-faceted self-assembled pyramidal InAs/GaAs quantum dots. *Phys. Rev. B*, 59(8):5678–5687, 1999.

[146] U. Bockelmann and G. Bastard. Interband absorption in quantum wires. I. zero-magnetic-field case. *Phys. Rev. B*, 45(4):1688–1699, 1992.

[147] Y. Takagaki and K.H. Ploog. Magnetic field dependence of optical anisotropy in InGaAs quantum dots. *Phys. Stat. Sol. (b)*, 225:237, 2001.

[148] M. Sugisaki, H.-W. Ren, S.V. Nair, K. Nishi, S. Sugou, T. Okuno, and Y. Masumoto. Optical anisotropy in self-assembled InP quantum dots. *Phys. Rev. B*, 59(8):R5300–R5303, 1999.

[149] H.J. Zhu, M. Ramsteiner, K.H. Ploog, R. Zhang, R. Tsui, K. Shiralagi, and H. Goronkin. Anisotropy of electronic wave function in self-aligned InAs dots. *Phys. Rev. B*, 62(24):R16314–R16317, 2000.

[150] U. Bockelmann and G. Bastard. Interband absorption in quantum wires. II. nonzero-magnetic-field case. *Phys. Rev. B*, 45(4):1700–1704, 1992.

[151] C. Pryor, M.-E. Pistol, and L. Samuelson. Electronic structure of strained InP/GaInP quantum dots. *Phys. Rev. B*, 56(16):10404–10411, 1997.

[152] L. Janssens, B. Partoens, and F.M. Peeters. Magnetoexcitons in planar type-II quantum dots in a perpendicular magnetic field. *Phys. Rev. B*, 64:155324–155332, 2001.

[153] K. Eberl, A. Kurtenbach, K. Häusler, F. Noll, and W.W. Rühle. Strained layer epitaxy-materials processing and device application. In K.-Y. Cheng E. Fitzgerald, J. Hoyt and J. Bean, editors, *Mat. Res. Soc. Symp. Proc.*, volume 379, page 145, 1995.

[154] A. Christ, H. Giessen, W.W. Rühle, K. Korona, J. Kuhl, M. Zundel, Y. Manz, and K. Eberl. Carrier dynamics in stacked InP/InGaP QDs. *Phys. Stat. Sol. (b)*, 221:59, 2000.

[155] F. Hatami, M. Grundmann, N.N. Ledentsov, F. Heinrichsdorff, R. Heitz, J. Böhrer, D. Bimberg, S. Ruvimov, P. Werner, S.V. Ivanov, B.Ya. Meltser, V. Ustinov, P.S. Kop'ev, and Zh.I. Alferov. Carrier dynamics in type-II GaSb/GaAs quantum dots. *Phys. Rev. B*, 57(8):4635–4641, 1998.

[156] C. Ulrich, S. Ves, A.R. Gõni, A. Kurtenbach, K. Syassen, and K. Eberl. Electronic subband structure of InP/InGaP quantum islands from high-pressure photoluminescence and photoreflectance. *Phys. Rev. B*, 52(16):12212–12217, 1995.

[157] B. Junno, T. Junno, M.S. Miller, and L. Samuelson. A reflection high-energy electron diffraction and atomic force microscopy study of the chemical beam epitaxial growth of InAs and InP islands on (001) GaP. *Appl. Phys. Lett.*, 72(8):954–956, 1998.

[158] F. Hatami, L. Schrottke, and W.T. Masselink. Radiative recombination from InP quantum dots on (100) GaP. *Appl. Phys. Lett.*, 78(15):2163–2165, 2001.

[159] J.N. Baillargeon, K.Y. Cheng, and K.C. Hsieh. Surface structure of (100) GaP grown by gas source molecular beam epitaxy. *Appl. Phys. Lett.*, 56(22):2201–2203, 1990.

[160] J.N. Baillargeon, K.C. Hsieh, and G.E. Stillman. The gas source molecular beam epitaxial growth of AlGaP on (100) GaP. *J. Appl. Phys.*, 68(5):2133–2139, 1990.

[161] J.N. Baillargeon, K.Y. Cheng, K.C. Hsieh, and C.L. Wei. Growth and silicon doping of AlGaP on GaP by gas source molecular beam epitaxy. *J. Crystal Growth*, 105(1–4):106–110, 1990.

[162] C.E.C. Wood, K. Singer, T. Ohashi, L.R. Dawson, and A.J. Noreika. A pragmatic approach to adatom-induced surface reconstruction of III-V compounds. *J. Appl. Phys.*, 54(5):2732–2737, 1983.

[163] M. Yoshikawa, A. Nakamura, T. Nomura, and K. Ishikawa. Surface reconstruction of GaP (001) for various surface stoichiometries. *Jpn. J. Appl. Phys.*, 35, Part1(2B):1205–12108, 1996.

[164] A.M. Frisch, W.G. Schmidt, J. Bernholc, M. Pristovsek, N. Esser, and W. Richter. (2×4) GaP(001) surface: Atomic structure and optical anisotropy. *Phys. Rev. B*, 60(4):2488–2494, 1999.

[165] W.G. Schmidt, J. Bernholc, and F. Bechstedt. (001) surfaces of GaP and InP: structural motifs, electronic states and optical signatures. *Appl. Surf. Science*, 166:179, 2000.

[166] J. Ramdani, Y. He, M. Leonard, N. El-Masry, and S.M. Bedair. Low-temperature growth of high resistivity GaP by gas-source molecular beam epitaxy. *Appl. Phys. Lett.*, 61(14):1646–1648, 1992.

[167] W.-C. Liu, D.-F. Guo, C.-Y. Sun, and W.-S. Lour. Morphological defects on Be-doped AlGaAs layers grown by MBE. *J. Crystal Growth*, 114(4):700–706, 1991.

[168] N. Chand and S.N.G. Chu. *J. Crystal Growth*, 104(2):485–497, 1990.

[169] M.A. Cotta, R.A. Hamm, S. Chu, R. Harriott, and H. Temkin. On the origin of oval defects in metalorganic molecular beam epitaxy of InP. *Appl. Phys. Lett.*, 66(18):2358–2360, 1995.

[170] H. Schmidt, B. Rheinländer, V. Gottschalch, and G. Wagner. InP monolayers inserted in a GaP matrix studied by spectroscopic ellipsometry. *Thin Solid Films*, (312):356, 1998.

[171] J.A. Prieto, G. Armelles, M.-E. Pistol, P. Castrillo, J.P. Silveira, and F. Briones. Optical studies of GaAs quantum wells strained to GaP. *Appl. Phys. Lett.*, 70(25):3449–3451.

[172] M.-E. Pistol, M.R. Leys, and L. Samuelson. Properties of thin strained Ga(As,P) layers. *Phys. Rev. B*, 37(9):4664–4670, 1988.

[173] K. Arimoto, T. Sugita, N. Usami, and Y. Shiraki. Effect of the insertion of an ultrathin AlP layer on the optical properties of GaAsP/GaP quantum wells. *Phys. Rev. B*, 60(19):13735–13739, 1999.

[174] S. Nagao, T. Fujimori, H. Gotoh, H. Fukushima, T. Takano, H. Ito, S. Koshihara, and F. Minami. Type-II photoluminescence from GaP/AlP/GaP quantum wells. *J. Appl. Phys.*, 81(3):1417–1421, 1997.

[175] P. Merle, D. Auvergne, and H. Mathieu. Conduction band structure of GaInP. *Phys. Rev. B*, 15(4):2032–2047, 1977.

[176] H. Mathieu, P. Merle, and E.L. Ameziane. No-phonon and phonon assisted transitions in indirect $GaAs_{1-x}P_x$ modulation spectra. *Phys. Rev. B*, 15(4):2048–2052, 1977.

[177] J. Moore, G. Duggan, P. Dawson, and C.T. Foxon. Short-period GaAs-AlAs superlattices: Optical properties and electronic structure. *Phys. Rev. B*, 38(8):5535–5542, 1988.

[178] J. Feldmann, R. Sattmann, E. Göbel, J. Kuhl, J. Hebling, K. Ploog, R. Muralidharan, P. Dawson, and C.T. Foxon. Subpicosecond real-space charge transfer in type-II GaAs/AlAs superlattices. *Phys. Rev. Lett.*, 62(17):1892–1895, 1989.

[179] Yu.I. Mazur, J.W. Tomm, V. Petrov, G.G. Tarasov, H. Kissel, C. Walther, Z.Ya. Zhuchenko, and W.T. Masselink. Staircase-like spectral dependence of ground-state luminescence time constants in high-density InAs/GaAs quantum dots. *Appl. Phys. Lett.*, 78(21):3214–3216, 2001.

[180] T.R. Ramachandran, R. Heitz, P. Chen, and A. Madhukar. Mass transfer in StranskiKrastanow growth of InAs on GaAs. *Appl. Phys. Lett.*, 70(5):640–642, 1997.

[181] M. Jaros and S. Brand. Localized defects in III-V semiconductors. *Phys. Rev. B*, 14(10):4494–4505, 1976.

[182] H. Kroemer and G. Griffiths. *IEEE Electron Device Lett.*, 4:20, 1983.

[183] G.H. Li, A.R. Gõni, C. Abraham, K. Syassen, P.V. Santos, A. Cantarero, O. Brandt, and K. Ploog. Photoluminescence from strained InAs monolayers in GaAs under pressure. *Phys. Rev. B*, 50(3):1575–1581, 1994.

[184] G.H. Li, A.R. Gõni, K. Syassen, O. Brandt, and K. Ploog. State mixing in InAs/GaAs quantum dots at the pressure-induced Gamma-X crossing. *Phys. Rev. B*, 50(24):18420–18425, 1994.

[185] Pressure-dependent photoluminescence measurements by C. Kristuk at TU Berlin.

[186] A.R. Gõni, K. Syassen, K. Strössner, and M. Cardona. Effect of pressure on the optical absorption in GaP and $\mathrm{Ga}_x\mathrm{In}_{1-x}\mathrm{P}$ (x=0.36 and 0.5). *Phys. Rev. B*, 39(5):3178–3184, 1989.

[187] P.Y. Yu. *Fundamentals of Semiconductors: Physics and Materials Properties.* Springer-Verlag, Berlin, 1999.

[188] Y. Takagaki. private communication.

[189] U. Bockelmann, W. Heller, and G. Abstreiter. Microphotoluminescence studies of single quantum dots. II. magnetic-field experiments. *Phys. Rev. B*, 55(7):4469–4472, 1997.

[190] A.J. Williamson, A. Zunger, and A. Canning. prediction of a strain-induced conduction-band minimum in embedded quantum dots. *Phys. Rev. B*, 57(8):R4253–R4256, 1998.

[191] P. Dawson, K.J. Moore, C.T. Foxon, G.W. ‘t Hooft, and R.P.M. van Hal. Photoluminescence decay time studies of type II-GaAs/AlAs quantum-well structures. *J. Appl. Phys.*, 65(9):3606–3609, 1989.

[192] R. Heitz, M. Veit, N.N. Ledentsov, A. Hoffmann, D. Bimberg, V.M. Ustinov, P.S. Kop’ev, and Zh.I. Alferov. Energy relaxation by multiphonon processes in InAs/GaAs quantum dots. *Phys. Rev. B*, 56(16):10435–10445, 1997.

[193] R. Heitz, A. Kalburge, Q. Xie, M. Grundmann, P. Chen, A. Hoffmann, A. Madhukar, and D. Bimberg. Excited states and energy relaxation in stacked InAs/GaAs quantum dots. *Phys. Rev. B*, 57(15):9050–9060, 1998.

[194] G.G. Tarasov, Yu.I. Mazur, Z.Ya. Zhuchenko, A. Maadorf, D. Nickel, J.W. Tomm, H. Kissel, C. Walther, and W.T. Masselink. Carrier transfer in self-assembled coupled InAs/GaAs quantum dots. *J. Appl. Phys.*, 88(12):7162–7170, 2000.

[195] J. Feldmann, G. Peter, E.O. Göbel, P. Dawson, K. Moore, C.T. Foxon, and R.J. Elliott. Linewidth dependence of radiative exciton lifetimes in quantum wells. *Phys. Rev. Lett.*, 59(20):2337–2340, 1987.

[196] J. Feldmann, G. Peter, E.O. Göbel, P. Dawson, K. Moore, C.T. Foxon, and R.J. Elliott. Linewidth dependence of radiative exciton lifetimes in quantum wells, errata. *Phys. Rev. Lett.*, 60(3):243, 1988.

[197] A.-L. Barabsi. Self-assembled island formation in heteroepitaxial growth. *Appl. Phys. Lett.*, 70(19):2565–2567, 1997.

[198] H.T. Dobbs, D.D. Vvedensky, A. Zangwill, J. Johansson, N. Carlsson, and W. Seifert. Mean-field theory of quantum dot formation. *Phys. Rev. Lett.*, 79(5):897–900, 1997.

[199] N. Moll, M. Scheffler, and E. Pehlke. Influence of surface stress on the equilibrium shape of strained quantum dots. *Phys. Rev. B*, 58(8):4566–4571, 1998.

[200] M. Meixner, E. Schöll, V.A. Shchukin, and D. Bimberg. Self-assembled quantum dots: Crossover from kinetically controlled to thermodynamically limited growth. *Phys. Rev. Lett.*, 87(23):236101–236104, 2001.

[201] F. Patella, M. Fanfoni, F. Arciprete, S. Nufris, E. Placidi, and A. Balzarotti. Kinetic aspects of the morphology of self-assembled InAs quantum dots on GaAs(001). *Appl. Phys. Lett.*, 78(3):320–322, 2001.

[202] S. Ruvimov, P. Werner, K. Scheerschmidt, J. Heydenreich, U. Richter, N.N. Ledentsov, M. Grundmann, D. Bimberg, V.M. Ustinov, A.Yu. Egorov, P.S. Kop'ev, and Zh.I. Alferov. Structural characterization of (In,Ga)As quantum dots in a GaAs matrix. *Phys. Rev. B*, 51(20):14766–14769, 1995.

[203] I. Kegel, T.H. Metzger, J. Peisl, P. Schlittenhelm, and G. Abstreiter. Lateral ordering of coherent Ge islands on Si(001) studied by triple-crystal grazing incidence diffraction. *Appl. Phys. Lett.*, 74(20):2978–2980, 1999.

[204] M. Schmidbauer, F. Hatami, P. Schäfer, M. Hanke, Th. Wiebach, H. Niehus, W.T. Masselink, and R. Köhler. Shape, strain and spatial correlation of InP/InGaP QDs multilayers. In *Mat. Res. Soc. Symp. Proc.*, volume 642, page J6.8, 2001.

[205] H.J. Kim, Y.J. Park, E.K. Kim, and T.W. Kim. Size control of InAs quantum dots on 2°-off GaAs (100) substrate by the thickness of GaAs buffer layer. *J. Crystal Growth*, 223(4):450–455, 2001.

[206] M. Schmidbauer, M. Hanke, F. Hatami, P. Schäfer, H. Raidt, D. Grigoriev, T. Panzer, W.T. Masselink, and R. Köhler. Shape induced anisotropic elasic relaxation in InP/InGaP quantum dots. *Physica E*, 13(2–4):1139–1142, 2002.

[207] M. Schmidbauer, F. Hatami, M. Hanke, P. Schäfer, K. Braune, W.T. Masselink, R. Köhler, and M. Ramsteiner. Shape mediated anisotropic strain in self-asselmbed InP/InGaP quantum dots. *Phys. Rev. B*, 65:125320–125326, 2002.

[208] M. Grundmann, O. Stier, and D. Bimberg. InAs/GaAs pyramidal quantum dots: Strain distribution, optical phonons and electronic structure. *Phys. Rev. B*, 52(16):11969–11981, 1995.

[209] Th. Wiebach, M. Schmidbauer, M. Hanke, H. Radit, R. Köhler, and H. Wawra. Strain and composition in SiGe nanoscale islands studied by x-ray scattering. *Phys. Rev. B*, 61(8):5571–5578, 2000.

[210] M. Schmidbauer, M. Hanke, and R. Köhler. X-ray diffuse scattering on self-organized mesoscopic structures. *Crys. Res. Technol*, 37:3, 2002.

[211] C. Pryor, J. Kim, L.W. Wang, A.J. Williamson, and A. Zunger. Comparison of two methods for describing the strain profiles in quantum dots. *J. Appl. Phys.*, 83:2548, 1998.

[212] J. Tersoff, C. Teichert, and M.G. Lagally. Self-organization in growth of quantum dot superlattices. *Phys. Rev. Lett.*, 76(10):1675–1678, 1996.

[213] R. Leon, Y. Kim, C. Jagadish, M. Gal, J. Zou, and D.J.H. Cockayne. Effects of interdiffusion on the luminescence of InGaAs/GaAs quantum dots. *Appl. Phys. Lett.*, 69(13):1888–1890, 1996.

[214] S. Malik, C. Roberts, R. Murray, and M. Pate. Tuning self-assembled InAs quantum dots by rapid thermal annealing. *Appl. Phys. Lett.*, 71(14):1987–1989, 1997.

[215] R. Leon, S. Fafard, P.G. Piva, S. Ruvimov, and Z. Liliental-Weber. Tunable intersublevel transitions in self-forming semiconductor quantum dots. *Phys. Rev. B*, 58(8):R4262–R4265, 1998.

[216] S.J. Xu, X.C. Wang, S.J. Chua, C.H. Wang, W.J. Fan, J. Jiang, and X.G. Xie. Effects of rapid thermal annealing on structure and luminescence of self-assembled InAs/GaAs quantum dots. *Appl. Phys. Lett.*, 72(25):3335–3337, 1998.

[217] T.M. Hsu, Y.S. Lan, W.-H. Chang, N.T. Yeh, and J.-I. Chyi. Tuning the energy levels of self-assembled InAs quantum dots by rapid thermal annealing. *Appl. Phys. Lett.*, 76(6):691–693, 2000.

[218] G. Mussler. Der Einfluß einer Thermischen Behandlung auf InP/GaP und InP/$In_{0,48}Ga_{0,52}P$ Quantenpunkte. Master's thesis, Institut für Physik, Humboldt-Universität zu Berlin, 2001.

[219] I. Lahiri, D.D. Nolte, J.C. Chang, J.M. Woodall, and M.R. Melloch. The role of excess arsenic in interface mixing in low-temperature-grown AlAs/GaAs superlattices. *Appl. Phys. Lett.*, 67(9):1244–1246, 1995.

[220] H.M. You, T.Y. Tan, U.M. Gösele, S.T. Lee, G.E. Höfler, K.C. Hsieh, and N. Holonyak,Jr. Al-Ga interdiffusion, carbon acceptor diffusion and hole reduction in carbon-doped $Al_{0.4}Ga_{0.6}As$/GaAs superlattices: The As_4 pressure effect. *J. Appl. Phys.*, 74(4):2450–2460, 1993.

[221] U. Voland, R. Cerny, P. Deus, D. Bergner, and G. Fenninger. X-ray diffraction studies of interdiffusion in InP-GaP powder blends. *Cryst. Res. Technol.*, 24(11):1177–1185, 1989.

[222] W.P. Gillin, S.S. Rao, I.V. Bradley, K.P. Homewood, A.D. Smith, and A.T.R. Briggs. Vacancy controlled interdiffusion of the group V sublattice in strained InGaAs/InGaAsP quantum wells. *Appl. Phys. Lett.*, 63(6):797–799, 1993.

[223] W.P. Gillin, S.D. Perrin, and K.P. Homewood. Comparative study of silicon nitride encapsulated and phosphine overpressure annealing on the interdiffusion of $In_xGa_{1-x}As$–$In_xGa_{1-x}As_yP_{1-y}$ heterostructures. *J. Appl. Phys.*, 77(4):1463–1465, 1995.

[224] W.P. Gillin, D.J. Dunstan, K.P. Homewood, L.K. Howard, and B.J. Sealy. Interdiffusion in InGaAs/GaAs quantum well structures as a function of depth. *J. Appl. Phys.*, 73(8):3782–3786, 1993.

[225] I.V. Bradley, W.P. Gillin, K.P. Homewood, and R.P. Webb. The effects of ion implantation on the interdiffusion coefficients in $In_xG_{1-x}As$/GaAs quantum well structures. *J. Appl. Phys.*, 73(4):1686–1692, 1993.

[226] K.Y. Hsieh, Y.C. Lo, J.H. Lee, and R.M. Kolbas. In *Inst. Phys. Conf. Ser.*, volume 96, page 393, 1989.

[227] B.L. Olmsted and S.N. Houde-Walter. Disordering and compensation in Si-doped AlGaAs/GaAs superlattices using Ga- and As-rich annealing ambients. *Appl. Phys. Lett.*, 63(8):1131–1133, 1993.

[228] O.M. Khreis, W.P. Gillin, and K.P. Homewood. Interdiffusion: A probe of vacancy diffusion in III-V materials. *Phys. Rev. B*, 55(23):15813–15818, 1997.

[229] S.F. Wee, M.K. Chai, K.P. Homewood, and W.P. Gillin. The activation energy for GaAs/AlGaAs interdiffusion. *J. Appl. Phys.*, 82(10):4842–4846, 1997.

[230] H. Saito, K. Nishi, I. Ogura, S. Sugou, and Y. Sugimotor. Room-temperature lasing operation of a quantum-dot vertical-cavity surface-emitting laser. *Appl. Phys. Lett.*, 69(21):3140–3142, 1998.

[231] T. Riedl, E. Fehrenbacher, A. Hangleiter, M.K. Zundel, and K. Eberl. Injection lasers with vertically aligned InP/GaInP quantum dots: Dependence of the threshold current on temperature and dot size. *Appl. Phys. Lett.*, 73(25):3730–3732, 1998.

[232] J.H. Ryou, R.D. Dupuis, G. Walter, D.A. Kellogg, N. Holonyak,Jr., D.T. Mathes, R. Hull, C.V. Reddy, and V. Narayanamurti. Photopumped red-emitting InP/$In_{0.5}Al_{0.3}Ga_{0.2}P$ self-assembled quantum dot heterostructure lasers grown by metalorganic chemical vapor deposition. *Appl. Phys. Lett.*, 78(26):4091–4093, 2001.

[233] T.P. Chin, J.C.P. Chang, K.L. Kavanagh, C.W. Tu, P.D. Kirchner, and J.M. Woodall. Gas-source molecular beam epitaxial growth, characterization and light-emitting diode application of $In_xGa_{1-x}P$ on GaP(100). *Appl. Phys. Lett.*, 62(19):2369–2371, 1993.

Acknowledgemens

I am grateful to Prof. Dr. William Ted Masselink who gave me the opportunity to learn, research, and teach in his group, and who always stimulated and supported the progress of my work.

Prof. Dr. Anupam Madhukar (University of Southern California) and Prof. Dr. Klaus Ploog (Paul-Drude-Institut) are sincere acknowledged for refereing this thesis.

I thank my colleagues Dr. Wolfgang Hoerstel, Britta Herrmann, and Anne-Kathrin Bluhm for their technical support. Dr. Uwe Müller assisted me in all computer concerns. Dr. Carsten Walther has introduced me to the GSMBE.

Without the structural characterization of QDs, this work would not have been possible. I am very thankful Karin Braune (HU Berlin) for AFM,
Dr. Siegfried Rogaschewski (HU Berlin) for SEM,
Dr. Martin Schmidbauer (HU Berlin) for X-ray, and
Dr. Holm Kirmse (HU Berlin) for TEM measurements.

I am particularly grateful to Dr. Heiko Kissel (Ferdinand-Braun-Institut),
Dr. Lutz Schrottke (Paul-Drude-Institut),
Dr. Jens Tomm (Max-Born-Institut),
Dr. Hsin-Yi Hao (Paul-Drude-Institut),
Dr. Manfred Ramsteiner (Paul-Drude-Institut), and
Christian Kristuk (TU Berlin) for supporting and performance of optical measurements.

Dr. Yuki Takagaki (Paul-Drude-Institut) calculated the PL anisotropy. He is acknowledged for the fruitful discussions.

I thank graduated physicist Daniel Palloks for proof reading this thesis. His linguistic advice together with his very good comprehension pertaining to physics made this thesis readable.

And Michael, Keyhan, Samin, and Sierra for being there.

Selbständigkeitserklärung

Hiermit erkläre ich, die vorliegende Arbeit selbstndig ohne fremde Hilfe verfasst zu haben und nur die angegebene Literatur und Hilfsmittel verwendet zu haben.

Ich habe mich anderwärts nicht um einen Doktorgrad beworben und besitze einen entsprechenden Doktorgrad nicht.

Ich erkläre die Kenntnisnahme der dem Verfahren zugrunde liegenden Promotionsordnung der Mathematisch-Naturwissenschaftlichen Fakultät I der Humboldt-Universität zu Berlin.

Berlin, den 07. Mai 2002

Fariba Hatami